Quantitative Single Cell Analysis of Cancerous Cells During Therapy

By

Deon Bryant Doxie

Dissertation

Submitted to the Faculty of the

Graduate School of Vanderbilt University

in fulfillment of the requirements

for the degree of

DOCTOR OF PHILOSOPHY

in

Cancer Biology

June 30, 2018

Nashville, Tennessee

Approved :

Vito Quaranta M.D.

Ann Richmond Ph.D.

Mark Kelley M.D.

Jonathan Irish Ph.D.

ACKNOWLEDGMENTS

This work would not have been possible without the financial support from the Vanderbilt-Ingram Cancer Center (VICC, P30 CA68485) and from the NIH/NCI (T32 CA009592 and R25 GM062459). I am grateful to my advisor, Dr. Jonathan, who has provided guidance and mentorship throughout my graduate career. I am also grateful for the mentorship and guidance of my dissertation committee: Dr. Vito Quaranta, Dr. Ann Richmond, and Dr. Mark Kelley. Their guidance was instrumental in shaping my dissertation research.

In addition to my dissertation committee, I am also grateful to my collaborators Dr. Pierre Massion, Dr. Douglas Johnson, and Dr. Mark Kelley for valuable clinical insight and the opportunity to work with valuable human patient samples. I am also grateful to Dr. Rebecca Ihrie and the current and past members of both the Irish and Ihrie labs. Their support as colleagues and vital feedback throughout my research played an instrumental role in the success of my work presented here.

I am deeply grateful to my family and friends for their support. I thank my mother and sister, Gail and Jasmine Doxie, for their constant emotional support and encouraging feedback. I thank my father, Deon Doxie for his career advice and supporting my decisions. I thank my friends for being a source of support during my graduate training. My success would not have been possible without them.

PREFACE

In this dissertation, I discuss the impact of high dimensional cytometry in cancer research and utilize this approach to dissect cellular heterogeneity from several solid tumors. Ideally, a single cell systems biology approach may reveal novel cell populations containing a cellular mechanism of therapy evasion and disease relapse. This work includes unpublished, submitted, and published peer-reviewed data. The submitted and published data discussed within the body of this dissertation is in the same form as prepared for publication (Chapters 2-5). Many colleagues and collaborators played a major role in the development and success of this work. My work with clinical investigators Dr. Mark Kelley, Dr. Douglas Johnson, and Dr. Pierre Massion merits special attention here. The results of those respective collaborations are discussed in Chapters 3, 5 and the Appendix.

Chapter 1 introduces the significance of cellular heterogeneity in cancer and an overview of how melanoma heterogeneity contributes to disease outcome. This chapter also briefly introduces single cell analysis approaches, including cytometry analysis, discussed in detail in Chapter 2 and utilized throughout Chapters 3, 4, and 5. High dimensional analysis computational tools, such as viSNE and FlowSOM, are also introduced as a means to dissect heterogeneity with minimal human bias in Chapter 5.

Chapter 2 entitled, “High dimensional single cell cancer biology”, is a published review that discusses the single cell biology view of cancer using flow cytometry techniques. This chapter was written when mass cytometry and phospho-flow cytometry

had not previously been applied to study cells from solid tumors. However, the Future Directions section envisions application to study solid tumors as shown in Chapter 5. The review article was written to summarize the benefits and caveats of this approach, to update the field on new features that could be measured, and to introduce mass cytometry, which was also new at the time, having been introduced in 2011. The single cell analysis approaches discussed in this chapter cover methods to characterize cell identity, post-translationally modified signaling proteins, cell cycle status, proliferation, apoptosis, and biomarkers of clinical relevance creating the “single-cell systems biology” view of cancer. This review also discusses several peer-reviewed examples that reveal cancer subsets that affect patient prognosis and therapy response. With the range of therapeutic options for cancer rapidly growing, this review demonstrates that single cell techniques could become a critical asset for the next generation of cancer treatments.

Chapter 3 entitled “Melanoma signaling and novel Implications for immunotherapy prognosis”, describes the development of phosphow-flow analysis to dissect melanoma cell signaling and identification of abnormal signaling features associated with an immunotherapy poor prognosis phenotype. Collaboration with Dr. Doug Johnson and Dr. Justin Balko led to the discovery that patients with a melanoma cell immune interaction phenotype predicted a more favorable outcome in response to anti-PD-1 immunotherapy. My role in this work was to identify a potential molecular mechanism of therapy evasion for melanoma cells. This research revealed cells without the immune interaction phenotype displayed unexpected oncogenic signaling responses. This method was useful to develop for this thesis, as I subsequently applied solid tumor phospho-flow to measure signaling in

the cells from primary human melanoma tumors (Chapter 5). In addition, this work provided support for including MHC II and MHC I in the studies in Chapter 5.

Chapter 4 entitled “Single cell analysis of human tissues and solid tumors with mass cytometry,” describes the systematic development of dissociation methods to release viable adherent cells into suspension for mass cytometry analysis. This work revealed that solid tissues release the most viable cells with enzymatic digestion using collagenase and DNase. Furthermore, IHC analysis revealed a comparable abundance of stromal cells as mass cytometry analysis. Results from this work enabled the development of a workflow utilized in a clinical study of human melanoma in Chapter 5.

Chapter 5, entitled “BRAF and MEK inhibitor therapy eliminates nestin expressing melanoma cells in human tumors,” utilizes approaches in Chapters 1-4 to characterize dabrafenib and trametinib responses in $BRAF^{V600mut}$ melanoma. Tumors were biopsied before and immediately after four weeks of therapy to identify and characterize cell populations that escaped therapy. Analysis with mass cytometry and computational tools revealed consistent changes in cancer heterogeneity and a significant increase in infiltrating immune T cells. Melanoma cells that escaped therapy showed significant loss of nestin expression and typically lacked immune interaction protein MHC I. Furthermore, IHC analysis revealed a comparable loss of nestin as mass cytometry analysis. Taken together the discovery of a cellular phenotype that evaded targeted therapy led to new mechanistic hypotheses of targeted therapy resistance.

Chapter 6 summarizes the findings from Chapters 2-5 and elaborates on future directions of this work. In particular, I will discuss how this approach can be applied to

patient samples and xenograft models receiving combination targeted therapy and checkpoint immunotherapy. Furthermore, I will hypothesize what cellular phenotypes may escape these therapies and discuss how cellular reprogramming aides in evasion from therapy.

Appendix A applies techniques developed within this dissertation in a collaborative project to dissect human adenocarcinoma tumor heterogeneity. This research demonstrates how the utility of approaches discussed in this dissertation are also applicable to other solid tumor types with more challenging adhesive characteristics. Work is in progress to define phenotypes within the epithelial and leukocyte populations that could predict tumor behavior and immune response within the microenvironment.

Table of Contents

LIST OF FIGURES

Figure **Page**

LIST OF TABLES

Table **Page**

CHAPTER I

INTRODUCTION

The biological and clinical significance of cellular heterogeneity in cancer

Innovative immune and targeted therapies have the potential to dramatically increase patient survival, however, complete long-lasting responses are rare in most late-stage cancers (Garraway and Janne, 2012). To identify cellular mechanisms of therapy resistance, recent advances in technology have prioritized the study of cellular heterogeneity. To date, high rates of subclonal genetic heterogeneity are associated with more aggressive disease in several cancers including head and neck squamous carcinoma, adenocarcinoma, and chronic myeloid leukemia (Landau et al., 2013; Mroz et al., 2013; Yoon et al., 2012). In some cases, genetic aberrations don't necessarily change protein expression or cell behavior (Zhang et al., 2014a).

Historically therapeutic resistance was thought to be associated exclusively with the selection of a rare subset of cells that acquire a mechanism of resistance. Only recently has the field identified that some therapies may give rise to a more diverse pool of subclonal populations. Most notably, genetic variation has been shown to increase in CML after chemotherapy, and several BRAF inhibitor resistance mechanisms have been found to co-exist in the same patient with metastatic melanoma after therapy (Landau et al., 2013; Rizos et al., 2014; Shi et al., 2014). However, in some cases, there is no clear genetic cause for resistance (Shaffer et al., 2017). For example in melanoma and lung cancer,

therapies have been shown to temporarily reprogram tumor behavior and cellular phenotypes in response to therapy (Oser et al., 2015; Song et al., 2017). A key question that has risen in the field is “does therapy change cell identity”? I will not be able to conclusively answer this, but my findings taken in context with the field suggest cellular plasticity also plays a role in therapy evasion.

Single cell analysis and cancer

Historical methods to analyze tumors create a global view of tumor characteristics from bulk analysis of cancer and stromal cells within a tumor. Single cell analysis approaches in cancer research aim to identify and characterize complex cell phenotypes, isolate novel cell populations and dissect underlying cellular mechanisms of disease progression (Irish and Doxie, 2014). The advantage of this approach is the signature features specific to individual populations of cells can be identified, and features of a rare population of cells are less likely to be masque by more abundant cells. A more thorough discussion of single cell detection, quantification, and experimental considerations is discussed in detail in Chapter 2.

Single-cell RNA-seq, multiplex imaging, and cytometry analysis platforms have continually improved to meet the demand for single-cell analysis approaches. Single-cell RNA-seq provides a quantitative comprehensive view of the transcriptome of a cell, however, transcript levels don’t always correlate with protein expression (Koussounadis et al., 2015; Zhang et al., 2014a). Fluorescence-based multiplex imaging analysis can detect an array of proteins from single cells and their proximity to neighboring populations. However, single cell quantitative imaging in tissues is challenging with standard methods to

identify cell nuclei (Gross et al., 2016). Flow cytometry and mass cytometry simultaneously detect hundreds of cells per minute, and mass cytometry (CyTOF) detects >30 features without the need to correct for overlapping emission spectrum (Bendall et al., 2011; Bjornson et al., 2013; Leelatian et al., 2017a). For these reasons, mass cytometry was chosen as the primary analysis approach.

Flow and mass cytometry can yield an immense amount of data that traditionally requires a user to manually identify and group populations of cells with biaxial gating. While this approach is quick and easy to visualize, this approach may reveal differences in user gating, and less studied systems may contain heterogeneous cell populations overlooked by biaxial gating (Diggins et al., 2015). To meet this challenge high dimensional data has driven the development of several computational tools to facilitate subset visualization, discovery, and characterization where pairwise biaxial gating would be inefficient. To map a 2D representation of high-dimensional data, and conserve the structure of the data, dimensionality reduction tool viSNE has been adapted for flow cytometry and single cell RNA-Seq using the tSNE algorithm (t-distributed stochastic neighbor embedding) (Amir el et al., 2013). Dimensionality reduction tool viSNE has been shown to identify subsets of murine immune cells, tonsillar cells, and pancreatic cells (Becher et al., 2014; Wang et al., 2016; Wogsland et al., 2017). Furthermore, several clustering tools have been adapted for cytometry data to reduce human bias and facilitate novel subset discovery including SPADE, PhenoGraph, and FlowSOM (Levine et al., 2015; Qiu et al., 2011a; Van Gassen et al., 2015b). While many tools have been developed to dissect high dimensional data to define populations for downstream analysis, some approaches suffer from clustering

accuracy and computational efficiency in dense data sets. Among the many clustering algorithms tested with peer-reviewed data sets, performance comparison analysis has shown that FlowSOM had among the fastest runtimes and reproducible results (Weber and Robinson, 2016). Because FlowSOM and viSNE analysis have been shown to efficiently dissect heterogeneous cell populations, both tools were used in a sequential analysis workflow to visualize and discover cell subsets discussed in Chapter 5.

Addressing the need for single cell analysis in metastatic melanoma

Cutaneous melanoma is a serious skin disease thought to be derived from the pigment producing melanocyte cell (Mort et al., 2015). Unlike most malignancies today, incidence and death rates of melanoma continue to rise (Erdmann et al., 2013). Primary melanoma tumors that are diagnosed early are considered treatable with surgical resection. However, melanoma tumors have been observed to rapidly progress into late stage metastatic disease (Shaw et al., 1987). For those diagnosed with late-stage melanoma, the prognosis is poor, with median survival less than 10 months before the advent of targeted and immunotherapies (Sandru et al., 2014).

The primary risk factor for melanoma incidence is ultraviolet (UV) radiation from sunlight (Situm et al., 2007). It is thought that UV radiation contributes to melanoma disease progression through DNA damage and inflammation (Garibyan and Fisher, 2010). Furthermore, UVA radiation in sunlight has also been shown to mediate DNA damage through the formation of reactive oxygen species (Afanas'ev, 2010). Other than sunlight exposure, artificial UV lamps, drug induced photosensitivity reactions, and cosmetic ingredients are risk factors for melanoma formation (Volkovova et al., 2012). In addition to

environmental exposure, approximately 15% of melanoma cases occur in patients with a history of melanoma in their family (Goldstein and Tucker, 2001). To date, the germline mutations CDKN2A or CDK4 have been associated with an inherited predisposition for melanoma (FitzGerald et al., 1996). Finally, melanomas also display among the highest rates of mutation which could be an additional risk factor for malignant cells to arise (Lawrence et al., 2013).

Melanoma, are frequently associated with heterogenous features at both the genomic and proteomic level. Genetic heterogeneity has been thought to arise from ongoing genomic instability promoting the development of subclones and intratumor heterogeneity (Marusyk and Polyak, 2010). For example, intratumor heterogeneity in the expression of mutant BRAF and NRAS proteins, drivers of oncogenesis, have been observed in lesions from the same melanoma patient (Wilmott et al., 2012). Other than mutations, patterns of protein and gene expression have been identified in melanoma that correlates with melanoma cell proliferation and invasion. Within the same tumor, cells with a proliferating phenotype marked by expression of SOX10 and MITF have been observed alongside melanoma cells with an invasive phenotype characterized by expression of AXL (Verfaillie et al., 2015). Furthermore, heterogeneity in immune related genes, such as PD-L1 and human leukocyte antigen (HLA), is associated with differential responses to immune and targeted therapies (Madore et al., 2015; Reuben et al., 2017). Another important consequence of melanoma tumor heterogeneity is tumors with more diversity are less likely to respond to therapy (Reuben et al., 2017). Overall, cellular heterogeneity is an additional obstacle to the effective treatment of patients.

Before the introduction of targeted and immune therapies patients with melanoma were observed to be largely unresponsive to conventional chemotherapies. However, the discovery of BRAF mutations in 60% of patients' benign nodal nevi and metastatic melanoma lead to significant advancements in melanoma treatment (Hodis et al., 2012). BRAF mutations deregulate MAPK signal transduction and extensively alter transcriptional programs (Davies et al., 2002; Wan et al., 2004). BRAF inhibitors designed to target mutant BRAF have been observed to initially reduce tumor volume in melanoma patients with BRAF V600E mutation. However, most patients experience brief remission followed by progression (Chapman et al., 2011; Sosman et al., 2012). Due to the frequency of restored MAPK signaling observed after therapy, combination therapy with MEK inhibitors was hypothesized to reduce the likelihood of resistance to develop. While combination therapy successfully increased patient survival up to 12 months, patients invariably relapsed and suffered from increased symptoms of toxicity (Flaherty et al., 2012; Robert et al., 2015a). Other pathways are currently being evaluated as possible treatment strategies, however, long-lasting treatment responses with immunotherapy suggest curative treatment strategies will need to address suppressed immunity as well (Robert et al., 2017).

Melanomas are widely regarded as immunogenic and are observed to activate adaptive immune responses (Blankenstein et al., 2012). In melanomas, tumor associated antigens like MAGE or differentiation antigens like tyrosinase have been identified as specific target of cytotoxic T cell recognition (Kang et al., 1995; van der Bruggen et al., 1991). However, it wasn't until the recent success of immune targeted therapies, discussed in detail below, that the field embraced the idea that the immune system plays an important

role in melanoma treatment responses. T cell infiltration in melanoma tumors revealed patients had better long-term survival, however, characterization of T cell function revealed some cells displayed suppressed activity (Azimi et al., 2012; Baitsch et al., 2011). These observations support the hypothesis that the immune system is responsible for elimination of malignant cells. Today this hypothesis has developed into the immunoediting hypothesis that suggests the immune system protects against cancer development and influences the characteristics of the emerging tumor (Mittal et al., 2014). The mechanism of immunoediting consist of three phases of disease progression where cells escape elimination, establish equilibrium through dormancy, and escape via immunosurveillance or immune suppression (Mittal et al., 2014). Moreover, immune profiles of the microenvironment have revealed dynamic changes in immune cell content as disease progresses. High abundance of CD8 T cells and NK cells are observed during tumor dormancy, however, FOXP3 T regulatory cells and myeloid derived suppressor cells are present during disease progression (Wu et al., 2013). These observations have led to the creation of several types of immune therapies that aim to restore immune system dysfunction in melanoma.

To improve cytotoxic function of T cells, melanoma patients were treated with IL-2. While some patients exhibited loss of tumor burden, this approach came with high risk of toxicity (Kammula et al., 1998). IFN was introduced to increase immune recognition of malignant cells, however, the overall response rate was 23% (Alexandrescu et al., 2010). Vaccinations have also been utilized to improve immune cell recognition of melanoma. However, vaccinations against the melanoma antigen NY-ESO-1 revealed new tumors lost

the NY-ESO-1 antigen. This study provided evidence of that ongoing immune editing events enable the loss of immune surveillance (von Boehmer et al., 2013). Finally, adoptive transfer of T cells (ACT) is another major advancement for immune therapy that utilizes the expansion of autologous tumor specific T cells. After *ex-vivo* expansion of T cells and depletion of lymphocytes in the patient, tumor specific T cells are returned the patient (Bernatchez et al., 2012). In a clinical trial of melanoma, ACT therapy resulted in 51% of patients with complete or partial responses (Dudley et al., 2005). T cells engineered to express T cell receptors against tumor antigens have also been demonstrated to create long lasting responses to therapy (Robbins et al., 2011).

Monoclonal antibodies have become available that specifically target immune checkpoints that suppress T cell function. Checkpoint inhibitor anti-CTLA4 (ipilimumab) improved overall survival to 10 months, however, some patients failed to respond or began to show signs of auto-immune side-effects (Hodi et al., 2010). Anti-PD-1 and anti-PDL1 inhibitors have also been developed to restore cytotoxic T cell interaction with cancer cells. While both therapies increase patient survival, these therapies rely on pre-existing T cell infiltration, the presence of PDL-1 expressing cells, or free antigen to be effective (Mahoney et al., 2015). Due to the success of small molecule inhibitors and immunotherapies, the current therapeutic landscape for patients includes testing combination therapies containing a MAPK inhibitor and immune checkpoint inhibitor (Kim et al., 2014; Ribas et al., 2016).

The array of resistance mechanisms documented in melanoma after targeted therapies and immunotherapies, suggests multiple paths of branched evolution can initiate relapse (Hugo et al., 2015; Shi et al., 2014). In addition, many tumors may progress without

a clear genetic mechanism (Rizos et al., 2014). These observations suggest that several melanoma subsets that evolve to survive therapy are more likely to be responsible for relapse, and aggregate analysis of bulk tumor populations is insufficient to dissect the evolution of resistance. Technological advances have led to the development of several platforms to dissect tumor heterogeneity. For example, single cell transcriptional profiling of melanoma tumor cells has identified resistant cells in patients' melanoma tumors after relapse, however, these studies don't necessarily report overlapping cell phenotypes from relapse samples (Hugo et al., 2015; Tirosh et al., 2016). One hypothesis that could explain this observation is the time between remission and relapse enables persisting cells to develop a broad array of cellular phenotypes more fit to survive therapy.

This research introduces the application of mass and flow cytometry analysis to dissect melanoma diversity by measuring signaling proteins and proteins of cell identity. Ideally, by dissecting complex cellular phenotypes with multidimensional analysis tools, I aim to identify signature features of populations to track melanoma cell subsets that evade therapy. Since the most melanoma tumors exhibit significant loss of tumor burden followed by rapid progression, I hypothesized cells not eliminated would be identified by a consistent pattern of protein expression. The remaining Chapters in this dissertation build on this idea with a thorough primer of high dimensional single cell analysis in Chapter 2. Development of phosphow-flow analysis to dissect melanoma cell signaling networks, and cancer cell signaling features associated with immunotherapy prognosis in Chapter 3. Chapter 4 includes the systematic development of dissociation methods for solid tumors to release viable single cells into suspension for mass cytometry analysis. In Chapter 5 approaches

demonstrated in the previous Chapters were utilized to characterize dabrafenib and trametinib response in *BRAF*^{V600mut} melanoma. By simultaneously measuring several proteins in thousands of cells cytometry analysis revealed targeted therapy was revealed to clear Nestin-expressing melanoma cells, which are considered a hallmark of aggressive, metastatic melanoma. Persisting subsets after targeted therapy also lacked surface expression of MHC I, which may inform strategies for combining targeted therapy and immunotherapy. Together the work presented here provides a novel view of melanoma revealing new in vivo biology of melanoma cells that can be used as a reference point for patient-derived xenograft and cell line research models.

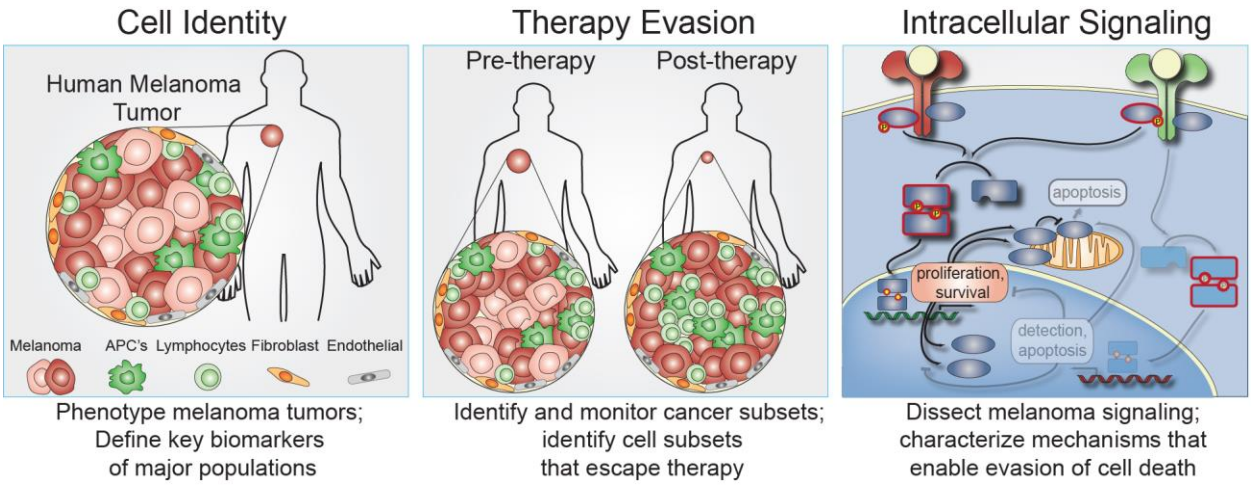

Figure 1-1 Single cell analysis of melanoma tumors. Mass cytometry analysis and other multidimensional analysis tools quantify key biomarkers of heterogeneous populations simultaneously with single cell resolution. Using >30 features any cellular biomarker can be quantified in heterogeneous cellular populations from tumors, xenografts, or early passage cell lines. Another advantage of cytomic approaches is that cytometry analysis can define key biomarkers of major populations, track therapy insensitive subset phenotypes, and dissect intracellular signaling pathways.

CHAPTER II

HIGH-DIMENSIONAL SINGLE-CELL CANCER BIOLOGY

Authors: Deon B. Doxie and Jonathan M. Irish

Reprinted by permission from Springer Nature: Springer, Berlin, Heidelberg, High-Dimensional Single-Cell Analysis. *Current Topics in Microbiology and Immunology,* Doxie DB and Irish JM. 2014

Preface

The study of metastatic melanoma and other cancers after relapse suggest, despite an initially favorable response to therapy, some patient's disease progresses because cancer subsets escape therapy. For this thesis research, I selected high dimensional cytometry analysis as the primary method to dissect and track cellular heterogeneity from hundreds of thousands of cells. The following chapter was written when mass cytometry and phospho-flow cytometry had not previously been applied to study cells from solid tumors. The review article was written to summarize the benefits and caveats of this approach, to update the field on new features that could be measured, and to introduce mass cytometry, which was also new at the time, having been introduced in 2011. The only published examples available were from blood cancer. However, the Future Directions section envisions application to study solid tumors. Thus, this chapter introduces in general how a single cell analysis approach enables a multiplex view of single cell identity, signaling proteins, cell cycle status, proliferation, apoptosis, and biomarkers of clinical relevance creating "single-cell systems biology" view of cancer. This review also discusses cytometry experimental methodology and explores several applications of cytometry techniques in a translational

cancer research setting. As novel treatment strategies continue to develop the content discussed here may bring valuable insight in evaluating therapeutic treatment responses. In summary, the review presented here describes the first step in my overall goal to identify and track cancer cell subsets that escape therapy.

Abstract

Cancer cells are distinguished from each other and from healthy cells by features that drive clonal evolution and therapy resistance. New advances in high-dimensional flow cytometry make it possible to systematically measure mechanisms of tumor initiation, progression, and therapy resistance on millions of cells from human tumors. Here we describe flow cytometry techniques that enable a 'single-cell systems biology' view of cancer. High-dimensional techniques like mass cytometry enable multiplexed single-cell analysis of cell identity, clinical biomarkers, signaling network phospho-proteins, transcription factors, and functional readouts of proliferation, cell cycle status, and apoptosis. This capability pairs well with a signaling profiles approach that dissects mechanism by systematically perturbing and measuring many nodes in a signaling network. Single-cell approaches enable the study of cellular heterogeneity of primary tissues and turn cell subsets into experimental controls or opportunities for new discovery. Rare populations of stem cells or therapy resistant cancer cells can be identified and compared to other types of cells within the same sample. In the long term, these techniques will enable tracking of minimal residual disease and disease progression. By better understanding biological systems that control development and cell-cell interactions in healthy and diseased contexts, we can

learn to program cells to become therapeutic agents or target malignant signaling events to specifically kill cancer cells. Single-cell approaches that provide deep insight into cell signaling and fate decisions will be critical to optimizing the next generation of cancer treatments combining targeted approaches and immunotherapy.

Contents

Introduction

Single-cell approaches reveal the heterogeneity inherent in primary tissues and tumors and provide the means to characterize complex phenotypes, isolate rare populations, and dissect underlying mechanisms. Especially critical for cancer research is the ability to track mutations and epigenetic events that confer hallmark attributes required for aggressive growth, malignancy, and therapeutic resistance (Hanahan and Weinberg, 2011). These changes impact network architecture and confer signatures that can be associated at the single-cell level with clinical features of each patient's disease (Irish et al., 2006a). Nearly all cellular features relevant for cancer research can now be measured on a per-cell basis (Table 1). A major advantage of a multidimensional, single-cell approach is that it allows determination of whether an abnormal trait in cancer, such as oncogenic signaling or a gene mutation, exists in all cells or is restricted to a cell subset (Fig. 1). As each piece of knowledge added per cell can dramatically improve the power to understand an experimental result (Krutzik et al., 2004), there has been a drive to expand the number of simultaneous per-cell measurements that can be made (Bendall et al., 2011; Perfetto et al., 2004). The creation of single-cell network profiling techniques has led to important breakthroughs in blood cancer, where flow cytometry techniques are straightforward to apply. There is an urgent need now to apply these tools more widely to the challenges of early detection and analysis of solid tumor cell signaling, tumor immunity, transformation to aggressive disease, and metastasis. High-dimensional flow cytometry approaches complement rapidly developing multiplex imaging cytometry tools (Gerdes et al., 2013; Gerner et al., 2012) and single-cell genetic tools (Kalisky and Quake, 2011; Wu et al., 2014). The promise of these techniques for precision medicine is great, but they also

create the challenge of integrating results from multiple high-dimensional, single-cell quantitative techniques. Here we provide a primer for applying high-dimensional, single-cell flow cytometry in translational cancer research.

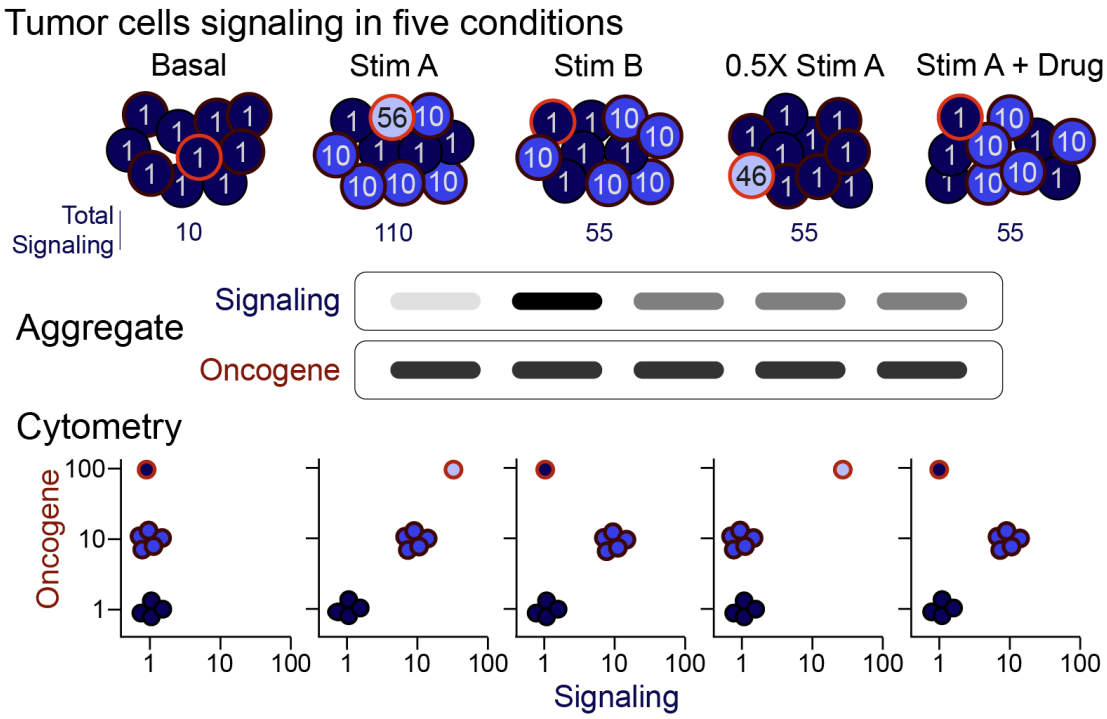

Figure 2-1. Multidimensional single-cell analysis pinpoints tumor cell signaling. In this example of 10 representative tumor cells analyzed under five stimulation conditions, oncogene expression marks three distinct populations of cells with contrasting signaling responses. In the top row, the number in each cell indicates the level of signaling in that cell under each condition. These values lead to the results shown as "Signaling". An aggregate analysis might mistakenly be interpreted to suggest that three of the conditions (Stim B, 0.5X Stim A, and Stim A + Drug) elicited the same signaling responses. However, the single-cell view reveals key subset-specific signaling differences. For example, the signal from Stim B is not half as effective as Stim A. Stim B is completely effective at stimulating one subset and ineffective at stimulating another. The oncogene-high cells are hypersensitive to Stim A and non-responsive to Stim B. Similarly, the partial effect of the Drug is due to complete inhibition of one subset and no inhibition of another. Adapted from (Krutzik et al., 2004).

Single-Cell Quantification of Cancer Hallmarks

A vast array of cellular features can now be detected by flow cytometry (Table 1). Using mass cytometry and other high-dimensional techniques enables sets of 30 or more of these features to be measured at the single-cell level simultaneously. Each new feature measured brings the potential to better dissect the cellular heterogeneity of a tumor (Fig 1). These features can be generally categorized as markers of cell identity, surrogate markers, and effectors. Effectors differ from surrogate markers in that they directly measure a mechanistically important part of a cellular process such as signaling (MEK phosphorylation), apoptosis (caspase 3 cleavage), or proliferation (cyclin D). Surrogate markers have been shown to correlate with an outcome under some circumstances but they are not thought to be effectors of that outcome. An example of a surrogate marker of cancer stem cells is CD133: CD133 does not confer stem-ness but rather tends to enrich for cancer stem cells. High-dimensional single-cell analysis allows simultaneous quantification of many effectors of different cellular processes in all major cell types present in a sample.

Table 2-1 Detecting cancer hallmarks in single cells

Cell property*	Example flow cytometry method (and referenced use in cancer)
Differentiation / Lineage	Antibodies against c-KIT (Wozniak and Kopec-Szlezak, 2004), CD34 (stem cells) (Holyoake et al., 1999; Robillard et al., 2005; Wozniak and Kopec-Szlezak, 2004); antibodies against CD38 (Robillard et al., 2005) or CD20 (Irish et al., 2010a; Robillard et al., 2005) and other cluster of differentiation (CD) antigens in human (Amir el et al., 2013; Mason et al., 2002; van Dongen et al., 2012) and mouse (Mayle et al., 2013; Van Meter et al., 2007) tumor and blood cancer tissue samples
DNA Content (aneuploidy, DNA fragmentation)	Propidium iodide (PI) (O'Brien and Bolton, 1995), ethidium monoazide (O'Brien and Bolton, 1995), or 7-actinomycin D (7-AAD) (Holyoake et al., 1999; O'Brien and Bolton, 1995) staining of DNA; flow cytometry and FISH to evaluate telomere length (Baerlocher et al., 2006); γH2AX foci indicating DNA double-strand break repair (Bourton et al., 2012; Huang et al., 2003); rhodium and iridium metal intercalators (Ornatsky et al., 2008)
RNA Content (quiescence)	Pyronin Y (Holyoake et al., 1999) staining of RNA
Cell Cycle Stage	Antibodies against cyclinD (Holyoake et al., 1999), cyclin A (Juan et al., 1998), cyclin B1 (Juan et al., 1998), cyclin E (Erlanson and Landberg, 1998); phosphorylated histone H3 (M phase) (Juan et al., 1998); all cell cycle stages (Behbehani et al., 2012)
Proliferation	Bromo-deoxyuridine staining for newly replicated DNA (Robillard et al., 2005); antibodies against proliferating cell nuclear antigen (PCNA) (Castillo et al., 2000), antibodies against Ki67 (Castillo et al., 2000; Holyoake et al., 1999); carboxy-fluorescein diacetate succinimidyl ester (CFSE) dye (Cooperman et al., 2004)
Oncogene Expression	Antibodies against BCL2 (Irish et al., 2010a; Laane et al., 2005; Robillard et al., 2005), c-MYC (Morkve et al., 1992), RAS (Andreeff et al., 1986)
Mutations	Antibodies against mutant p53 (Zheng et al., 1999), H-Ras-Val12 (Carney et al., 1986)
Tumor Suppressor Activity	Antibodies against p53 protein (Krutzik et al., 2004; Zheng et al., 1999) or p21/Waf1 promoter activity driving GFP (p53R-GFP system) (Ohtani et al., 2004)‡; antibodies against phosphorylated p53 (Irish et al., 2007; Krutzik et al., 2004) or phosphorylated Rb (Behbehani et al., 2012);
Apoptotic Cell Death	Antibodies against Caspase 3 cleavage products (Belloc et al., 2000)
Cell Membrane Changes, Viability, & Necrosis	AnnexinV (Belloc et al., 2000) staining for extracellular phosphatidylserine exposure, which occurs on apoptotic cells; detection of membrane permeability by PI dye exclusion (Nicoletti et al., 1991) or Alexa dye exclusion (Table 1); cisplatin exclusion (Fienberg et al., 2012)
Metabolism & Redox State	Dichlorofluoresceine diacetate (DCF-DA) staining (Armstrong et al., 2002), a measure of oxidation; monobromobimane (MBrB) staining (Chow and Hedley, 1995), a measure of glutathione; lipophilic fluorochrome dihexaoxacarbocyanine iodide (DiOC6(3)) (Belloc et al., 2000), a measure of mitochondrial membrane potential; mitochondria peroxy yellow 1 (MitoPY1), a fluorescent probe to quantify hydrogen peroxide levels in living cells (Dickinson and Chang, 2008)
Tumor Antigens	Antibodies against B (Timmerman et al., 2002) or T (Maecker and Levy, 1989) cell receptor idiotype; tetramers against tumor antigen (e.g., tyrosinase) specific T cells (Lee et al., 1999)
Signaling Activity	Antibodies against phosphorylated STAT and MAPK proteins (Irish et al., 2004b; Kotecha et al., 2008; Van Meter et al., 2007), phosphorylated NF-κB, AKT, S6, Src family kinases (SFKs), and many more (Bendall et al., 2011; Irish et al., 2010a); response to drug treatment (Bodenmiller et al., 2012; Krutzik et al., 2008); Indo-1 staining for Ca^{++} flux (Trentin et al., 2004); antibodies against IL-12 (Panoskaltsis et al., 2003), IFN-γ (Lee et al., 1999) or other cytokines

* Deep profiling enables >36 of such features to be measured on single cells (Bendall and Nolan, 2012; Bendall et al., 2012). Adapted from (Irish et al., 2006a).

In addition to measuring extracellular antigens or using live-cell permeable, non-toxic reagents, cytometry can quantify intracellular molecules and signaling activity in fixed and permeabilized cells, allowing targets in the cytoplasm and nucleus to be detected. Examples are intracellular targets are proteins with roles in metabolic potential (Armstrong et al, 2002, Chow and Hedley, 1995, and Belloc et al., 2000), phosphorylation induced signal transduction (Irish et al, 2004), and cytokine secretion (Panoskaltsis et al, 2003 and Lee et al, 1999).

As the technology to measure signaling has developed, it has aided in our understanding of computational modeling of biological networks in cancer. With the ability to quantitatively measure large sets of features simultaneously, this could lead to the systematic identification of clinically relevant signaling targets in a precision medicine setting where therapy is matched to the exact changes observed in the patient's cells. A single-cell view is critical to this, as drug responses in cell subsets are obscured when populations are analyzed in aggregate (Fig. 1).

Although a number of techniques can be used to measure certain features of cells, pragmatic concerns direct choice in many experiments. The detection techniques available to measure these features vary greatly in the amount of crosstalk that will be observed when measuring these features in combinations. A central challenge going forward is to quantitatively measure large sets of features in ways so that crosstalk between the measured channels is minimized. For example, loss of cell membrane integrity – a common surrogate for cell viability (Table 1) – should be routinely included and can be

measured many different ways that have different impacts on experiment design. In traditional flow cytometry, exclusion of fluorescent molecules like propidium iodide (PI) (Nicoletti et al., 1991), 7-aminoactinomycin D (7-AAD) (Schmid et al., 1992), and Alexa dye succinimidyl esters (SE) (Krutzik and Nolan, 2006) is commonly used to detect cells lacking an intact membrane. However, PI has very broad excitation and emission spectra that greatly limits the use of additional fluorochromes detected at >550 nm.

Table 2-2 Exclusion viability test using Alexa 700 succinimidyl ester (Ax700-SE)

Step	Details
Ax700-SE 50,000X Stock	Dissolve 1 mg Ax700-SE in 0.5 mL dimethyl sulfoxide (DMSO) to achieve a 50,000X long term frozen stock of 2,000 µg/mL. Store frozen and protected from water.
Ax700-SE 500X Aliquots	Prepare 500X frozen stocks of 20 µg/mL Ax700-SE in DMSO. A 20-µL aliquot is sufficient to stain approximately 50 experimental samples in 200 µL.
Ax700-SE 50X Working	Dilute Ax700-SE in DMSO to prepare a 50X of 2 µg/mL. Do not store.
Stain[†]	Add 4 µL of 50X working stock of Ax700-SE directly to cells in suspension to achieve a final concentration of 0.04 µg/mL. Stain for 10 min; titrate as needed.
Wash & Collect	Wash with 1X PBS[§] containing 1% bovine serum albumin (BSA) or other carrier protein. Pellet cells by centrifugation and continue with other staining steps or collect.

[†]Typically, live cells are stained prior to stimulation and no apparent impact on biology is observed. For a mass cytometry version using cisplatin, refer to (Fienberg et al., 2012).
[§]Sterile filtered phosphate buffered saline (PBS) without calcium or magnesium is recommended.

As an alternative to PI or 7-AAD, Alexa 700 SE (Ax700-SE) can be used as a viability test (Box 1) in a manner analogous to the fluorescent cell barcoding protocol previously described (Krutzik and Nolan, 2006). The Alexa dyes can be used to minimize crosstalk from the viability detection channel into other channels or to allow staining for other targets of interest on specific channels occupied by PI or 7-AAD. Sequential use of spectrally distinct Alexa dyes can be used to track changes in viability over time. In mass cytometry, a rhodium or iridium nucleic acid intercalator (Ornatsky et al., 2008) or cisplatin (Fienberg et

al., 2012) can be used in a similar manner to detect cells lacking an intact plasma membrane. Detection of dead cells is especially critical with working with necrotic tumor tissue and samples from patients undergoing therapy. While centrifugation at ~180 x *g* is typical for live cells, centrifugation at ~830 x *g* is recommended to effectively pellet dead and fixed cells.

It is often useful to measure cellular features that maintain tumor growth, such as proliferation, apoptosis, and cell cycle status (Table 1). Detection of bromo-deoxyuridine (BrdU) incorporation into newly replicated DNA (Robillard, 2005) and Ki67 (Holyoake et al., 1999 and Castillo et al., 2000), a protein strictly associated with proliferation (Scholzen and Gerdes, 2000), remain common indicators of proliferation. Apoptotic cell death is frequently measured by activation of the cleaved caspase 3 or by analysis of cell membrane changes like phosphatidylserine exposure (Belloc et al, 2000). In addition, experimental drug studies with chemotherapeutics and ionizing radiation have shown that cell cycle status plays a major role in maintaining tumor homeostasis. Cytometry has explored the therapeutic implications of cells in various states of the cell cycle by revealing quiescent cells kept in a drug-tolerant state. These cells can be identified by pyronin Y staining of RNA or by the abundance of cyclins that regulate cell cycle status (Holyoake et al, 1999, Juan et al, 1998, and Erlanson and Landberg 1998). To delineate cell cycle stages by mass cytometer, 5-iodo-2-deoxyuridine (IdU) is used to mark cells in S phase and G0/G1 cells are detected using antibodies against retinoblastoma protein (Rb) phosphorylated at serines 807 and 811 (Behbehani et al., 2012).

Dissecting Abnormal Signaling Networks

Genetic and epigenetic alterations in cancer cells lead to sustained changes in basal signaling and signaling responses (Fig. 2). The vast majority of driver mutations in cancer effect profound changes in cell signaling networks (Irish et al., 2006a). These observations indicate that differential activation of signaling pathways play critical roles in determining a cell's chance for survival or death. Epigenetic changes are also a potent force in shaping the structure of signaling networks in healthy development and cancer. Gain or loss of intercellular signaling interactions, activation of receptors whose signaling controls cell identity, and drug treatments can all trigger sustainable patterns of signaling that persist through cell division or isolation of those cells in culture. Epigenetic reprogramming of signaling networks is a primary mechanism of patterning in healthy development. B and T lymphocytes are an exception in that genetic changes are a mechanism driving healthy development and differentiation. As tools to sequence DNA and RNA continues to improve in speed, read depth, and single-cell precision (Dalerba et al., 2011; Marcy et al., 2007; Powell et al., 2012; Wu et al., 2014), genomic and proteomic tools for studying signaling network activity, transcription factor binding, and DNA methylation typically require tens of millions of cells for one test and are restricted to aggregate analysis (Fig. 1).

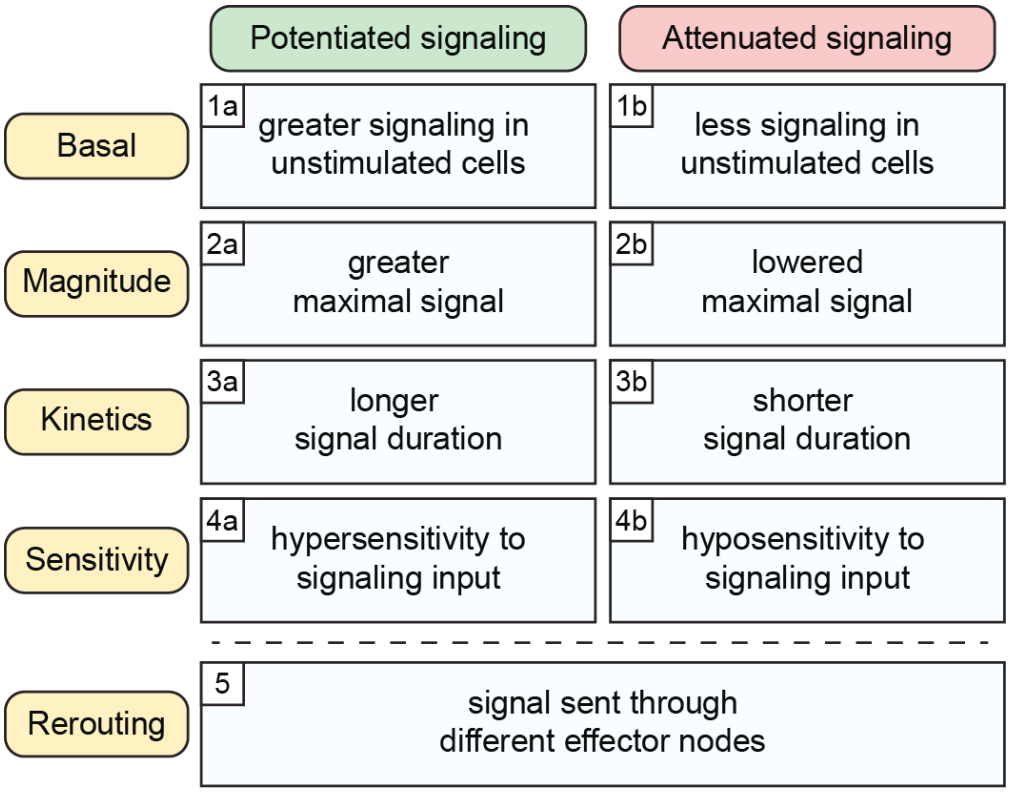

Figure 2-2 Abnormal signaling in cancer cell networks. Gains and losses of signaling drive oncogenesis and tumor progression. This figure classifies commonly observed signaling alterations according to direction (potentiated or attenuated) and mechanism. Basal signaling disruptions are commonly observed in cancer cells, and the signaling networks of the most negative prognostic cells typically display altered responses to environmental cues. Refer to (Irish et al., 2006a) for example cancer hallmark signaling changes conferred by gene mutations.

High-dimensional flow cytometry addresses this critical technology gap by quantifying single-cell epigenetic changes encoded by altered signaling mechanisms that transform cell function and fate (Fig. 2). Abnormal signaling in cancer can be viewed as changes in the function of signaling nodes within a network (Irish et al., 2006a). These changes are encoded by mechanisms such as constitutive basal activation of an oncogenic kinase (Fig. 2, 1a), loss of a tumor suppressor phosphatase (Fig. 2, 1b), or hypersensitivity to growth factor stimulation (Fig. 2, 4a). The signaling event can be either potentiated (strengthened)

or attenuated (weakened), and these changes can have dramatic impacts on the overall function of the signaling network and the cell. Example signaling alterations in cancer that represent these mechanisms are highlighted in the following sections of this chapter.

To understand changes in regulation of signaling it is important to determine how signaling responses differ in cancer cells. A starting point to consider before analyzing a cell's entire signaling network is to identify signaling inputs that individually activate signaling nodes. In this method, cells treated with a stimulus always serve as positive controls for signaling activity, whereas cells in a basal state function as negative controls. For constitutively active pathways, use of signaling node inhibitors may be necessary. Attention to the inhibitor specificity and concentration should considered, as the signaling response may be the result of off-target effects in a signaling network (Bodenmiller et al., 2012). With this methodology, it is possible to reveal clinically relevant signaling profiles by comparing signaling networks among patients with different clinical outcomes (Fig. 3).

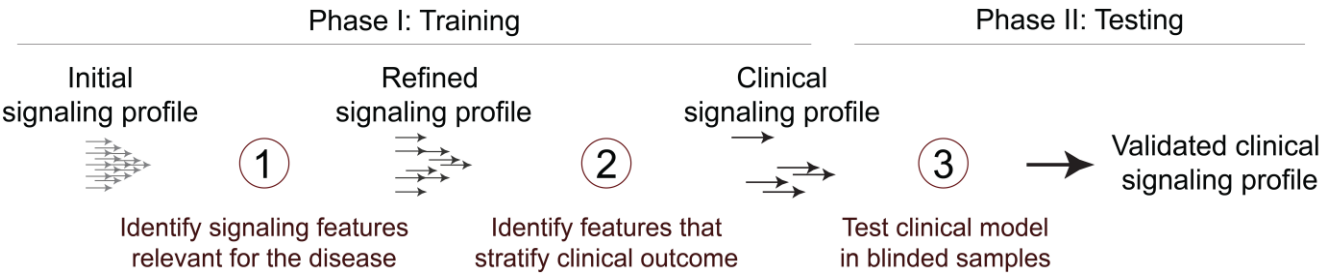

Figure 2-3 Discovery and validation of a clinical signaling profile. During the training phase, many hypotheses are tested as signaling is assessed at many nodes under a large number of conditions (basal, various signaling activators, doses, time points, drugs, and combinations). The signaling profile is then refined by determining which features differed in the experimental group (cancer) relative to controls (healthy). This feature selection step is based on the biosignature hypothesis (Irish et al., 2004a), which proposes that features that vary as much in the control group as they do in the experimental group are not likely to

productively contribute to unsupervised stratification because they are not specific to the experimental group. Models based on one or more features are then built, and it is determined whether they stratify a feature of interest such as clinical outcome. This clinical signaling profile is then tested in a new set of samples comparable to the first and balanced for potential confounders. Ideally the test is performed by a new investigator or a computer algorithm that is blinded to the outcomes.

There are two main phases in the generation of a validated signaling profile (Fig. 3): (1) the training phase, which has the goal of hypothesis generation and new discovery and (2) the testing phase, which is a focused challenge of a small number of hypotheses identified during testing. Development of a signaling profile begins with assembling a list of measurable features and deciding how to organizing the staining panels to maximize the information gained while minimizing issues like channel crosstalk. Features are then selected according to the biosignature hypothesis, refined for clinical relevance, and tested in a new set of samples (Fig. 3).

Single Cell Detection, Diagnosis, and Prognosis

Cancer cells are genetically unstable and subsets of cancer cells emerge over time during tumorigenesis, thus the ability to measure multiple biomarkers per cell is particularly valuable. It is common for cancer cells to resemble non-malignant tumor infiltrating cells of the same lineage (Fig. 4). In this example from B cell follicular lymphoma, expression of CD20, the oncogene BCL2, and BCR light chain isotype (κ or λ) were all used to distinguish tumor B cells from non-tumor host B cells. Normally B cells exhibit a mixture of κ and λ light chains, but in lymphoma it is common for >95% of B cells to be a clonal expansion of a cancer cell with just one isotype. In a simple four-color panel it is possible to detect three identity markers and one phospho-protein signaling event (Fig. 4). Here, greater than

normal ERK, BTK, SYK, and p38 signaling responses were identified specifically in the tumor B cells. Along with a greater magnitude of signaling potential, tumor cells sustained signaling for a significantly longer period (Irish et al., 2006c). This and other studies of BCR signaling in cancer have highlighted BCR signaling as a target for therapeutic discovery (Rickert, 2013). Recently, targeting BTK has shown great promise in B cell malignancies (Byrd et al., 2013; Wang et al., 2013).

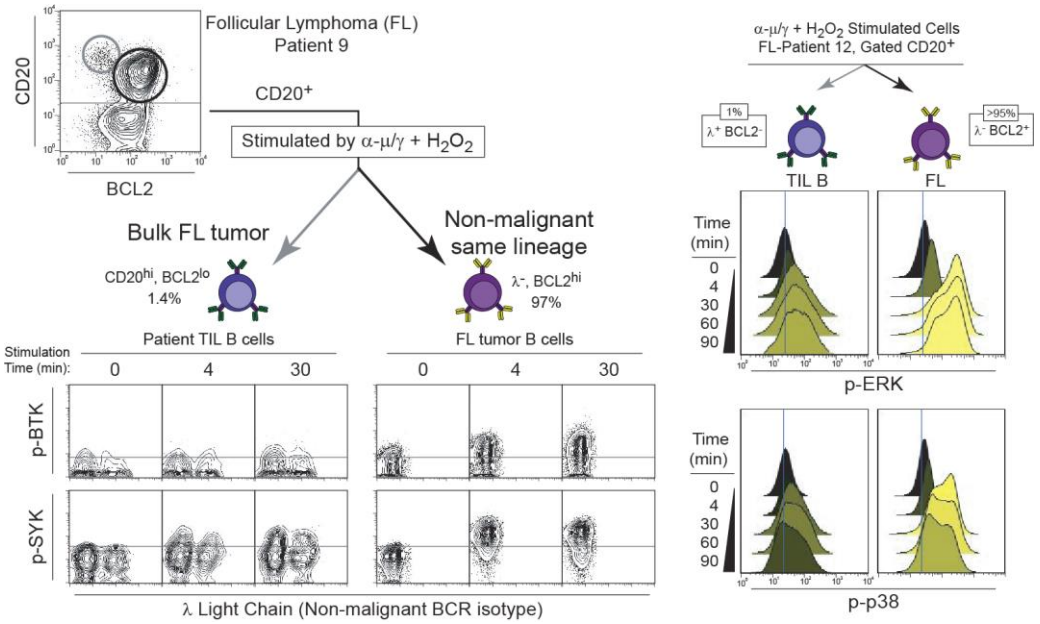

Figure 2-4 Identifying contrasting signaling in cancer and non-malignant cells of same lineage cell within a tumor. In this example, non-malignant tumor infiltrating lymphocyte (TIL) B cells are detected within follicular lymphoma B cell tumors from two patients. On the left, non-tumor cells were identified by the expression of the "wrong light chain" – a B cell receptor immunoglobulin light chain of a different isotype from the clonal tumor – combined with high CD20 expression and a lack of BCL2 expression. Here we can see that these cells have a distinct SYK and BTK signaling profile that contrasts with the bulk tumor. The histogram overlays on the right show potentiated magnitude and kinetics of ERK and p38 phosphorylation in lymphoma B cells (right side, $BCL2^+$) vs. TIL B cells (left side, identified as λ^+ non-tumor light chain and $BCL2^-$).

A key advantage of mass cytometry is that many surface and signaling markers can be simultaneously detected. In the fluorescence example (Fig. 5), different individual signaling readout were repeated paired with the same three cell identity markers across four redundant staining panels in order to measure four phospho-proteins. A critical problem with this approach is that one cannot compare signaling vs. signaling in the same cell – the comparison must be made at the population level. With mass cytometry, 20 markers of identity can be paired with 14 phospho-proteins in a 34-dimensional panel. This removes redundant staining panels, conserves sample, and creates higher quality data. In cases where altered signaling distinguishes cancer cells from healthy cells (Fig. 4 and Fig. 5), mass cytometry may make it possible to quickly and accurately diagnose patients based on a flow cytometry signaling profile.

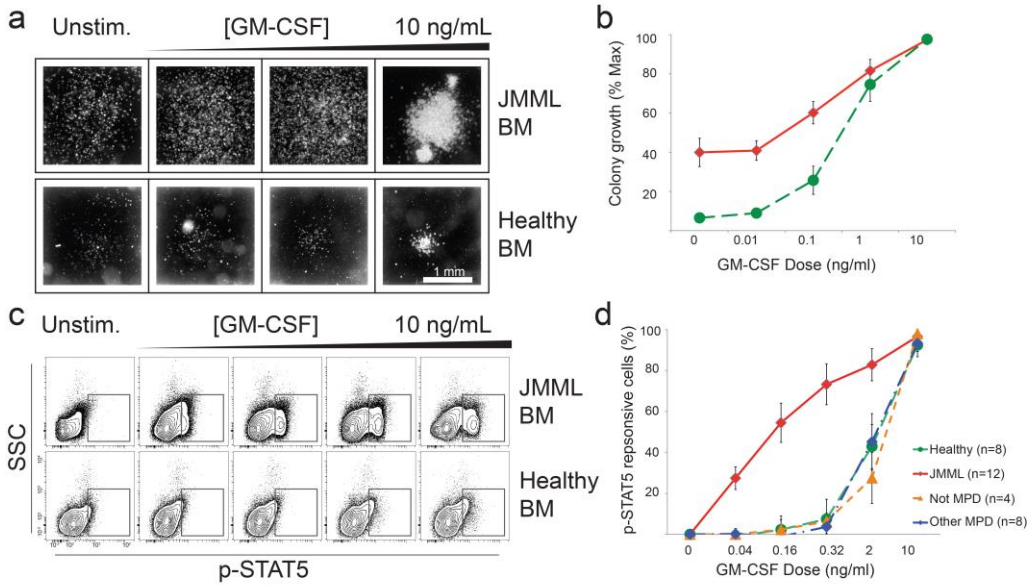

Figure 2-5 Hypersensitivity to a signaling input is diagnostic for JMML. Previously, 3-4 weeks were required to confirm a suspected diagnosis of JMML with a granulocyte-macrophage colony-forming units (CFU-GM) assay. In the CFU assay, bone marrow cells from healthy donors (green curve) and patients have different responses to GM-CSF. b Plot of colony growth vs. GM-CSF dose in healthy volunteers (green) and

patients (red). c By flow cytometry, a hypersensitive population of JMML cells is detected in cancerous bone marrow compared to the normal control. d A dose-dependent increase in hypersensitive activity of p-STAT5 uniquely distinguished JMML from other myeloproliferative disorders as well as healthy patients. Adapted from (Kotecha et al., 2008).

Juvenile myelomonocytic leukemia (JMML) has historically diagnosed and confirmed with a granulocyte-macrophage colony forming units (CFU-GM) assay (Fig. 5). The disadvantage of this approach is 3-4 weeks are required to confirm the diagnosis when the potentially curative therapy for JMML is an early allogeneic stem cell transplant. Previously, studies with JMML patient samples and mice suggested GM-CSF responses are necessary for the pathogenesis of JMML, but the role of STAT5 activation had not been investigated. In a study that used single-cell profiling of JMML patient blood and bone marrow samples, a small proportion of $CD33^{+}$, $CD14^{+}$, $CD38^{dim}$ cells exhibited hypersensitive p-STAT5 responses in response to sub-maximal concentrations of GM-CSF (Kotecha et al., 2008). This diagnostic approach was recently independently validated (Hasegawa et al., 2013). Thus, phospho-flow cytometry provides a precise readout for the aberrant signaling in JMML that distinguishes JMML from both healthy subjects and from patients with other myeloproliferative disorders. Analysis of cell subpopulations associated with disease opens opportunities for quick detection of minimal residual disease (MRD) and has potential to assess therapeutic resistance (Kotecha, 2008). The application to MRD is especially important in the clinical setting of cancer chemotherapy, and a vital need exists for flow cytometry tools that track and automatically identify MRD using surface markers or signaling events (Amir el et al., 2013).

Predicting Therapy Response and Tracking Evolution

Surface and signaling-based single-cell analysis can track the abundance of malignant cells at diagnosis and spot the emergence of drug-resistant cells over time during treatment. An example of this is the detection of a clinically significant tumor cell subset of lymphoma cells defined by altered BCR signaling (Fig. 6). Following α-BCR stimulation, several phospho-epitopes had impaired BCR signaling responses in a subset of cells termed lymphoma negative prognostic (LNP) cells. The presence of BCR-insensitive LNP cells was negatively correlated with overall patient survival and LNP cells increased in abundance following treatment and disease progression (Irish et al., 2010a). These results indicate that BCR-insensitive LNP cells may have a selective survival advantage compared with bulk tumor B cells (Fig. 6). The close associations between the signaling profiles and risk of death, strongly suggest that these cells are therapy insensitive due to specific changes to cell signaling. Perturbing cells with an input stimulus to observe differential activation of signaling networks in cancer has repeatedly been shown to stratify survival (Irish et al., 2004a; Irish et al., 2010a).

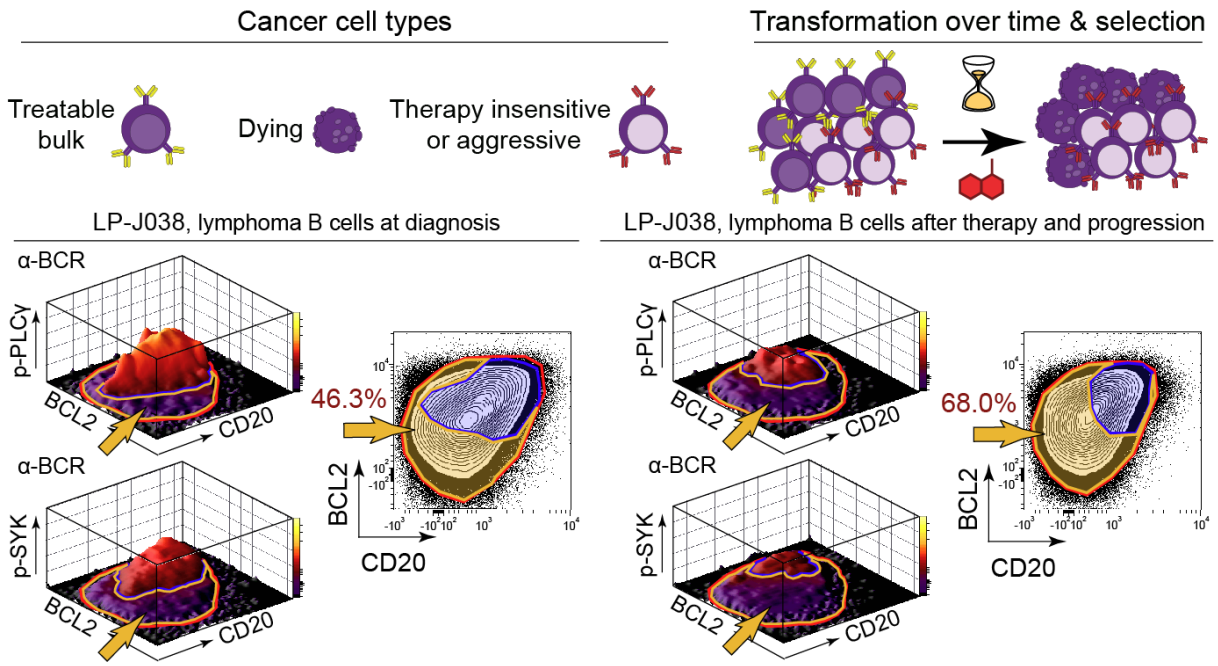

Figure 2-6 Emergence of a negative prognostic subset over time following treatment. In this example, LNP tumor cells from lymphoma patient J038 are distinguished by abnormal SYK and PLCγ signaling and differential BCL2 and CD20 expression (gold arrow). At the time of diagnosis, LNP cells constituted only 46.3% of the tumor cells. After therapy and disease progression, LNP cells increased to 68% of the tumor. Each 1% increase in LNP cells is associated with a 2.5% increased risk of death in the following year ($p < 0.000005$, z-score = 4.68). Adapted from (Irish et al., 2010a).

Targeted cancer therapies have advanced rapidly as our understand of cancer cell-specific signaling alterations has increased (Irish et al., 2006a). Genomic technologies can now identify patterns of gene expression or detect the presence of novel point mutations in a case-by-case basis. This has led to the identification of tumor subclasses and improved understanding of disease biology for appropriate therapies. For example, targeting the overexpression of HER2 with lapatinib or trastuzumab in breast cancer has benefited patients. Similarly, identification of BCR-ABL kinase and the use of imatinib mesylate (Gleevec) has aided in treatment of chronic myeloid leukemia. However, it can be difficult to target newly discovered mutations, and separating drivers from passengers can be

challenging when normal, pre-, and post-treatment sample sets are not available. In contrast, the signaling events measured in phospho-flow panels are typically highly targetable, and in many cases there are drugs available that are already being used in the clinic in other settings.

An alternative strategy is to measure deregulation of an oncogenic pathway by measuring active kinase signaling and a cell networks signaling potential when perturbed (Fig. 7). For example, signaling alterations that predict therapy outcome are observed in acute myeloid leukemia (AML) patient samples. Increased activity of STAT5 and STAT3 activity are known to induce the expression of genes for survival and proliferation. Interferon γ treatment activates STAT1 activity, which can oppose survival by activation of genes involved in antigen presentation to the immune system. Cells from patients who did not respond to induction chemotherapy shared a profile including a critical failure to phosphorylate STAT1 in response to interferon γ (Fig. 7, Therapy-resistant AML cells). Instead of activating STAT1, these cells have rerouted IFNγ signaling to phosphorylate oncogenic STAT5. These results provide a rationale for the investigation of STAT5 inhibition in therapy-resistant AML to improve the outcome of patients with this resistant subset. Thus, a key promise of the signaling profile approach is that observed cancer-specific signaling disruptions are required for cancer cell survival or aggressive behavior.

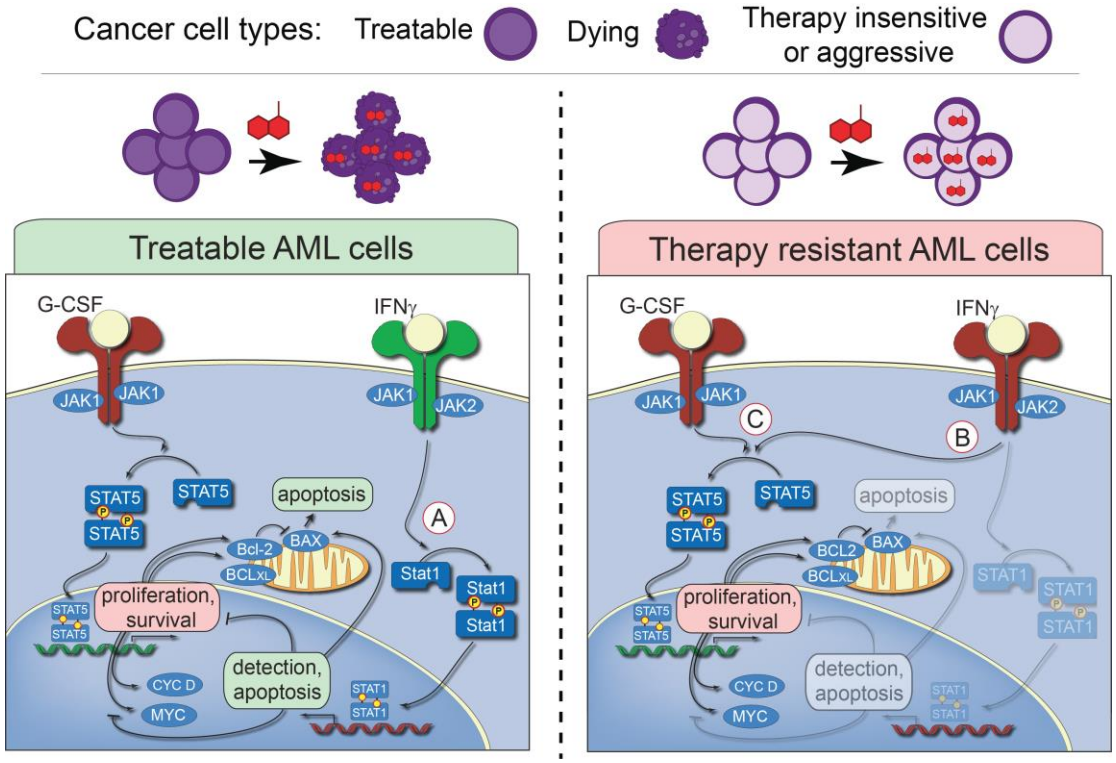

Figure 2-7 A hallmark mechanism of AML therapy resistance is rewired JAK/STAT signaling. In this example, signaling profiles of two different AML cancer cells are shown. In treatable AML cells, G-CSF signaling through JAK1 and induction of STAT5 phosphorylation mediates transcription of pro-survival and proliferation genes. Conversely, IFNγ signaling through JAK2 results in induction of STAT1 phosphorylation that mediates cell cycle arrest and apoptosis. In the signaling network of the therapy resistant AML cell, the response to IFNγ has become rerouted to STAT5, which, like G-CSF, mediates transcription of pro-survival and proliferation genes. The lack of functional STAT1 activation, which activates cell cycle arrest induced apoptosis, explains why patients with these cancer cells are often resistant to DNA-damage-induction therapy. Inhibition of JAK2/STAT5 signaling in therapy resistant AML cells could potentially improve the outcome of patients with this resistant subset.

A primary challenge in high-dimensional profiling of heterogeneous cells is optimization of a staining protocol that facilitates the detection of extracellular and intracellular targets of the cells. A target's localization should be considered and a range of appropriate reagents tested in order to develop a protocol that balances speed, reproducibility, and sensitivity.

Optimizing signal to noise remains a central goal in fluorescent flow cytometry (Maecker and Trotter, 2006) and mass cytometry (Bendall et al., 2012). This may involve titrating the detection of the target on live cells, after para-formaldehyde fixation, and/or after permeabilization (e.g., methanol, ethanol, saponin, Triton X-100) of the cell membrane (Krutzik and Nolan, 2003). Panels that measure all features except one are a classic flow cytometry control termed 'fluorescence minus one' (FMO), described in detail by Maecker and Trotter (Maecker and Trotter, 2006). For mass cytometry, a comparable 'mass minus one' (MMO) control is equally valuable for determining what level of signal can reliably be considered positive.

When creating multi-step staining protocols for detection of extracellular and intracellular epitopes, a key advantage of small molecule dyes and the polymer metal chelators used in mass cytometry is that they are not sensitive to the common permeabilization agents. This contrasts with large protein fluorophores; fluorescence of protein fluorophores can be harmed by harsh alcohol treatments used in storage of fixed samples and during permeabilization. In mass cytometry, a multi-step staining protocol is a common alternative to seeking epitope unmasking staining conditions that work well for a variety of epitopes that are localized in different cellular compartments and differentially dependent on three-dimensional conformation. In a typical signaling experiment, surface marker staining occurs after the cells have been fixed so that detection of cell identity does not alter signaling. However, since many surface marker target epitopes are no longer detectable following harsh permeabilization conditions, surface staining occurs immediately following the short fix step that stops signaling in the phospho-flow protocol (1.6% paraformaldehyde

for 5 minutes at room temperature). Thus, surface staining occurs following stimulation/fixation and prior to methanol permeabilization. For more information, see Table I (Krutzik et al., 2005) and Fig. 2 (Krutzik and Nolan, 2003). For certain intracellular targets – especially transcription factors – permeabilization with saponin or Triton X-100 can yield superior staining. Usually a short formaldehyde fix (≤ 10 minutes) does not destroy target epitopes and detection of surface markers is decreased by an acceptable ~10% of the original signal, although there are exceptions.

Antibody titration and staining optimization should follow well-established guidelines (Box 1). It is critical to titrate antibodies in the exact conditions that they will be used and to include populations of positive and negative control cells at known ratios. The stain index between positive and negative cells allows verification of the subset pattern. It is not sufficient to titrate an antibody on a uniform positive population while using unstained or isotype control stained cells as a comparison point. It is acceptable for the positive and negative cells to be in different tubes, but the advantage of staining all the cells simultaneously in multidimensional cytometry is lost. With intracellular work: less is more. Problems are typically due to over-staining, which leads to non-specific background signal (see Figure 2 in (Krutzik and Nolan, 2003)). Antibodies that work well by immunofluorescence nearly always are suitable for fluorescent flow and mass cytometry when the same fixation, permeabilization, and staining conditions are used.

Box 1 | Guidelines for titrating antibodies
1) Titrate antibodies in house using actual experimental conditions. 2) Mix positive and negative cells to create a signature pattern for titrations. 3) Use well characterized cells for titrations (not rare cells of interest). 4) Select optimal instrument channels for titrating reagents. 5) It may be necessary to titrate multiple clones under multiple perm conditions for intracellular epitopes that have not been widely studied.

For all types of cytometry, internal biological control populations are ideal controls. Intracellular controls transform the cellular heterogeneity that confounds aggregate approaches (Fig. 1) into a distinct advantage of single-cell approaches. Markers of stem-ness, such as CD34 (Woziniak and Kopec-Szlezak, 2004), and lineage-restricted molecules expressed during differentiation (Mason et al., 2002) help determine the identity of tumor cells. However, developmental programs can be aberrantly activated or suppressed in both the cancer cells and the surrounding microenvironment. Because phenotypic plasticity characterizes cancer, it is especially valuable to have multiple markers that are expected to be positive and negative on each major tumor and host-cell population. A general rule is to include two positive markers and one negative marker for each major tumor and host cell type (Irish et al., 2010a). Negative markers help rule out artifacts. In immune cancers, markers of clonality can be used to confirm cancer cell identity or dissect cancer cell lineage (Green et al., 2013; Irish et al., 2006c; Sachen et al., 2012). Cell isolation by fluorescence-activated cell sorting followed by sequencing for oncogenic mutations can confirm the identity of cancer cells or be used to identify underlying driver and passenger mutations (Green et al., 2013). Ultimately, the more features detected (Table 1), the more confidence one has in the identity and biology of a given population

during the discovery or training phases of a project (Fig. 3). Cytometry provides the toolkit for tracking and characterizing the ubiquitous heterogeneity of cancer.

The dysregulated intracellular signaling observed in cancer cells contrasts greatly from signaling in normal cells. Challenging of the cancer cells with perturbation reagents can reveal divergent response patterns. Even when the mechanism is not directly inferable, analysis of multiple signaling events can identify the point in a cellular system that is dysregulated. To develop a protocol that profiles signaling responses, comparisons to a healthy population of cells, such as peripheral blood mononuclear cells or a tractable genetically modified cell line, often establishes a comparison point for how intracellular systems should behave.

After acquiring a large dataset, data interpretation can be a challenging hurdle in high-dimensional experiments. Traditional multi-parameter techniques like flow cytometry have relied upon two-dimensional plots to visualize the data to understand correlations between the parameters. Unfortunately, as the number of parameters increase, the number of two-dimensional plots increase to create an overwhelming visualization problem. Analytical approaches developed to tackle this complexity include dimensional reduction tools such as SPADE (Bendall et al., 2011; Qiu et al., 2011b) and viSNE (Amir el et al., 2013). To achieve a greater understanding of tumor proteins and signaling, these tools can be used to then computationally compare this new view of cancer across patients and tumor subtypes.

Future Perspectives

Going forward, the field must address a number of challenges in data analysis and platform integration raised by the increased power to simultaneously detect many features of single cells. Four key areas are:

1) Data analysis, storage, and sharing with collaborative teams.
2) Cross-platform comparisons with other systems biology techniques.
3) Cross-scale data integration, especially between single cells and aggregates.
4) Comparisons across time, especially in clinical studies.

Technical tools and experimental designs have far outpaced the existing computational tools. Many are working to address this need, but it is important to go beyond the basic challenge of clustering groups of cells by similar features. Tools for identification of populations within single-cell datasets have increased dramatically in sophistication and speed (Aghaeepour et al., 2013; Amir el et al., 2013; Pyne et al., 2009; Qiu et al., 2011b), and now there is an urgent need for tools that model the populations and derive biological meaning from the markers used to find populations. It is critical to make sure that tools do not find populations in such a way that they are limited to a particular dataset. This is vital for reproducibility as well as for clinical application. In the end, it is critical to define the difference metric in terms of the underlying biological mechanisms and to refine the model to the minimal parts for clinical testing.

How do we connect measurements made at the single-cell level with knowledge gained using other aggregate analysis tools? Single-cell techniques have essentially been

developing independently of aggregate analysis tools because it unclear how to connect the information gained at such different scales. Thus, approaches to span experimental platform and biological scale are sorely needed for the next generation of single-cell opportunities in cancer biology (Fig. 8).

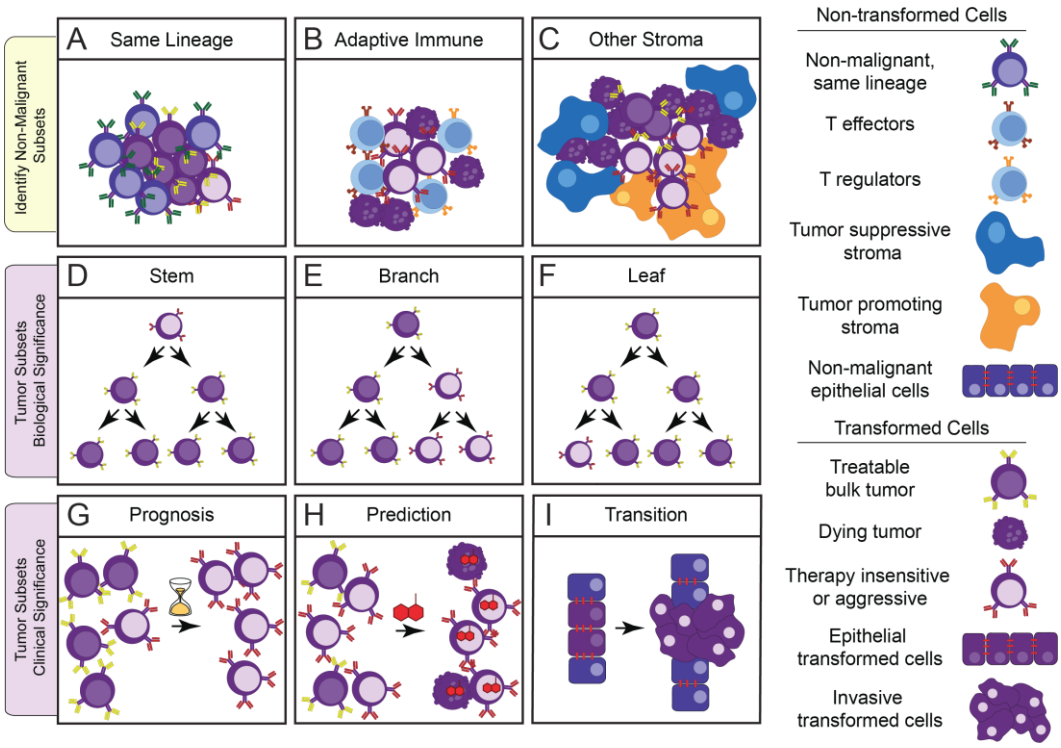

Figure 2-8 Key single-cell opportunities in cancer research. The first row depicts the opportunities of detecting non-malignant cells of the same lineage as the tumor (A, as in Fig. 5), tumor infiltrating immune responders (B, as in (Myklebust et al., 2013)), and other non-malignant stromal cells (C). It will be important to distinguish between abnormal signaling that promotes cancer, such as inflammation, and abnormal signaling that results from cancer, such as T cell suppression via PD-1 or generation of cancer associated fibroblasts (Barcellos-Hoff et al., 2013). In the second row, (D), (E), and (F) depict contrasting biological origins of an aggressive, therapy-insensitive tumor subpopulation that can be dissected with single-cell tools. A gatekeeper mutation conferring resistance to targeted therapy might be an apomorphy that distinguishes a rare 'leaf' subset (F). Alternatively, a slow cell cycle phenotype might distinguish a cancer stem cell (D) (Reya et al., 2001). A large, heterogeneous branch (E) observed at the time of diagnosis might need to be treated with a combination of therapies in order to kill all populations and obtain a clinical response. The third row depicts clinical single-cell opportunities, such as detecting negative prognostic subpopulations (G, as in Fig.

7), treatment insensitive subsets (H), and cellular transitions as would be observed when epithelial cancer cells become an invasive, metastatic population (I).

Increasingly, single-cell tools will need to take into account changes over long periods of time – such as is the case with samples obtained over time during treatment. The concepts of before and after treatment and of subset evolution, emergence, transformation, and metastasis must be considered. What are reliable markers of stable cellular identity and how do we track ‘a population’ of cells over time?

CHAPTER III

MELANOMA SIGNALING AND NOVEL IMPLICATIONS FOR IMMUNOTHERAPY PROGNOSIS

This work consists of unpublished data and peer-reviewed published data from Johnson et al. *Nature Communications* 2016.

Preface

In the past, cellular heterogeneity in cancer has been studied to identify novel genomic alterations in cell subsets that drive cancer oncogenesis or therapeutic resistance. However, epigenetic changes are also a potent mediator of healthy and cancer cell development. Genetic alterations and epigenetic changes have the potential to affect cell signaling and regulate transcriptional events. To date, characterizing and targeting cell-signaling events has been utilized therapeutically to modify cellular behaviors including immunosurveillance, cell fate, proliferation, and cell identity. In this chapter, a phospho-flow assay was developed to dissect phosphorylation-induced signaling in melanoma cells. Furthermore, this approach was utilized in collaboration with Dr. Doug Johnson and Dr. Justin Balko where we identified MHC-II tumor phenotype as a prognostic feature of patients with melanoma after anti-PD-1 immunotherapy. My role in this work identified a potential signaling mechanism associated with the poor immuno-therapy prognosis phenotype. This work illustrated that extracellular protein expression and signaling activity can be used to identify clinically relevant melanoma subsets. The methods development work for this chapter included application of phospho-flow to adherent melanoma cell lines.

This was a novel application of the phospho-flow technique. This method was useful to develop for this thesis, as I subsequently applied solid tumor phospho-flow to measure signaling in the cells from primary human melanoma tumors (Chapter 5). In addition, this work provided support for including MHC II and MHC I in the studies in Chapter 5.

Melanoma signaling and clinical resistance to therapy

Protein phosphorylation signaling events are the direct result of genetic and epigenetic alterations that determine a cells chance for survival, proliferation, and death. In melanoma, oncogenic phosphorylation events induced by mutant BRAF kinase are found in >60% of melanoma. However, resistance to mutant BRAF targeted therapies and other single target therapies has emerged as a key clinical problem caused by additional signaling alterations (Hodis et al., 2012; Van Allen et al., 2014). Resistance to BRAF and MEK targeted therapies is frequently driven by reactivation of MAPK signaling after therapy. The discovery of MEK mutations, expression of BRAF splice variants, expression of phosphatase COT, and BRAF amplification have all been shown to reactivate MAPK signaling (Johannessen et al., 2010; Rizos et al., 2014). In addition to MAPK signaling, oncogenic PI3K/AKT signaling, receptor tyrosine kinase signaling, cyclin-dependent kinase signaling, and STAT3 signaling cascades have been observed after targeted therapy (Girotti et al., 2013; Johnson et al., 2014; Paraiso et al., 2011; Smalley et al., 2008).

Immunotherapies are the most recent innovation in the field of melanoma treatment, and clinical resistance mechanisms are a field of ongoing investigation. However, recent research has identified MAPK signaling, loss of PTEN, activation of WNT/ βcatenin, and loss of interferon sensitivity as cell-intrinsic signaling mechanisms that mediate immunotherapy resistance. MAPK signaling has been shown to increase expression of PD-L1 and VEGF which have been shown to suppress T cell engagement and inhibit T cell trafficking (Liu et al., 2013; Sumimoto et al., 2016). Loss of PTEN and activated PI3K signaling has been shown to increased immunosuppressive cytokines in preclinical models of melanoma (Peng et al., 2016). Loss of interferon sensitivity and dysregulation of the JAK/STAT signaling pathway has been shown to decrease antigen presentation and block apoptotic signaling in melanoma (Pansky et al., 2000). Furthermore, JAK1/2 mutations have been shown to mediate antibody-based immunotherapy resistance by suppressing immune engagement genes and STAT1 signaling (Shin et al., 2017; Zaretsky et al., 2016). Because signaling is at the cross-section of many cellular resistance mechanisms, continuing to study and target signaling should be valuable to evaluate future therapeutic strategies combining targeted and immunotherapies.

Phosphoflow analysis and dissecting signaling heterogeneity in melanoma

While it's clear that changes to signaling occur in therapy-resistant cells after therapy, it is unclear if detection of signaling features can be used to identify resistant populations in melanoma. Additionally, it remains unclear what points of these signaling pathways should be targeted to enhance cell killing. To develop this approach to dissect signaling network aberrations, adherently grown melanoma cells were stimulated in suspension to quantify

basal and induced signaling responses. Key nodes of signaling in the JAK/STAT, RAF/MEK/ERK, and PI3K/AKT pathways were selected by relevance to melanoma therapeutic resistance (Shtivelman et al., 2014) (Figure 1).

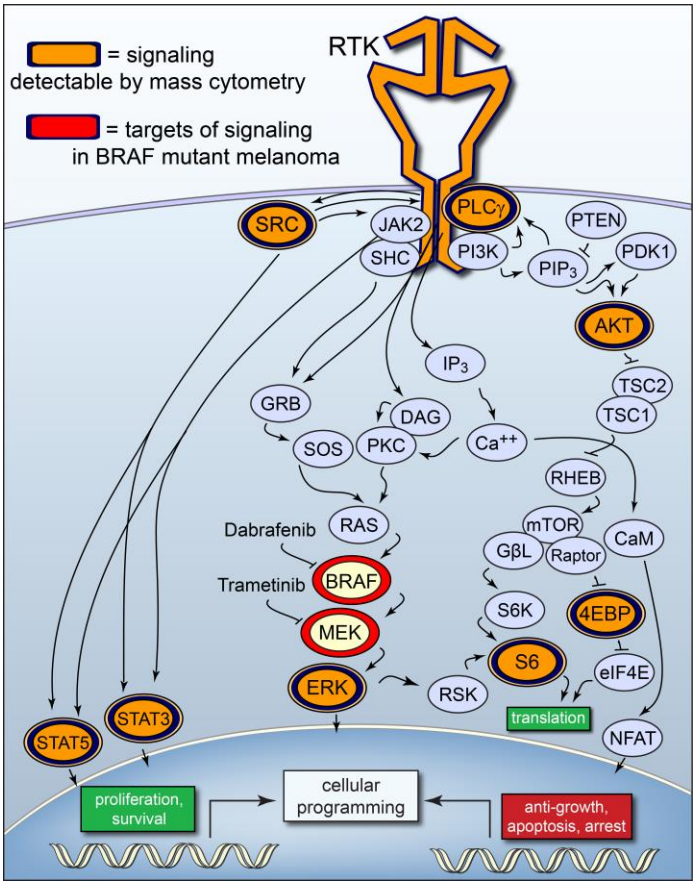

Figure 3-1 Melanoma resistance associated signaling events detected by flow cytometry. Cytometric analysis tools have been optimized to simultaneously detect several points of the melanoma cell-signaling network (highlighted orange).Targets of signaling in BRAF mutant melanoma are the current standard of care for patients with $BRAF^{V600}$ mutations (highlighted red). Key targets for analysis are signaling nodes within pathways consistent with melanoma oncogenesis and targeted therapy resistance.

To dissect melanoma signaling responses phospho-flow analysis was used to measure signaling activity after incubation with small molecules, growth factors, and cytokine stimulation for 15 minutes (Figure 2). Cytokine signaling responses by MeWo cells matched

canonical STAT protein signaling responses. IFNα and IFNγ induced a STAT1 signaling response in MeWo cells (Figure 2A). STAT1 activity regulates genes that oppose survival by transcription of genes associated with antigen presentation and suppression of proliferation (Calo et al., 2003). IFNα signaling induced phosphorylation of p-STAT3 and p-STAT5 (Figure 2A). Unlike p-STAT1 signaling, STAT3 and STAT5 signaling are known to induce genes for survival and proliferation (Calo et al., 2003). IL-4 stimulation induced phosphorylation of p-STAT6 (Figure 2A). IL-4 mediated STAT6 signaling exhibits pleiotropic effects on cancer progression by inhibiting tumor growth and increase invasiveness in some cancers (Bruns and Kaplan, 2006; Lee et al., 2017). These results demonstrate that phospho-flow analysis captures the signaling events of melanoma cells in suspension. Furthermore, these results demonstrate that the melanoma-signaling network can be reliably perturbed to activate known signaling responses from cytokines.

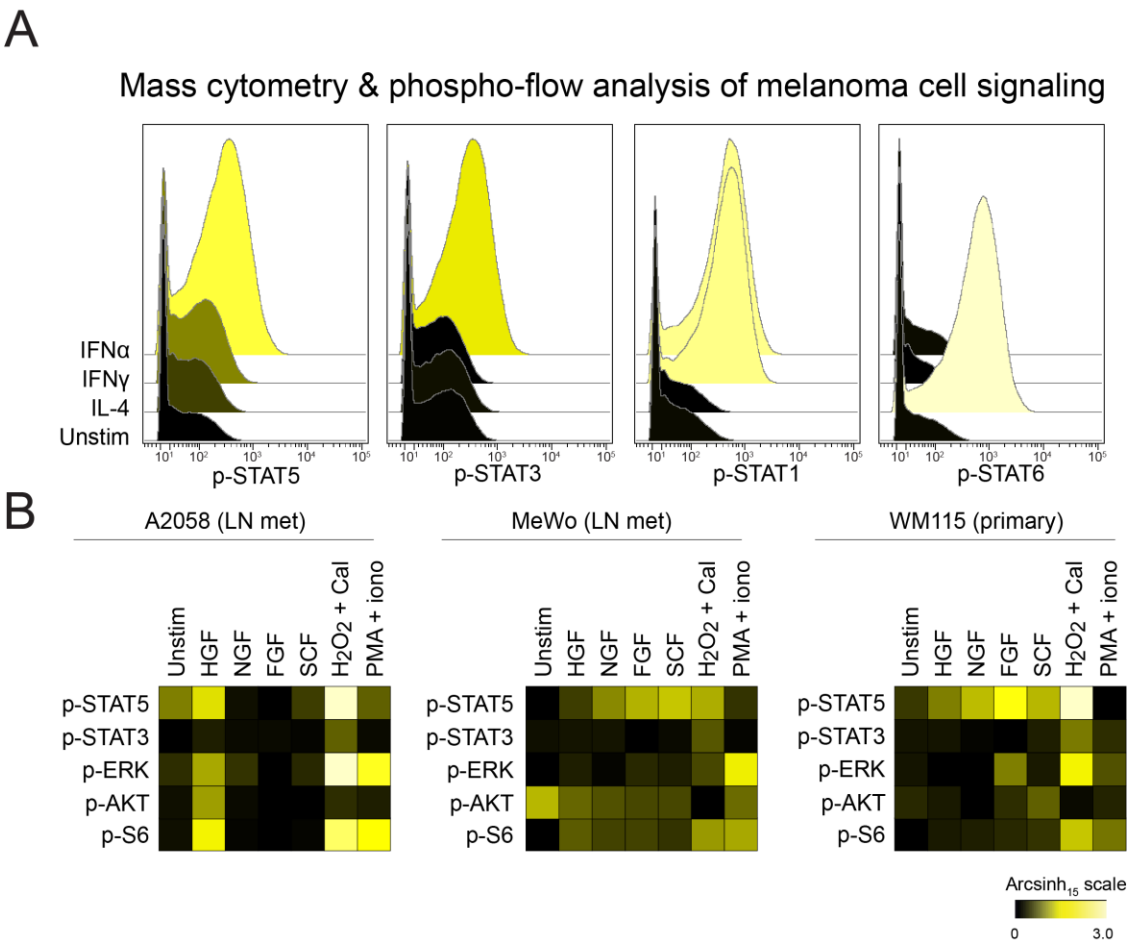

Figure 3-2 Mass cytometry (CyTOF) and phospho-flow analysis of the melanoma-signaling network. Cytokine stimulation canonically activates JAK/STAT signaling events in normal and malignant cells. (A) MeWo melanoma cells are shown responding to four cytokine factors. The color of the histogram represents the arcsinh transformed median intensity relative to the column minimum value. (B) Signaling network analysis of two additional cell lines in a separate experiment show diverging signaling network responses to six stimuli. The color of heat map represents the arcsinh transformed median intensity relative to the row minimum value.

Growth factor stimulation of receptor tyrosine kinases can activate an array of signaling components not specific to one pathway. Furthermore, receptor-signaling events have been shown to mediate resistance to BRAF and MEK targeted therapies in melanoma(Johnson et al., 2014). Phospho-flow analysis revealed A2058, MeWo, and

WM115 cells exhibited diverging signaling responses to growth factors and small molecules inhibitors. MeWo and WM115 cells were sensitive to growth factors and activated of p-STAT5, p-ERK, and p-S6 (Figure 2B). In contrast, A2058 cells showed the least diverse growth factor signaling profile but signaled strongest after HGF stimulation (Figure 2B).

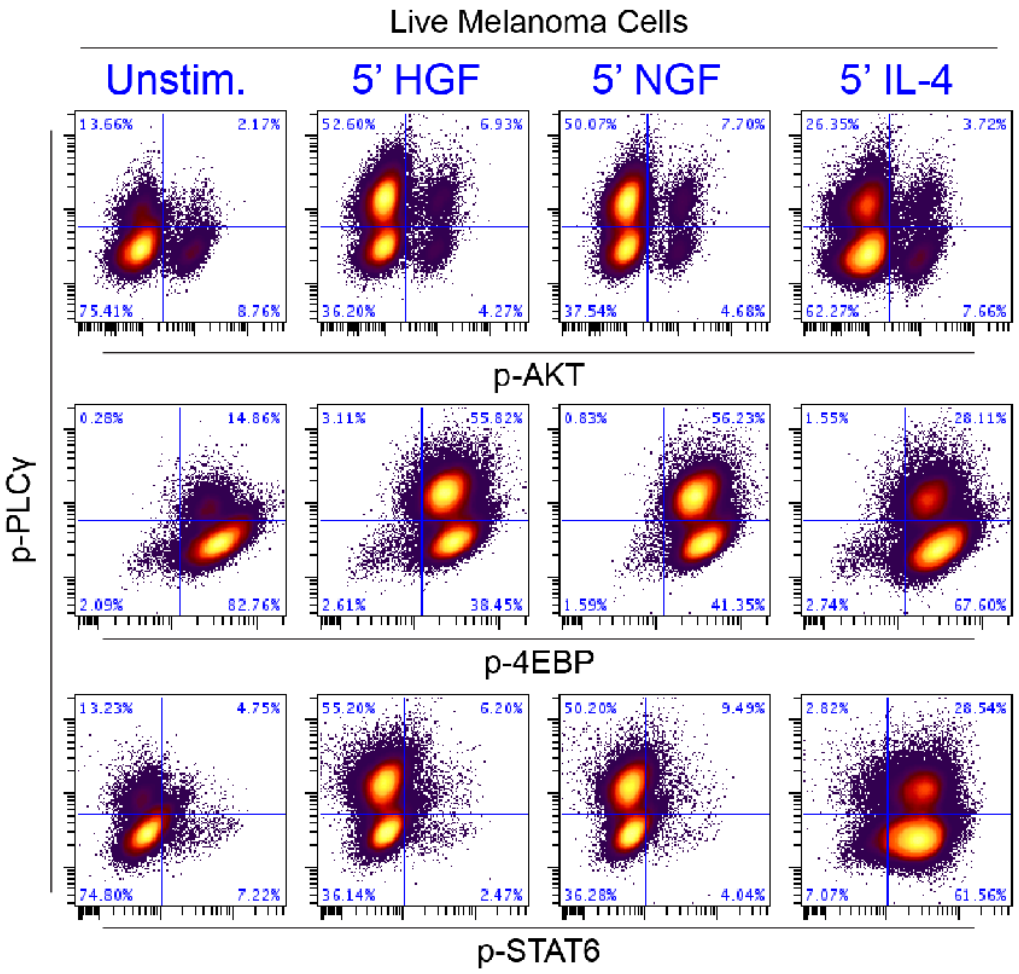

Figure 3-3 Phospho-flow analysis of MeWo melanoma cells reveal subsets distinguished by diverging signaling responses. Subsets of melanoma cells were dissociated into single cell suspension and stimulated with hepatocyte growth factor (HGF), nerve growth factor (NGF), and interleukin 4 (IL-4). Subsets responded to HGF, NGF, and IL-4 by phosphorylating AKT, PLCγ, or STAT6. Two small subsets of high basal p-PLCγ and p-AKT are detectable in the unstimulated condition. Stimulation after 5 minutes revealed cell subsets further distinguished by high and low potentiation of p-PLCγ signaling.

Signaling networks can also be dissected using small molecules that serve as positive controls for intracellular signaling pathways (Chapter 2). Peroxide and calyculin are known to inhibit tyrosine and serine/threonine phosphatases, and can temporarily increase the activity of several signaling pathways (Denu and Tanner, 1998; Swingle et al., 2007). PMA and ionomycin stimulate PKC and calcium ionophore to activate MAPK signaling (Crawford et al., 2014). Peroxide and calyculin A incubation revealed potent activation of p-STAT5, p-STAT3, p-ERK, and p-S6 in all melanoma cells (Figure 2B). PMA and ionomycin activated p-ERK and p-S6 in all melanoma cells (Figure 2B).

The phospho-flow analysis also revealed heterogeneous signaling events in MeWo cells. After HGF, NGF, and IL-4 stimulation, a subset of MeWo cells induced higher p-PLCγ signaling (Figure 3). These results show that signaling features can identify subset phenotypes, and stimulation reveals differences in signaling network regulation of melanoma cells. With this methodology, it could be possible to identify potential mechanisms of therapy resistance that mediate differential outcomes to therapy (Chapter 2).

Loss of MHC II phenotype associated with dysfunctional STAT signaling and poor immunotherapy prognosis

The landscape of treatment for melanoma has shifted towards monoclonal antibody immunotherapies that relieve suppression of antitumor responses (Mahoney et al., 2015). However, durable responses are observed in only 30-40% of advanced melanoma patients (Hamid et al., 2013; Robert et al., 2015b). From those findings, accurate predictive biomarkers are necessary to optimize patient selection and treatment strategies. Cancer

cells have been shown to evade the immune system with an expression of checkpoint inhibitors (PD-L1 and PD-L2) and recruitment of regulatory immune cells (Jiang et al., 2013; Spranger et al., 2013). Cancer cells can also downregulate the expression of major histocompatibility proteins (MHC) that present antigen to the immune system (Garcia-Lora et al., 2003). Loss of MHC proteins is associated with increased metastasis, impaired immune cell engagement, and is a prognostic biomarker in other cancers (Oldford et al., 2006; Warabi et al., 2000). While tumor-specific antigens have been well studied in melanoma, the functional significance of MHC II expression by cancer cells remains unclear. Furthermore, the influence of major histocompatibility proteins on immunotherapy prognosis has not been elucidated before in melanoma. On this basis, Johnson et al. hypothesized MHC I and MHC II proteins are required for anti-PD-1 activity and are clinically relevant biomarkers for therapy response.

To determine if MHC II is associated with anti-PD-1/PD-L1 clinical response, Johnson et al. obtained archival pre-treatment or resection specimens from 30 patients treated with anti-PD-1 (nivolumab or pembrolizumab) or anti-PD-L1 (MPDL3280A). To separate patients into two groups, MHC II^+ tumors were labeled as tumors with >5% melanoma cells ($SOX10^+$) with MHC II expression. Johnson et al. found that clinical response of patients with MHC II non-expressing tumors was significantly less than patients with MHC II-expressing tumors in a discovery cohort (P=0.033 Fisher's exact t-test). Similarly, clinical response was significantly less in patients MHC II non-expressing tumors in the validation cohort (P=0.025 Fisher's exact t-test). Furthermore, responding patients typically had tumors with higher percentages of MHC II-expressing cells (Figure 4A and, 4B). Progression-free

(PFS) and overall survival (OS) was also compared between MHC II-expressing and non-expressing patient's tumors. Median PFS was significantly longer for MHC II^+ patients (median not reached vs 3.2 months P=0.02 Figure 4C). Overall survival was also significantly longer for MHC II^+ patients (median not reached vs 27.5 months P=0.03 Figure 4C).

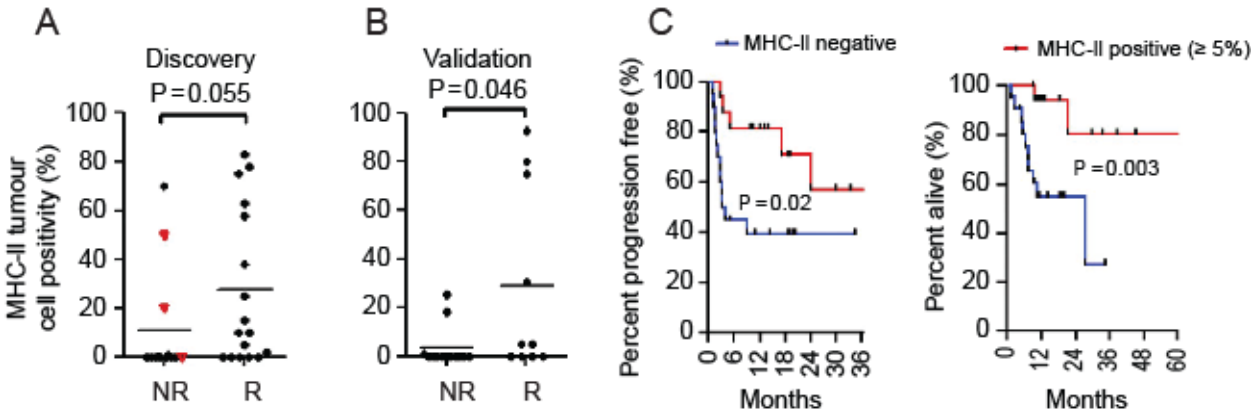

Figure 3-4 Melanoma patients with MHC II-expressing tumors have better response rates to anti-PD1/PD-L1 immunotherapy. (A) Immunohistochemical analysis of percent MHC II positive cells in a discovery set (N=30) and validation set (N=23). Responders include patients that displayed partial or complete RECIST criteria defined responses. Non-responders include patients with mixed responses (N=3, red triangles) or progressive disease patients. Wilcoxon signed rank tests were performed with a significance threshold of p=0.05. (C) Progression-free survival and overall survival in anti-PD-1/anti-PD-L1 treated patients stratified by MHC II positivity (positive tumors >5% MHC II tumor cells per section). Data from validation and discovery cohorts included in the statistical analysis. Log ranked tests were performed with a significance threshold of p=0.05.

To investigate cellular mechanisms associated with poor prognosis MHC II negative phenotypes, Johnson et al obtained and studied 60 melanoma cell lines from the Cancer

Cell Line Encyclopedia (CCLE). Analysis of mRNA expression data showed MHC I expression was high and expressed in most cell lines, however, MHC II expression was present in approximately 50% of cell lines. Because, canonical interferon gamma and STAT1 signaling have been shown to induce MHC I and II expression, the JAK/STAT signaling pathway was hypothesized to be dysregulated. My role in this work was to use phospho-flow analysis to dissect interferon gamma (IFN γ) and STAT signaling responses from melanoma cell lines. Phospho-flow analysis demonstrated that IFN γ was robustly induced after 15 min in all cell lines, however, MHC II negative cell lines unexpectantly phosphorylated STAT5 protein (Figure 5). This result demonstrates that IFN γ signaling responses are rewired in MHC II-negative cells. Furthermore, similar rewired signaling events have been observed in patients with acute myeloid leukemia resistant to IFN γ (Irish et al., 2004b). From these results activation of STAT5 signaling could be opposing STAT1 apoptotic and cell cycle arrest transcription events. These results provide a rationale for the investigation of STAT5 inhibition in melanoma patients lacking MHC II subsets to improve the outcome of patients with antibody-based immunotherapy. Thus, investigating extracellular phenotypes and signaling profiles represent a valuable approach to investigate cellular mechanisms associated with therapeutic outcomes.

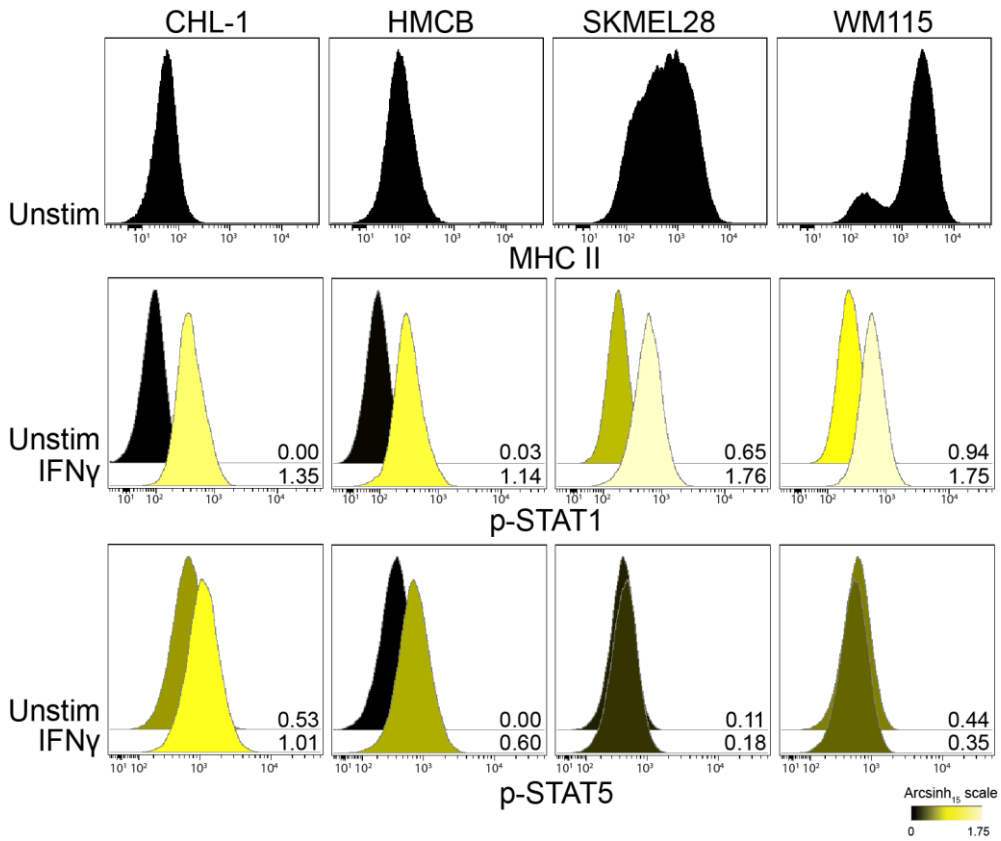

Figure 3-5 Melanoma cell MHC II class expression associated with divergent p-STAT signaling responses. Black histograms in the top row display the median MHC II expression of 4 melanoma cell lines. Phosphorylation of STAT1 and STAT5 was measured after 15 minutes of IFNγ (interferon gamma) stimulation. The color of histograms for p-STAT1 and p-STAT5 represents the arcsinh transformed median fluorescence intensity relative to the table minimum value. All cells lines displayed p-STAT1 signaling responses after IFNγ, however only MHC II low cells induced p-STAT5 signaling after IFNγ.

Materials and Methods

Cell Culture and Cell Lines. MeWo, A2058, WM115, SKMEL28, CHL-1, and HMCB melanoma cells were grown in MEM (Mediatech, Inc., Manassas, VA), supplemented with 10% fetal bovine serum (Gibco standard FBS, Life Technologies, Grand Island, NY), 1% penicillin (Gibco) and 1% streptomycin (Gibco). MeWo, A2058, WM115, and SKMEL28 cells were acquired as gifts from the lab of Vito Quaranta M.D. CHL-1 and HMCB cells were acquired as gifts from the laboratory of William Pao.

Patients. Patient samples were obtained based on the availability of tissue and were not subjected to pre-specified power analysis. All samples were acquired with patient written consent on IRB approved protocols (#030220 and #100178). Treated samples were obtained within 2 years of anti-PD-1 or anti-PD-L1 immunotherapies (nivolumab, pembrolizumab, and MPDL3280a). Responses were evaluated with RECIST criteria or in a single case defined as a stable disease with clinical benefit >3 years. For more details of patient features and clinical characteristics see Johnson et al. (Johnson et al., 2016).

Phospho-flow Cytometry. Melanoma cell lines were treated with Accutase (EMD Millipore, #SCR005) for 10 min at 37 °C to dissociate them from the plate. Dissociated cell lines rested at 37 °C in a CO2 incubator for 30min before stimulation. For the calyculin A treatment group, cells were incubated at 0.1 µM during the 30 min incubation period (Cell Signaling Technology, Danvers, MA). After resting, cells were stimulated by adding cytokines or growth factors (Cell Signaling Technology) at a final concentration of 100 ng/ml. Peroxide treated cells were stimulated at a final concentration of 3.3 mM. During signaling, cells were kept in a 37 °C CO2 incubator. After 15 min of signaling, cells were fixed for 10 min at room temperature with a final concentration of 1.6% paraformaldehyde (Electron Microscopy Services). Cells were then pelleted, and permeabilized by resuspension in 2ml of methanol and stored overnight at 20 °C. Flow cytometry staining was performed after methanol using the following antibodies: HLA-DR (BD Biosciences, clone G46-6), p-STAT5 (BD Biosciences, clone 47), p-STAT1 (BD Biosciences, clone 4A), p-STAT3 (BD Biosciences, clone 4/P-STAT3), p-STAT6 (BD Biosciences, clone 18), p-ERK (BD Biosciences, clone 20A), p-AKT (Cell Signaling, clone 193H12), p-S6 (Cell Signaling,

clone D57.2.2E), p-PLCγ (BD Biosciences, clone K86-689.37), and p-4EBP1 (BD Biosciences, clone 236B4). Samples were analyzed on an LSRII system (BD Biosciences).

Mass Cytometry. MeWo cells in Figure 2A were prepared and stained with the same techniques as phospho-flow fluorescence cytometry. Phospho-specific antibodies were also the same as fluorescence cytometry, however, metal-labeled conjugates were acquired from Fluidigm.

Immunohistochemistry and HLA-DR Scoring. HLA-DR (clone sc-53319) and SOX10 (clone LS-C312170) antibody clones were acquired Santa Cruz Biotechnology and LsBio respectively. For details of staining, conditions see Johnson et al. Two pathologists scored percentage of HLA-DR positive melanoma cells that expressed SOX10. Pathologist made visual estimations from whole tumor sections in cancer cell dense regions. For more details of HLA-DR scoring see Johnson et al.

Data Analysis. Cytobank was used to store .fcs files and perform data analysis including histogram overlays, biaxial plots, and heat maps.

Statistical Analysis. Statistical test for MHC II tumor percent positivity was performed using nonparametric Wilcoxon's rank sum test. For PFS analysis, the survival curves were estimated using the Kaplan–Meier method with the log-rank test to examine the statistically significant differences between study groups. Statistical analyses were performed using R or GraphPad Prism. All P values reported were two-sided. For more details of statistical methods see Johnson et al.

CHAPTER IV

SINGLE CELL ANALYSIS OF HUMAN TISSUES AND SOLID TUMORS WITH MASS CYTOMETRY

Authors: **Leelatian N.* and Doxie DB*.**, Greenplate AR, Mobley BC, Lehman JM, Sinnaeve J, Kauffmann RM, Werkhaven JA, Mistry AM, Weave KD, Thompson RC, Massion PP, Hooks MA, Kelley MC, Chambless LB, Ihrie RA, Irish JM

*Denotes equal contribution as co-authors

This work is presented as it appears in manuscript form in *Cytometry B Clin Cytom* 2017

Preface

High dimensional analysis approaches such as mass cytometry analysis have been well documented in blood cancers, however, standardized approaches to analyze and release adherent cells into suspension have not been developed for mass cytometry analysis. This work features the systematic comparison of dissociation techniques and reagents. The systematic comparison of dissociation techniques identified workflows most suitable to yield viable cells and maintain tissue heterogeneity in suspension. Results from this work enabled the development of a workflow applied to tumors in a clinical study of human melanoma in Chapter 5.

.

Abstract

Background: Mass cytometry measures 36 or more markers per cell and is an appealing platform for comprehensive phenotyping of cells in human tissue and tumor biopsies. While tissue disaggregation and fluorescence cytometry protocols were pioneered decades ago, it is not known whether established protocols will be effective for mass cytometry and maintain cancer and stromal cell diversity.

Methods: Tissue preparation techniques were systematically compared for gliomas and melanomas, patient derived xenografts of small cell lung cancer, and tonsil tissue as a control. Enzymes assessed included DNase, HyQTase, TrypLE, collagenase (Col) II, Col IV, Col V, and Col XI. Fluorescence and mass cytometry were used to track cell subset abundance following different enzyme combinations and treatment times.

Results: Mechanical disaggregation paired with enzymatic dissociation by Col II, Col IV, Col V, or Col XI plus DNase for 1 hour produced the highest yield of viable cells per gram of tissue. Longer dissociation times led to increasing cell death and disproportionate loss of cell subsets. Key markers for establishing cell identity included CD45, CD3, CD4, CD8, CD19, CD64, HLA-DR, CD11c, CD56, CD44, GFAP, S100B, SOX2, nestin, vimentin, cytokeratin, and CD31. Mass and fluorescence cytometry identified comparable frequencies of cancer cell subsets, leukocytes, and endothelial cells in glioma ($R = 0.97$), and tonsil ($R = 0.98$).

Conclusions: This investigation establishes standard procedures for preparing viable single cell suspensions that preserve the cellular diversity of human tissue microenvironments.

Introduction

In preparing single cell suspensions of healthy and malignant tissue, a common goal is to preserve viability while maintaining cellular diversity and preserving rare subsets. Multidimensional cytometry is well suited to this challenge because it can simultaneously characterize known cell types and reveal novel cell subsets (Irish, 2014; Irish and Doxie, 2014). Mass cytometry uses antibodies to quantify features of individual cells in primary tissues (Bandura et al., 2009; Leelatian et al., 2015) and has been applied to characterize cell subsets in human bone marrow, blood, and germinal center tissues as well as diverse murine tissues (Amir el et al., 2013; Bendall et al., 2011; Levine et al., 2015). However, mass cytometry remains relatively untested in the context of solid tumors. Fluorescence flow cytometry and fluorescence activated cell sorting (FACS) have been used to prospectively isolate functionally distinct cell subsets and suggest that mass cytometry analysis could help to further characterize solid tumors (Irish and Doxie, 2014). A key goal of this study was to evaluate the suitability of different cell preparation techniques for mass cytometry and to develop standard procedures and quality controls that do not require measuring light scatter. An additional goal was to use the multidimensionality of mass cytometry to characterize preservation of cellular diversity under different solid tumor cell preparation techniques.

In this study, mechanical and enzymatic dissociation protocols were systematically tested on multiple types of fresh human solid tumors and tissues to develop an efficient, reliable method for dissociation and single-cell analysis by mass cytometry. Human tonsils and lymphoma tumors reliably dissociate with mechanical force alone and we have previously

established protocols for their study by fluorescence cytometry (Irish et al., 2006b; Irish et al., 2010b) and mass cytometry (Polikowsky et al., 2015). Preparation techniques for tissue samples derived from intraoperative resections of gliomas (grades II-IV), melanomas, and patient derived xenografts (PDX) of small cell lung cancer (SCLC) were compared. As a control, the same techniques were applied to human tonsillar tissue. The abundance of different cell types, such as leukocytes, endothelial cells, epithelial cells, fibroblasts, and cancer cell subsets, was tested under these conditions. Established protein markers for expected cell types in tissues tested in this study were used in fluorescence cytometry (Table S1) and mass cytometry (Table S2, Table S4). The common markers were selected so that both rare and abundant cell types could be compared between mass and fluorescence cytometry. The additional markers in the mass cytometry panel provided a more comprehensive analysis of cell diversity.

Six enzymes for cell separation were selected to compare in solid tumor preparation protocols for mass cytometry analysis: HyQTase, TrypLE, collagenase (Col) II, Col IV, Col V, and Col XI. Enzyme choice was based in part on prior use in several solid tumor types and preparation of single cell suspensions containing cancer cell and immune subsets for FACS (Al-Hajj et al., 2003; Boiko et al., 2010; Chan et al., 2009; Donnenberg et al., 2013; Richards et al., 2012; Zimmerlin et al., 2011). DNase was also tested to determine its ability to enhance live cell yield from dissociation. Dissociation kinetics for enzyme combinations in distinct tissue types were also characterized. Finally, specific enzymes and dissociation duration times were selected based on optimal viable cell yield and representation of expected cell populations.

Tissue Sample Collection – All samples were obtained with patient consent, with Vanderbilt institutional review board (IRB) approval, in accordance with the Declaration of Helsinki, and were de-identified. Gliomas were intraoperative specimens from WHO grade II, III, or IV tumors (IRB #131870), collected in sterile normal saline. Melanomas were cutaneous and lymph node resections (IRB #030220), collected in MEM (Corning/Mediatech, Corning, NY) with 10% FBS + 1X Pen/Strep (GE Healthcare, Pittsburgh, PA). Small-cell lung cancer (SCLC) patient derived xenograft (PDX) samples were obtained as a gift from the Rudin laboratory (LX-22, (Daniel et al., 2009)) and propagated solely as patient-derived xenografts in female athymic nude mice (HSD:Athymic Nude-Foxn1$^{nu/nu}$) obtained from Envigo with Vanderbilt institutional animal care and use committee (IACUC) approval. SCLC PDX were collected in RPMI 1640 (Corning/Mediatech, Corning, NY) plus 10% FBS+ 1X Pen/Strep. Glioma, melanoma, and SCLC PDX samples were transported at room temperature without delay to the laboratory and processing began within 30 minutes of collection from patients. Human tonsillar tissue was obtained from routine tonsillectomies (IRB #121328), collected in RPMI 1640 (Corning/Mediatech, Corning, NY) plus 10% FBS+ 1X Pen/Strep, transported on ice, and processed within 4 hours of collection.

Mechanical and Enzymatic Dissociation – Sequential dissociation steps are described in detail in the main text. “Coarse mincing” indicates no additional mechanical dissociation of tissues (i.e. tissues were left as obtained intraoperatively). “Fine mincing” indicates additional mechanical dissociation using scalpels. Conventional mechanical dissociation of tonsils included fine mincing and immediate filtration of tissue through a

70 µm cell strainer without additional enzymatic dissociation, as previously established (Irish et al., 2006b; Irish et al., 2010b; Polikowsky et al., 2015). Dissociation enzymes were obtained from Sigma Aldrich (Darmstadt, Germany) (collagenase II, IV, V, and XI), ThermoFisher (Waltham, MA) (TrypLE-Express), and GE Healthcare (PA) (HyQTase). Collagenases were used at 1 mg/mL. HyQTase and TrypLE-Express were used at 1X according to the manufacturer's recommendations. DNase I (Sigma Aldrich) was used at a final concentration of 0.25 mg/mL. For conditions involving collagenases and no enzyme, cells were resuspended in recommended media for specific tissue types prior to adding indicated enzymes (gliomas, DMEM/F12+Glutamax, (Gibco/Life Technologies, MA) with a defined hormone and salt mix (Reynolds et al., 1992) and 50 µg/mL gentamicin; melanomas, MEM with 10% FBS + 1X Pen/Strep; Tonsils and SCLC PDXs, RPMI 1640 + 10% FBS + 1X Pen/Strep. For dissociation conditions with HyQTase or TrypLE, tissues were dissociated in working concentrations of enzymes (with or without DNase), without addition of cell culture media, according to the manufacturer's recommendations. Enzymatic dissociations were performed in a 37°C incubator with 5% CO_2, with constant rocking on a nutating platform mixer at 18 rpm. Cells were then strained with 70 µm and 40 µm cell strainers prior to further analysis.

Quantification of cell viability – Cell suspensions obtained from different dissociation protocols were resuspended in corresponding cell culture media at volumes proportional to initial tissue weight (1 mL per 100 mg of tissue). Viable cells were quantified using Trypan Blue staining, normalized to the initial tissue weight, and reported as millions of live cells per gram of tissue.

Statistical testing – Enzyme conditions were compared as groups (horizontal lines) using a Student's t-test. The relationship between cell subset abundance measured by fluorescence or mass cytometry was compared using Pearson's correlation R and Spearman's rank correlation ρ (rho).

Cell line and cell culture – Jurkat cells were obtained from Utpal Dave at Vanderbilt, and were grown in RPMI 1640 + 10% FBS + 1X Pen/Strep as recommended. MeWo cells were obtained from Kimberly Dahlman and Jeffery Sosman with permission of Antoni Ribas (UCLA) and were grown in MEM + 10% FBS + 1X Pen/Strep, as recommended.

Flow cytometry - Cell suspensions were evenly divided for parallel phenotyping with fluorescence and mass cytometry according to the protocols below. Conditions were identical between mass and fluorescence cytometry with the exception of an additional staining step including saponin for mass cytometry analyses of glioma and melanoma that include SOX2. This type of saponin step has been established to have no significant impact on subsequent mass cytometry staining (Behbehani et al., 2014).

Fluorescence flow cytometry – For fluorescence cytometry, live surface staining was performed for surface marker detection (Supplemental Table S1). After washing with PBS and pelleting twice (at 200 x *g* for 5 min each time), cells were fixed with 1.6% paraformaldehyde (Electron Microscopy Services, Fort Washington, PA) for 10 min at room temperature, washed with PBS (HyClone Laboratories, Logan, UT), pelleted at 800 × *g,* and permeabilized with 100% ice-cold methanol (Fisher Scientific, Waltham, MA) at −20°C overnight following established protocols (Irish et al., 2010b; Krutzik and Nolan, 2003). Cells were washed twice with cell staining media composed of PBS plus 1% BSA

(Fisher Scientific, Waltham, MA) and pelleted at 800 *x g*. For each comparison, cells were stained in 100 µL staining media for 30 minutes at room temperature. All antibodies are listed in Supplemental Tables. Note that some antibodies that detect cell surface antigens (CD45-BV786, CD44-PE, and CD31-PE-Cy7) were used after fixation and methanol permeabilization due to concerns for stabilization of fluorochromes after methanol exposure. After staining, cells were washed twice with PBS, pelleted at 800 *x g*, and resuspended in PBS for analysis on a 5-laser LSRII (BD Biosciences, San Jose, CA) at the Vanderbilt Flow Cytometry Shared Resource.

Mass cytometry – Solid tissue cells obtained from the same dissociation conditions as those analyzed by fluorescence flow cytometry were stained live for cell surface markers, fixed, permeabilized, and washed as for fluorescence flow cytometry above and in concordance with established mass cytometry protocols (Leelatian et al., 2015). Permeabilization with 0.02% Saponin (Millipore, Darmstadt, Germany) in PBS was also included before methanol permeabilization of gliomas and melanomas as part of an optimized multi-step protocol that included detecting SOX2, which was not included in the fluorescence panel. Metal-tagged antibodies were used to stain cells in 100 µL cell staining media for 30 minutes at room temperature (Supplemental Table S4). After staining, cells were washed once with PBS, once with deionized water, pelleted at 800 *x g*, and resuspended in deionized water containing normalization beads (Fluidigm). Standard bead-based normalization was used as previously described (Finck et al., 2013). Cells were collected on a CyTOF 1.0 at the Vanderbilt Flow Cytometry Shared Resource. Original data were normalized with MATLAB normalization software prior to further analysis using

Cytobank (Kotecha et al., 2010) and established mass cytometry analysis methods (Diggins et al., 2015). viSNE analysis was performed using 60,000 cCasp3^{-}HH3^{+} cells per sample. For glioma G-LC-15, the following markers were used for viSNE analysis: CD31, CD64, CD45RO, S100B, CD45, PDGFRα, SOX2, CD24, CD44, CD3, GFAP, αSMA, HLA-DR, and CD56. For tonsil T02-23, the following markers were used for viSNE analysis: CD4, IgD, CD16, CD45RO, CD45RA, CD45, CD27, CD86, CD33, CD11c, CD14, CD19, CD38, CD8, CD3, IgM, HLA-DR, and CD56. Samples of the same tissue type dissociated with different types of collagenase were analyzed simultaneously by viSNE.

Histone H3 testing – Healthy peripheral blood mononuclear cells (PBMCs) were used as controls in testing histone H3 as a nucleated cell marker for multiple flow cytometry platforms. PBMCs were stained live for detection of cell surface markers (Supplemental Table S2). After being washed twice with PBS, cells were then fixed with 1.6% paraformaldehyde and permeabilized with 100% ice-cold methanol for intracellular staining. Stained PBMCs were then evenly divided and half of the cells were stained with iridium at a final concentration of 0.25 μM in PBS for 15 minutes at room temperature. Cells were then washed once with PBS, once with deionized water, pelleted at 800 *x g*, and resuspended in deionized water containing normalization beads. Cells were collected as described above.

Results

Tissue dissociation with collagenase and DNase improved live cell yield

A matrix of dissociation conditions was tested to identify optimal protocols for multiple solid tumor types and tonsil controls (Figure 1, Figure S1, and Figure S2). The mechanical dissociation protocol (*see Materials and Methods*) was first compared to fine mincing of

tonsil tissue followed by a 2-hour enzymatic dissociation with combinations of collagenase and DNase. For tonsils, a combination of fine mincing, collagenase, and DNase resulted in superior live cell yield per gram of tissue compared to conventional dissociation methods (Figure S1, $p < 0.05$). Additionally, fine mincing of tonsils did not adversely affect cell viability (Figure S2) when compared to coarse mincing (left as obtained intraoperatively).

Since freshly resected tissues and tumors frequently differ in size, fine mincing was selected as an initial mechanical dissociation step for all tissue types. To determine the optimal enzymes for disaggregation of human gliomas, seven different enzymatic conditions were tested for their ability to yield live, single cells (Figure 1A, N = 3). Intraoperative samples of gliomas were finely minced and incubated with a cocktail of DNase plus one enzyme (either HyQTase, TrypLE, Col II, Col IV, Col V, or Col XI) or DNase alone for 2 hours at 37°C, with continuous rocking. Increased live cell yield per gram of tissue was seen in conditions containing collagenase and DNase as compared to other conditions ($p < 0.01$). Additionally, DNase plus collagenase improved live cell yield for glioma compared to collagenase alone ($p < 0.01$). No significant differences were observed in live cell yield per gram of glioma tissue between conditions using different types of collagenases plus DNase. High-resolution images of trypan blue stains are shown in Figure S3.

The same matrix of conditions was tested on intraoperative samples of human melanomas (Figure 1B, N = 3). As with glioma, no significant difference in live cell yield was observed between different types of collagenases, and viable cell yields were highest in conditions containing collagenases and DNase ($p < 0.01$). In freshly resected tonsils (Figure 1C, N =

4), collagenases with DNase gave a higher live cell yield than either DNase alone ($p < 0.05$) or TrypLE plus DNase ($p < 0.01$). However, collagenases with DNase did not significantly differ from HyQTase with DNase, and addition of DNase did not result in higher or lower live cell yield, in tonsil dissociation.

Enzymatic dissociation with collagenase and DNase for 1-2 hours provided superior live cell yields

While incubation in enzyme solutions enhanced tissue disaggregation (Figure 1 and Figure S1), excessive incubation might adversely affect cell viability. A dissociation time course was performed on intraoperative glioma specimens to determine the optimal time point for highest live single cell yield (Figure 2A). Gliomas were finely minced and incubated in collagenases plus DNase for 30 minutes, 1 hour, 2 hours, 4 hours, or 6 hours (Figure 2A, N = 3). Live cell yield per gram of glioma tissue significantly decreased after 4 hours of enzymatic dissociation with Col II, Col V, or Col XI plus DNase compared to earlier time points (Col II and Col XI, $p < 0.001$; Col V, $p < 0.05$), whereas it significantly decreased after 6 hours of dissociation with Col IV plus DNase (Figure 2A, $p < 0.001$).

Dissociation kinetics of tonsils were also characterized for time points ranging from 15 minutes to 24 hours (Figure 2C). Finely minced tonsils dissociated with Col II plus DNase for 1-2 hours gave higher live cell yield when compared to earlier time points ($p < 0.05$) as well as later time points ($p < 0.001$). Similarly, viable cell yield decreased significantly after 1-2 hours when tonsils were dissociated with either Col IV or Col XI plus DNase (IV, $p < 0.05$; IX, $p < 0.01$). Live cell yield from the combination of Col V and DNase also decreased after 6 hours ($p < 0.01$). Live cell yield from intraoperative melanoma specimens and SCLC

patient-derived xenografts (PDXs) did not significantly decrease after 6 hours of dissociation, regardless of the type of collagenase (Figure 2B and 2D).

Testing histone H3 as a nucleated cell marker compatible with mass and fluorescence cytometry

An anti-Histone H3 (HH3) monoclonal antibody was next tested as a potential marker of nucleated cells that would function equivalently in fluorescence and mass cytometry. Jurkat T leukemia cells gated as intact cells were 98.9% positive for HH3 in fluorescence cytometry (Figure S4A). Similarly, when Jurkat cells were gated first as $HH3^+$, they were observed to be >99.8% intact cells when gated using light scatter in fluorescence cytometry (Figure S4B). Peripheral blood mononuclear cells (PBMCs) were used to further test HH3 because PBMC have well-studied cell subsets that have been extensively characterized by both fluorescence and mass cytometry (Bodenmiller et al., 2012; Leelatian et al., 2015; Nicholas et al., 2015). PBMCs from a healthy donor were stained with a panel of 16 mass-tagged antibodies (Table S2). Frequencies of known cell subsets identified by biaxial gating were closely correlated in the same mass cytometry dataset gated using HH3 or established iridium-based gating (Figure S5, Pearson correlation R = 1.00, Spearman rank of subset abundance rho (ρ) = 1.00, Table S3), supporting the use of HH3 as nucleated cell marker across multiple flow cytometry platforms.

Assessment of cell subset diversity in solid tumor following collagenase and DNase treatment

Two- to seven-dimensional fluorescence flow cytometry has been used extensively to characterize presence and abundance of cell subsets in patient-derived tissues. Glioma cell

subsets consistent with those documented in prior studies were present after a 1-hour dissociation with DNase plus Col II using fluorescence flow cytometry (Figure 3A, Col II). In glioma sample G-RT-06, 55.4% of all events were identifiable as intact nucleated cells based on HH3 staining. $CD45^+$ immune cells comprised 59.7% of live intact cells, which included $CD3^+$ T cells (26.7%) as well as other immune cell types (71.8%). Presence of immune cell subsets was confirmed with immunohistochemistry (IHC) staining of formalin-fixed paraffin-embedded (FFPE) sections of the same sample (Figure S6). Additionally, $CD31^+$ endothelial cells were detected (5.1% of non-immune cells), as were cell subsets that differentially expressed CD56 (NCAM) and GFAP. The abundance of nucleated cells and other known cell subsets was similar between different collagenase types (Figure S7).

To determine if cells derived from dissociations using collagenase and DNase were suitable for mass cytometry analysis, cells obtained from intraoperative glioma resections (G-RT-06) were stained with 16 isotope-labelled antibodies (Table S4). Histone H3 was used to identify intact nucleated cells. A biaxial analysis sequence similar to that used for fluorescence flow cytometry analysis was used for comparison of subset abundance identified by these two cytometry platforms (Figure 3B). A strong correlation of cell subset abundance between the two methods was observed and quantified (Table 1; Pearson's $R = 0.97$, Spearman's rank $\rho = 0.93$). Similar comparisons were performed in tonsils (Figure 3D). Strong correlations of subset abundance between the two different cytometry platforms was also observed in tonsil (Table 1; Pearson's $R = 0.98$, Spearman's rank $\rho = 0.90$).

Subsets of immune cells in tonsils were also identified by fluorescence flow cytometry, including $CD3^+$ T cells, $CD44^+$ antigen-presenting cells (APCs), $CD44^-$ APCs, and additional immune and non-immune cell types, as expected (Figure 3C, Col II). Abundance of tonsil cell subsets was similar between dissociations using different collagenase types (Figure S8). Single cells obtained from resected melanomas (MP-04) and a melanoma cell line, MeWo, were analyzed by fluorescence flow cytometry and were observed to have intrinsic auto-fluorescence on some channels, whereas glioma and tonsil samples studied here showed no auto-fluorescence (Figure S9). Mass cytometry was next used to study melanoma tumors (Figure S10). $CD45^+$ immune subsets, including $CD45^+$HLA-DR^+ antigen-presenting cells, $CD45^+CD3^+$ T cells ($CD8^+$ and $CD8^-$, and $CD45RO^+$ memory and $CD45RO^-$ non-memory), as well as $CD31^+$ endothelial cells were identified in melanoma. Additionally, among the non-immune, non-endothelial cells, other cell subsets were identifiable by nestin, SOX2, CD44, HLA-ABC, vimentin, and cytokeratin.

To characterize the effects of different types of collagenase on the presence of cell subsets, mass cytometry analysis of cells derived from glioma dissociation at one hour with DNase plus either Col II, Col IV, Col V, or Col XI was performed (Figure 4). This time point was selected based on its highest live cell yield across multiple tissue types, shown above. viSNE analysis (Amir el et al., 2013) was used to compare cell subsets in the different dissociation conditions. Known cell subsets in gliomas were present in all conditions, including $CD45^+$ immune cells ($CD3^+$ T cells, and $CD64^+$ microglia), $CD45^-CD31^+$ endothelial cells, $GFAP^+$ glial cells, $S100B^+$ astrocyte-like cells, and $SOX2^+$ stem-like cells. Established cell subsets were also observed in tonsil specimens dissociated for one hour in

all types of collagenase (Figure S11). As expected, the majority of cells were $CD45^+$ immune cells. Additionally, known immune subsets, including $CD3^+CD4^+$ helper T cells, $CD3^+CD8^+$ cytotoxic T cells, $CD19^+IgD^+$ naïve B cells, and $CD19^+CD27^+$ memory B cells, were identified. These findings suggest that both mass cytometry and fluorescence cytometry identify key cell subsets in glioma and tonsil dissociated with collagenase plus DNase.

Longer dissociation times led to disproportionate cell death and loss of cellular diversity

To determine if the abundance of cell subsets changed over time with enzymatic dissociation, time course dissociations of glioma sample, G-LC-15 (Figure 5), and tonsil sample, T02-23 (Figure S13), with DNase plus Col II were performed. Cell subsets were identified using sequential biaxial analysis and given the indicated labels following expert review. Apoptotic cells, defined by high cCasp3 signal, were excluded from subsequent cell subset quantification (Figure 5A). Within the population of $HH3^+$ nucleated cells, marker analysis identified $CD45^+$ immune cells and $CD31^+$ endothelial cells. Known subsets of immune cells were present within the $CD45^+$ population, including microglia ($HLA\text{-}DR^+CD64^+$), memory T cells ($CD3^+CD45RO^+$), and non-memory T cells ($CD3^+CD45RO^-$) (Figure 5B). Within the $CD45^-CD31^-$ population, pericytes (αSMA^+) and ependymal cells ($CD24^+$) were seen, as well as rare $SOX2^+$ stem-like cells, $GFAP^+$ glial cells, $PDGFR\alpha^+$ cells, and $S100B^+$ astrocyte-like cells (Figure 5C). Quantification of these cell subsets was performed in samples obtained from different dissociation durations to characterize maintenance and enrichment of cell subsets over time (Figure 5D). Among immune cells, a

decrease in microglia (after 1 hour) and memory T cells (after 4 hours) was noted, whereas the proportion of non-memory T cells appeared to remain constant over the full range of times tested. $SOX2^+$ stem-like cells were most abundant after 1 hour of dissociation and decreased thereafter. Even though the proportion of $SOX2^+$ stem-like cells increased at 24 hours after dissociation, the overall decrease in viable cells after 4-6 hours of glioma dissociation (Figure 2A) suggested an overall loss in total viable stem-like cells at later time points. Additionally, the abundance of $GFAP^+$ glial-like cells (known to be present in most gliomas, Figure S12) remained constant during the initial 10 hours of dissociation and showed a decrease after 16 hours. This suggested that longer dissociation depletes key cell subsets in glioma. Most of the nucleated, non-apoptotic cells that remained after 24 hours of dissociation lacked expression of the key cell identity markers used in this study. Moreover, the abundance of $cCasp3^+$ apoptotic events also increased over time (Figure 5E).

A similar time course strategy was applied to tonsil specimen dissociation (Figure S13A). A decrease in the abundance of most immune cell subsets was observed at all time points greater than 1 hour of dissociation with Col II plus DNase (Figure S13B). This decrease affected all T cell subsets, plasma cells/blasts, germinal center B cells, class-switched memory B cells, and unswitched memory B cells. Notably, abundance of naïve B cells remained constant during the initial 6 hours of dissociation and only decreased after 10 hours. $CD27^-IgD^-$ B cells increased in abundance at time points extending to 6 hours, followed by a decrease at 10 hours. Dendritic cells were the only immune cell subsets that

continued to increase in abundance at 24 hours of dissociation. As expected, longer dissociation times likewise led to an increase in apoptotic cells (Figure S13C).

Discussion

A common protocol of collagenase II plus DNase for 1 hour was identified as effective for preparing viable and mass cytometry compatible single cell suspensions of all tested human solid tumors and healthy tissues. Multiple types and combinations of enzymes and dissociation kinetics were compared in freshly resected patient-derived tissues and patient-derived xenografts. Unexpectedly, collagenase also resulted in greater viable cell yield from tonsils when compared to the conventional dissociation method (Figure 1 and Figure S1), indicating that the protocol for preparation of tonsil and lymphoma tumors could be further refined. DNase clearly improved live cell yield from gliomas and melanomas and is strongly recommended for tissues where there may be ongoing cell death. Even though DNase was not observed to improve tonsil dissociation, DNase also did not adversely affect tonsil cell viability. Live cell yield from glioma dissociation began to decrease after 4-6 hours. However, live cell yields from melanoma and SCLC PDX were constant throughout the dissociation duration tested (6 hours) for all types of collagenase. In contrast, live cell yield from tonsils was maximal during the initial 2 hours of dissociation, except for collagenase V, which significantly decreased only after 6 hours.

Critically, dissociation of tissue using combined collagenase and DNase preserved cellular diversity, as seen by mass cytometry and standard fluorescence flow cytometry (Figure 3 and Figure 4). At one hour after dissociation, known cell subsets were present as expected

in each of the tested tissue types. These included immune cells in tonsil, infiltrating immune cells in glioma and melanoma, and tissue-specific cell subsets, such as cancer cell subsets, endothelial cells, glial cells, pericytes, and stem-like cells in gliomas. A difference in abundance of T cells observed between fluorescence and mass cytometry was determined to be due to use of different anti-CD3 antibody clones, as has been previously reported (Maecker et al., 2012; Nicholas et al., 2015). While immune cells and $GFAP^+$ cells in glioma were confirmed with IHC stains and observed to be in relatively close agreement between IHC and flow cytometry, small tissue sections and sections that do not sample all tumor regions may over- or under-represent cell subsets or overlook rare cells. The quantitative analysis of a large number of whole cells by multidimensional flow cytometry (10^5 to 10^7) provides a strong complement to the location information provided by imaging cytometry (Spitzer and Nolan, 2016).

Longer dissociation times led to increased cell death and disproportionate depletion of cell subsets in both gliomas and healthy tonsil. Additionally, the abundance of glial/astrocyte-like cells, as well as rare stem-like cells in glioma, decreased over time. Even though the proportions of some cell subsets increased at later time points (endothelial cells, pericytes, $SOX2^+$ stem-like cells in gliomas, and dendritic cells and $CD27^-IgD^-$ B cells in tonsils), the significant increase in cell death over a long period of dissociation would result in an overall decrease in total yield of those cell types. Comparison of the results from gliomas, melanomas, SCLC xenografts, and tonsil tissue indicates that different tissues may be sensitive to prolonged enzymatic digestion. Dissociation conditions should be evaluated closely and carefully matched to tissue type and study goals. However, based on the

results here, no more than 1 hour of dissociation is recommended unless the protocol is being optimized for a specific purpose. In future single-cell-level studies of other complex solid tissues, it will be critical to identify conditions that efficiently generate single-cell suspensions while preserving rare subpopulations of interest. Additionally, cell viability stains such as Cisplatin can be included in future mass cytometry experiments that aim to test cell functions like signaling, proliferation, viability, or cytokine production (Fienberg et al., 2012).

Acknowledgements

The authors thank Charlie Rudin for the LX22 PDX line, Utpal Dave for Jurkat T leukemia cells, and Kimberly Dahlman and Jeffery Sosman for MeWo cells.

Funding sources: Study and researchers were supported by NIH/NCI R00 CA143231 (J.M.I.), R25 GM062459 (D.B.D.), T32 CA009592 (D.B.D.), F31 CA199993 (A.R.G.), F31 HD007502 (J.S.), the Vanderbilt-Ingram Cancer Center (VICC, P30 CA68485), the Vanderbilt International Scholars Program (N.L.), a Vanderbilt University Discovery Grant (J.M.I. and N.L.), a VICC Provocative Question award (M.C.K. and J.M.I.), R01 NS096238 (R.A.I) and VICC Ambassadors awards (J.M.I. and R.A.I.).

Conflict-of-interest disclosure: J.M.I. is co-founder and board member and Cytobank Inc. and received research support from Incyte Corp.

Figure legends and Tables

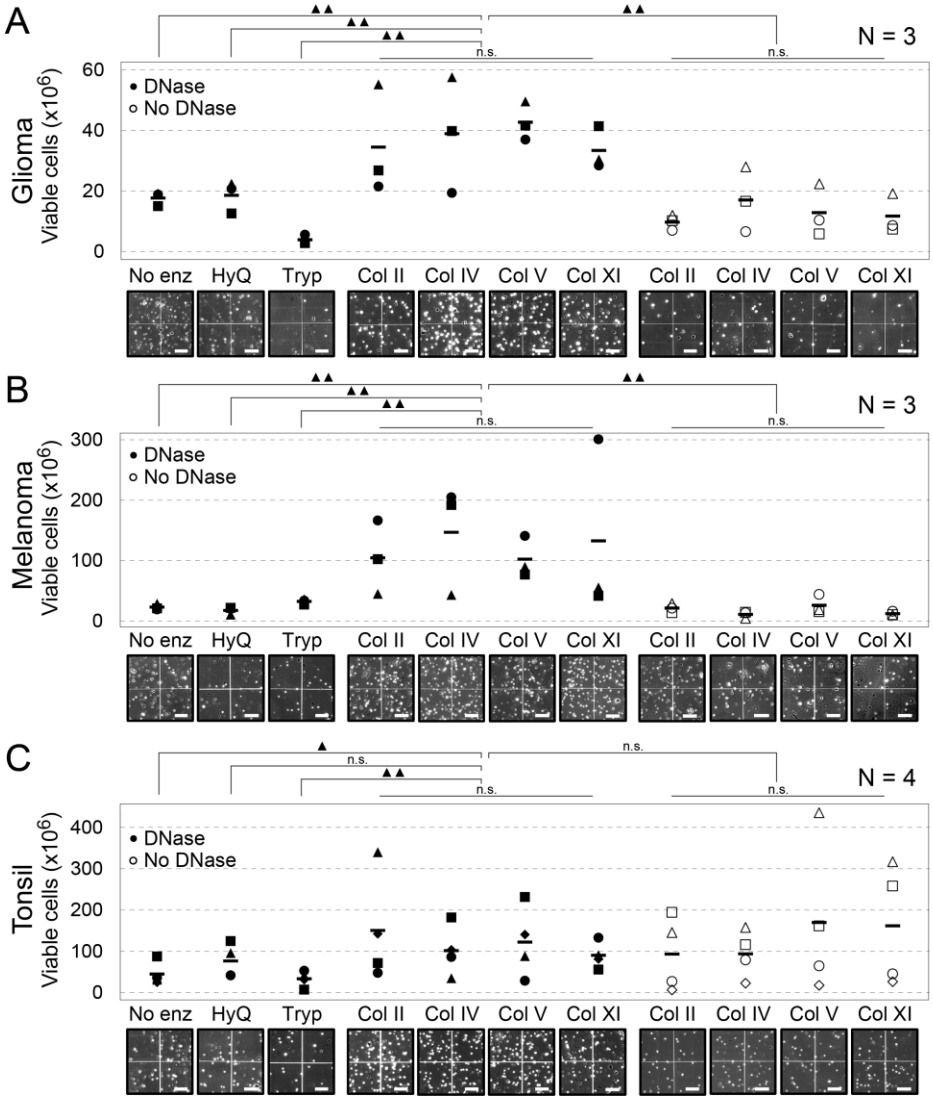

Figure 4-1 Collagenase plus DNase treatment provides better yield of live cells from three human tissues than no enzyme, TrypLE, HyQTase, or collagenase treatment alone. Graphs show millions of viable cells per gram yielded by different tissue preparation conditions following fine mincing for (A) gliomas, (B) melanomas, and (C) tonsil tissue. In addition to DNase (closed symbols), preparation enzymes tested included no additional enzyme (No enz), recombinant trypsin TrypLE (Tryp), HyQTase (HyQ), and collagenase (Col) II, IV, V, or XI. Average live cell yield is indicated for each condition by the thick horizontal line. Individual tissues or tumors are represented by different symbols. Representative trypan blue stained images are depicted under each condition. Scale bars = 100 µm. Symbols denote not significant (n.s.), p <

0.05 (♦), or p < 0.01 (♦♦). N indicates number of separate individual sample donors tested under each condition for each tissue type.

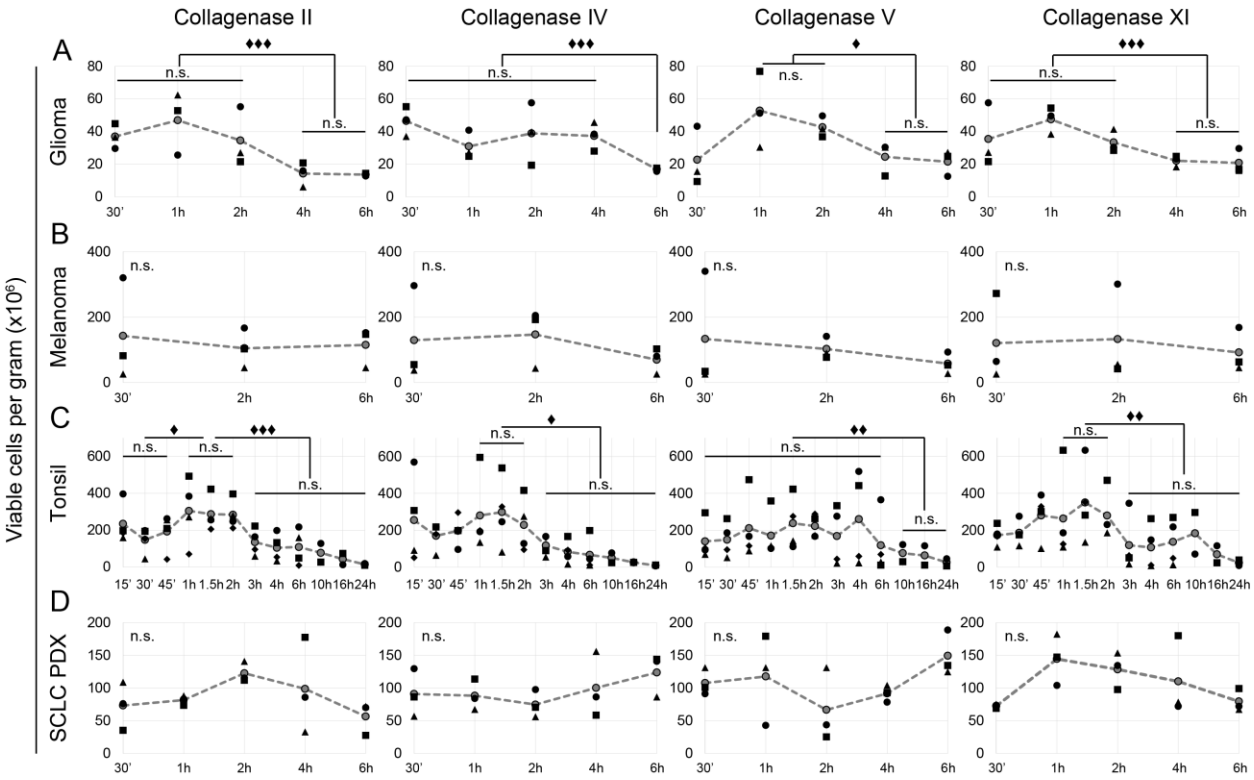

Figure 4-2 Collagenase and DNase treatment for 1 or 2 hours provided better overall live cell yield than other times. (A) Gliomas (N = 3) were finely minced and treated for varying times with DNase and either Col II, Col IV, Col V, or Col XI. Yield of live single cells (x10^6) per gram was quantified from Trypan blue images after 30 minutes (’), 1 hour (h), 2h, 4h, and 6h (filled symbols). Individual tissues or tumors are represented by different symbols. Grey circles mark average yield and are connected with dashed lines to indicate dissociation kinetics. Dissociation kinetics were similarly assessed for (B) melanomas (N = 3), (C) tonsil tissue (N = 4, except for 10h, 16h, 24h where N = 2), and (D) SCLC PDX tumors (N = 3) (D). Symbols denote not significant (n.s.), p < 0.05 (♦), p < 0.01 (♦♦), or p < 0.001 (♦♦♦).

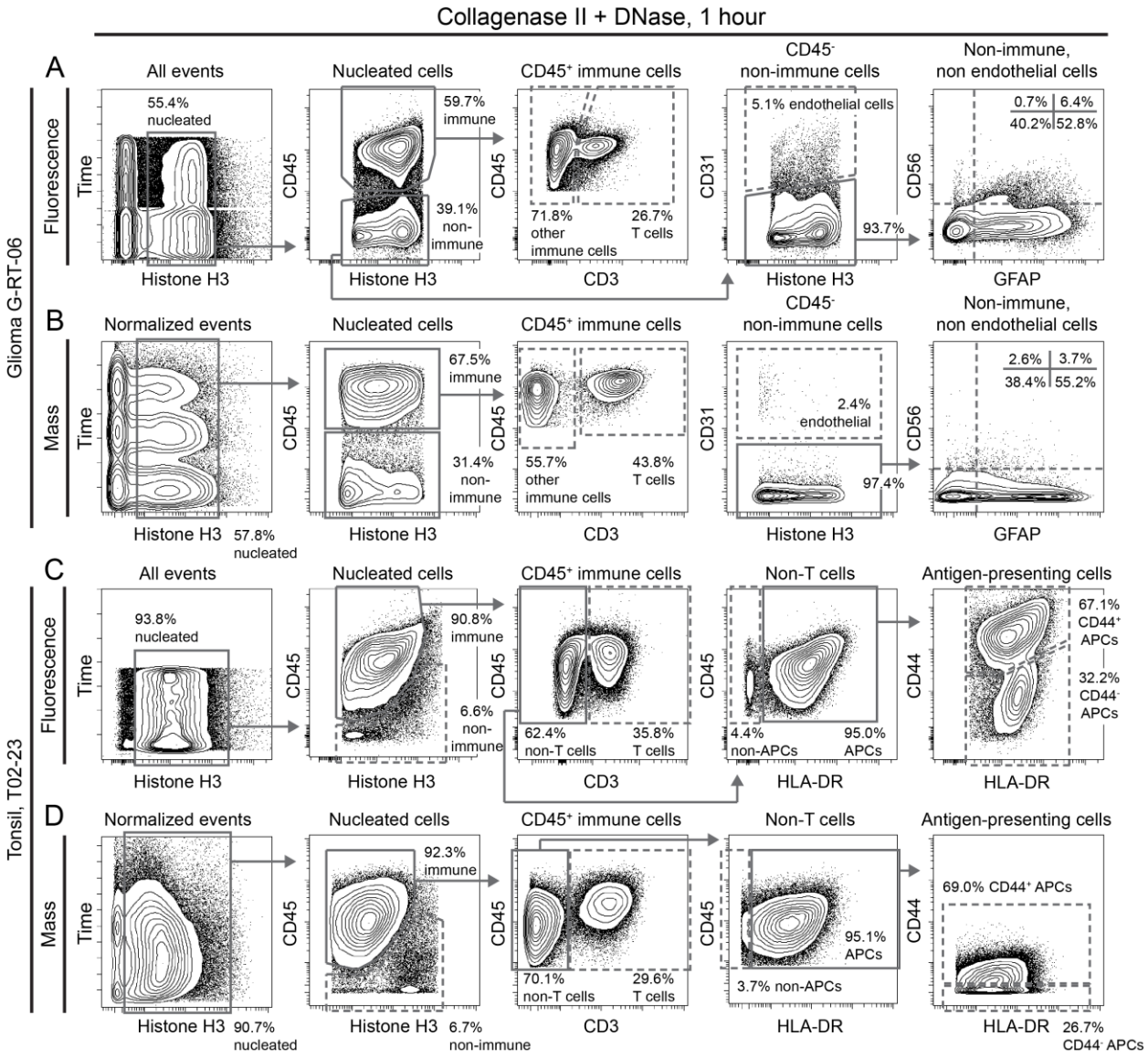

Figure 4-3 Frequency of cell types in glioma, and tonsil tissue quantified by fluorescence and mass cytometry. Biaxial plots show gating for established cell types in human tumors and tissues prepared using Col II plus DNase for 1 hour. Nucleated cells ($HH3^+$) were identified. Immune cells ($CD45^+$), T cells ($CD45^+$ $CD3^+$), APCs ($CD45^+$ $CD3^-$ $HLA\text{-}DR^+$), endothelial cells ($CD31^+$ $CD45^-$), and non-immune non-endothelial cells ($CD45^-$ $CD31^-$) were also found. (A) In fluorescence cytometry analysis of glioma from an individual patient (G-RT-06), CD56 (NCAM) and GFAP expression are shown for $CD45^-$ $CD31^-$ cells. (B) A similar gating scheme was applied to mass cytometry data from G-RT-06. In tonsil tissue from donor T02-23, CD44 and HLA-DR are shown for $CD45^+$ $CD3^-$ $HLA\text{-}DR^+$ cells, for both fluorescence (C) and mass cytometry analysis (D). Frequency of terminal populations (dashed gates) was compared between fluorescence and mass cytometry in Table 1.

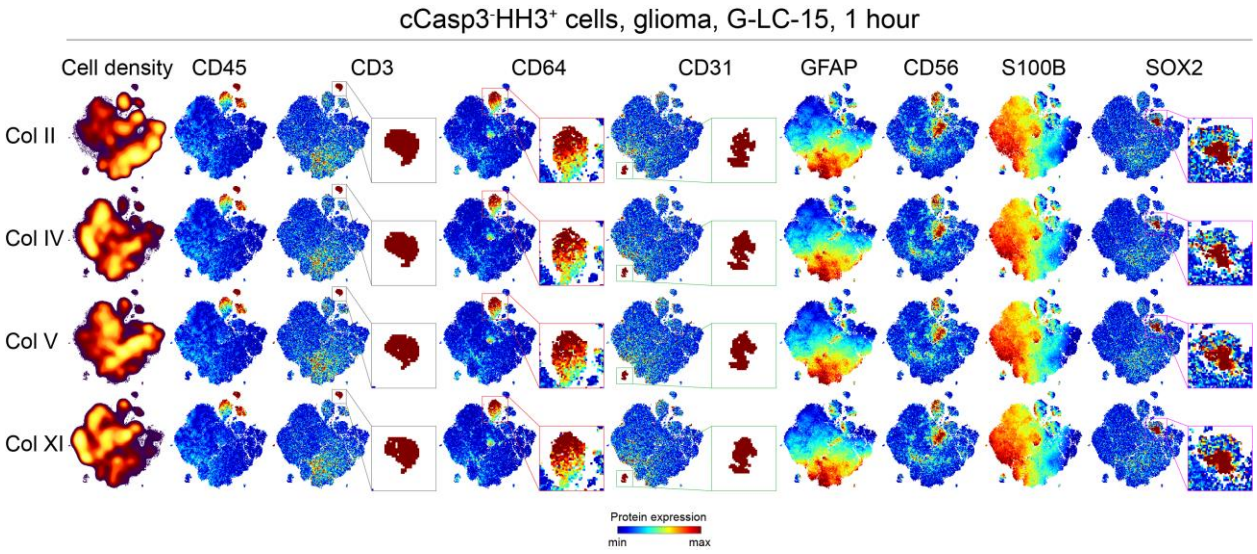

Figure 4-4 Treatment of a glioma with different collagenases yielded comparable cell subset frequencies. viSNE plots show non-apoptotic nucleated cells ($cCasp3^{-}HH3^{+}$) from glioma G-LC-15 obtained following 1-hour treatment with DNase plus either Col II, VI, V, or XI. Heat plots indicate cell density (first column) or expression of 8 proteins indicating cell type (CD45, CD3, CD64, CD31, GFAP, CD56, S100B, and SOX2). viSNE mapping was run together. Color-coded inserts next to the complete map highlight cell subsets (grey = $CD45^{+}CD3^{+}$ T cell, 0.9 ± 0.1%; red = $CD45^{+}CD64^{+}$ microglia, 3.9 ± 1.0%; green = $CD45^{-}CD31^{+}$ endothelial cells, 0.7 ± 0.2%; fuchsia = $SOX2^{+}$ stem-like cells, 1.2 ± 0.5%).

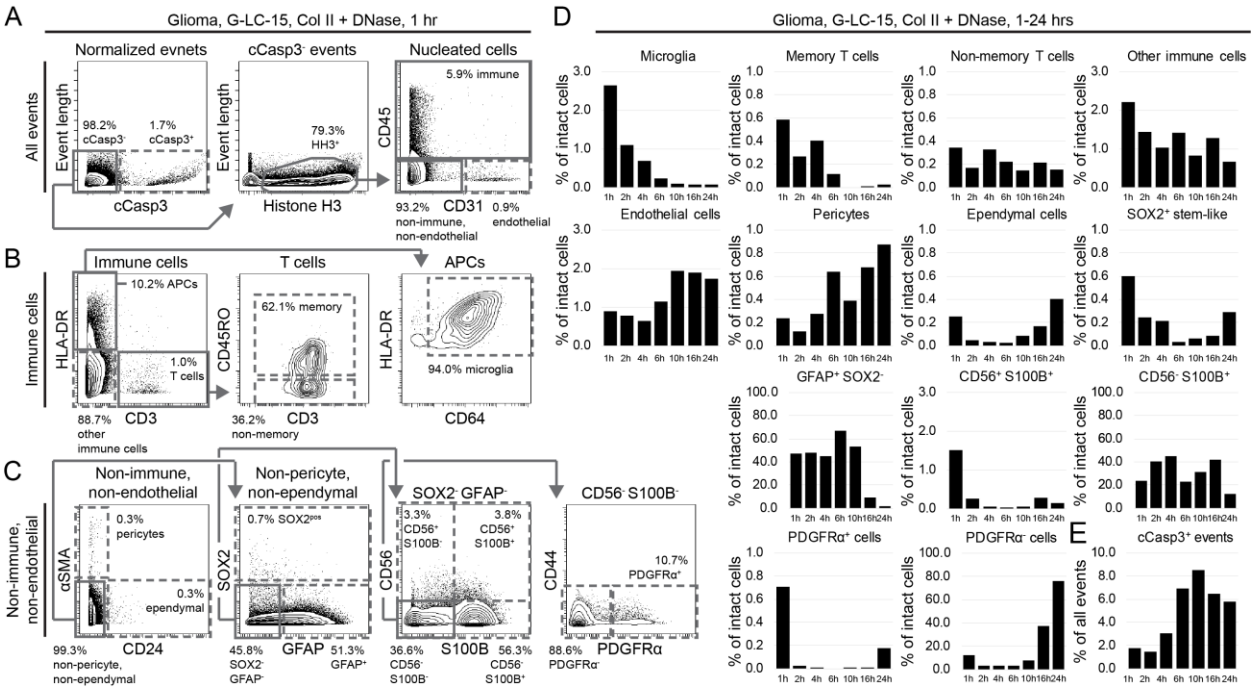

Figure 4-5 Enzymatic treatment times longer than one hour differentially impact glioma tumor cell subsets. Biaxial plots and bar graphs quantify cell subsets measured in mass cytometry analysis of glioma G-LC-15 after varying treatment times with collagenase II and DNase. (A) Gating for apoptotic cells ($cCasp3^+$) and live immune cells ($cCasp3^-CD45^+$), endothelial cells ($cCasp3^-CD31^+$), and non-immune, non-endothelial cells ($cCasp3^-CD45^-CD31^-$). (B) Subsets of glioma tumor-infiltrating immune cells were identified, including microglia ($HLA\text{-}DR^+CD64^+$), $CD45RO^+$ and $CD45RO^-$ subsets of $CD3^+$ T cells, and other immune cells. (C) Pericytes ($CD45^-CD31^-\alpha SMA^+$), ependymal cells ($CD45^-CD31^-CD24^+$), $SOX2^+$ stem-like cells ($CD45^-CD31^-SOX2^+$), $GFAP^+$ cells ($CD45^-CD31^-GFAP^+$), and astrocyte-like cells ($CD45^-CD31^-S100B^+$) were quantified as subsets of G-LC-15. (D) Gating for cell types as in (A-C) was applied to mass cytometry analysis of cells from G-LC-15 treated with collagenase II plus DNase for 1, 2, 4, 6, 10, 16, or 24 hours. (E) Percentage of apoptotic cells as in (A) was measured for each dissociation time, as in (D).

Table 4-1 Mass and fluorescence cytometry detect comparable frequencies of cell types in glioma, melanoma, and tonsil tissue.

Table 1 - Mass and fluorescence cytometry detect comparable frequencies of cell types in glioma, melanoma, and tonsil tissue

Tissue	Subsets	Percent†		R*	Rank		⊠§
		MC	FC		MC	FC	
Glioma G-RT-06	$CD56^{+}GFAP^{-}$	0.7	0.1	0.97	1	1	0.93
	Endothelial cells	1.0	0.8		2	3	
	$CD56^{+}GFAP^{+}$	1.1	0.2		3	2	
	$CD56^{-}GFAP^{-}$	11.4	6.1		4	4	
	$CD56^{-}GFAP^{+}$	18.1	15.4		5	6	
	T cells	27.8	15.1		6	5	
	Other immune cells	39.3	30.9		7	7	
Tonsil T02-23	Non-APCs	2.1	2.5	0.98	1	2	0.90
	Non-immune	5.2	2.3		2	1	
	$CD44^{-}$ APCs	16.2	17.7		3	3	
	T cells	27.1	33.8		4	4	
	$CD44^{+}$ APCs	40.3	39.1		5	5	

† Frequency of terminal populations (dashed gates in Figure 3, percent) was measured by mass cytometry (MC) or fluorescence cytometry (FC)
* Pearson's correlation coefficient R
§ Spearman's ranked ρ

Supplemental Figures and Tables

Leelatian et al., Supplementary Figure S1

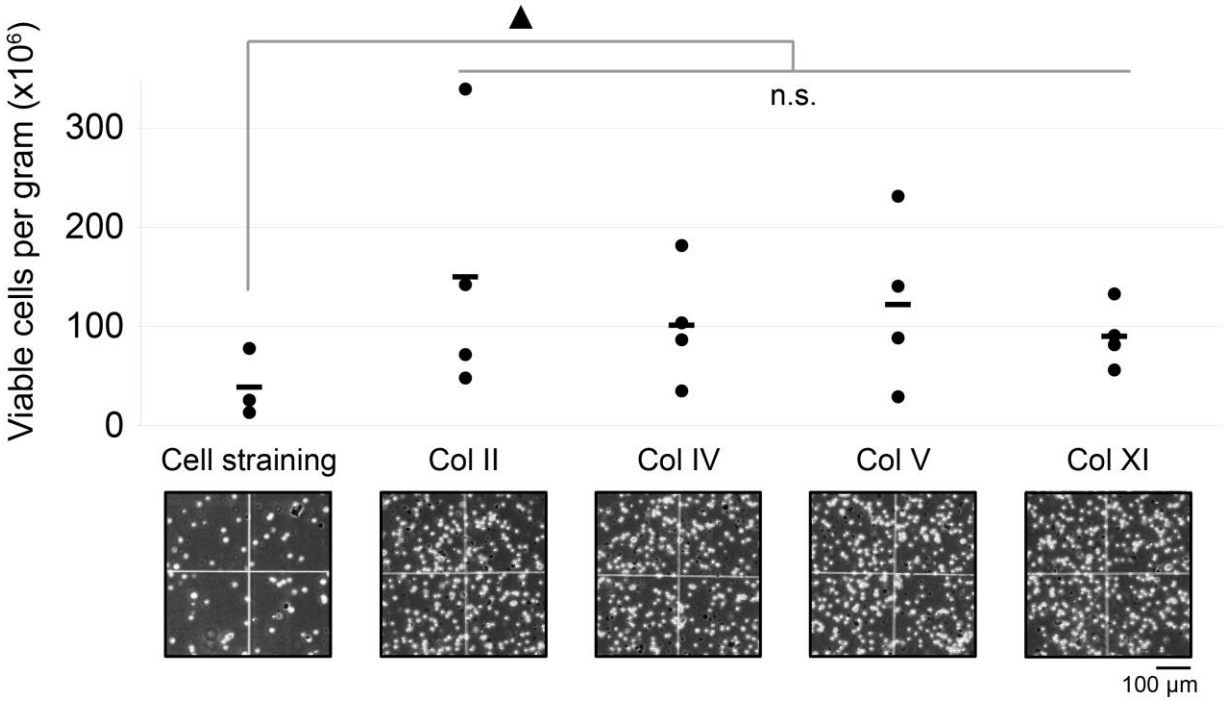

Figure 4-6 (S1) Tonsil dissociation with fine mincing and enzymes gave higher live cell yield compared to conventional dissociation method. Enzymatic dissociations of tonsils by fine mincing and incubation with collagenases and DNase (2 hours) were compared to traditional mechanical dissociation (see *Materials and Methods*). Viable cells (x10^6) per gram of tissue were quantified. Average live cell yield of each condition are shown as horizontal lines. Scale bars = 100 µm. (n.s. = not significant; Col = collagenase; no enz = no enzyme; HyQ = HyQTase; Tryp = TrypLE). (Cell straining, N = 3; Col, N = 4). (▲ $p < 0.05$)

Leelatian et al., Supplementary Figure S2

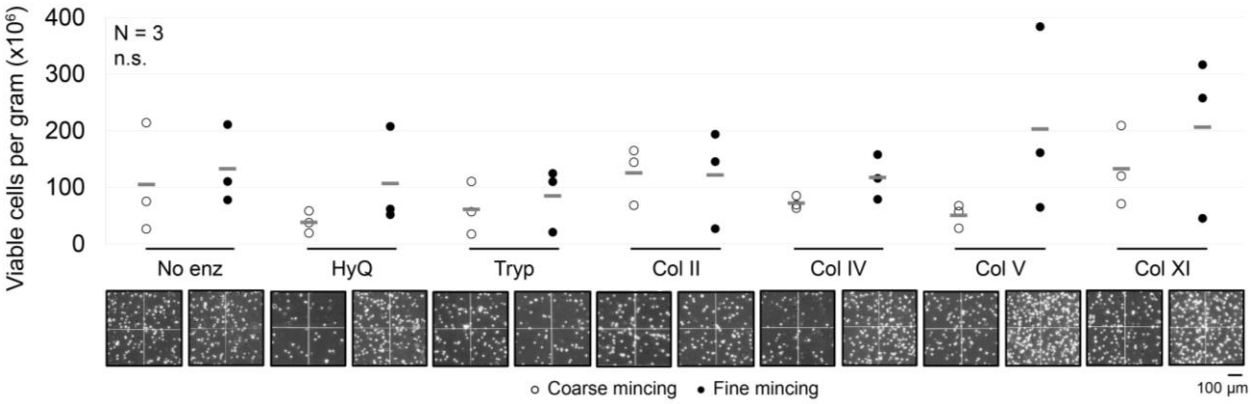

Figure 4-7 (**S2**) **Fine mincing did not adversely affect live cell yield from tonsil dissociation.** Live cell yield (x10^6) per gram of tonsils obtained by coarse (open circles) and fine (filled circles) mincing of tonsils were compared after a 2-hour incubation in different enzyme combinations. All conditions contained DNase. Average live cell yield of each condition are shown as horizontal lines. Representative Trypan Blue stained images of each conditions are shown. Scale bars = 100 µm. (n.s. = not significant; Col = collagenase; no enz = no enzyme; HyQ = HyQTase; Tryp = TrypLE).

Leelatian et al., Supplementary Figure S3

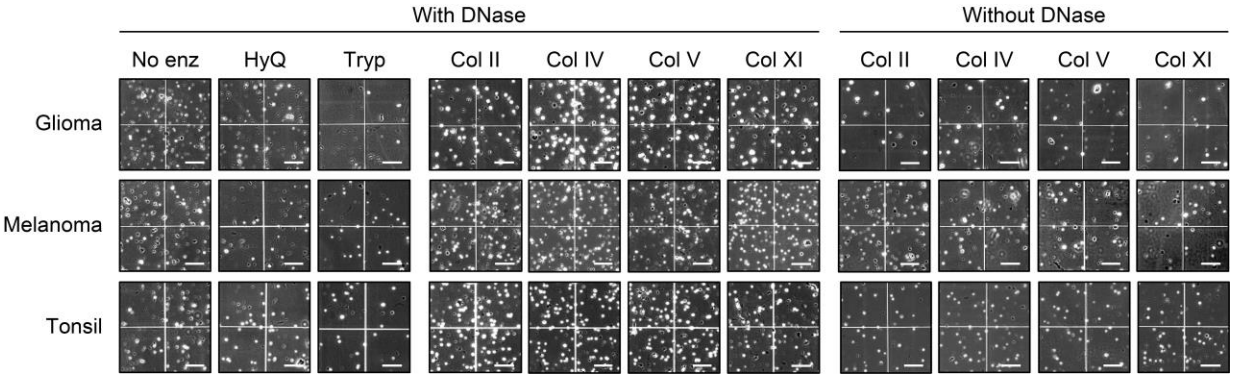

Figure 4-8 (S3) Trypan Blue staining allowed quantification of live cell yield. Higher resolution of Trypan Blue stains shown in Figure 1. No enz = no enzyme; HyQ = HyQTase; Tryp = TrypLE; Col =collagenase. Scalebars = 100 µm.

Leelatian et al., Supplementary Figure S4

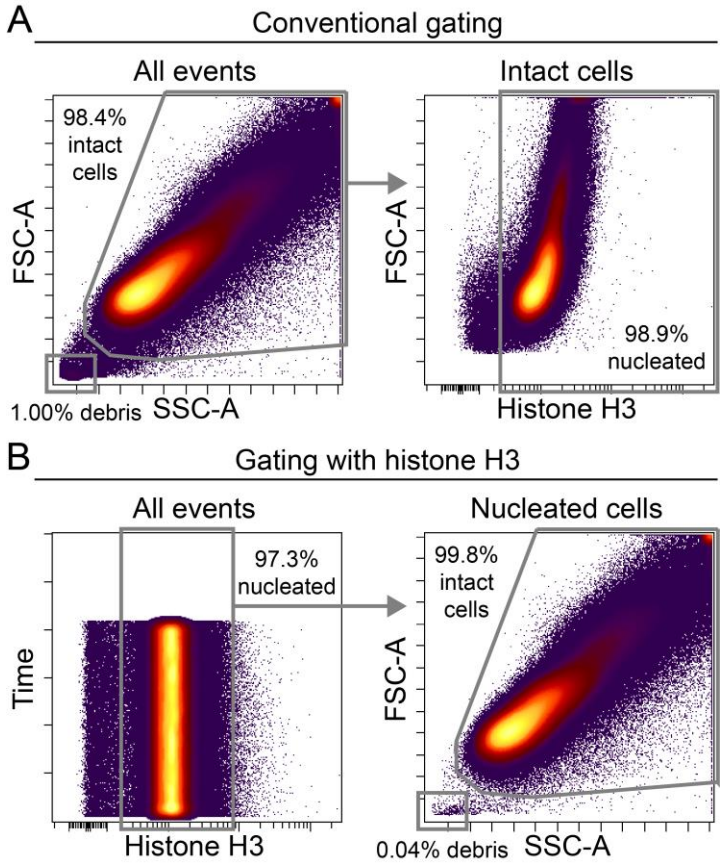

Figure 4-9 (**S4**) **Histone H3 effectively identifies intact Jurkat cells via fluorescence flow cytometry. (**A) Intact Jurkat T cells (98.4%) were identified by conventional biaxial analysis using SSC-A (x-axis) and FSC-A (y-axis). 98.9% of intact Jurkat cells were $HH3^{+}$ (nucleated). (B) Sequential gating starting with HH3 identified 97.3% nucleated events, 99.8% of which were defined as intact cells based on FSC-A and SSC-A biaxial analysis.

Leelatian et al., Supplementary Figure S5

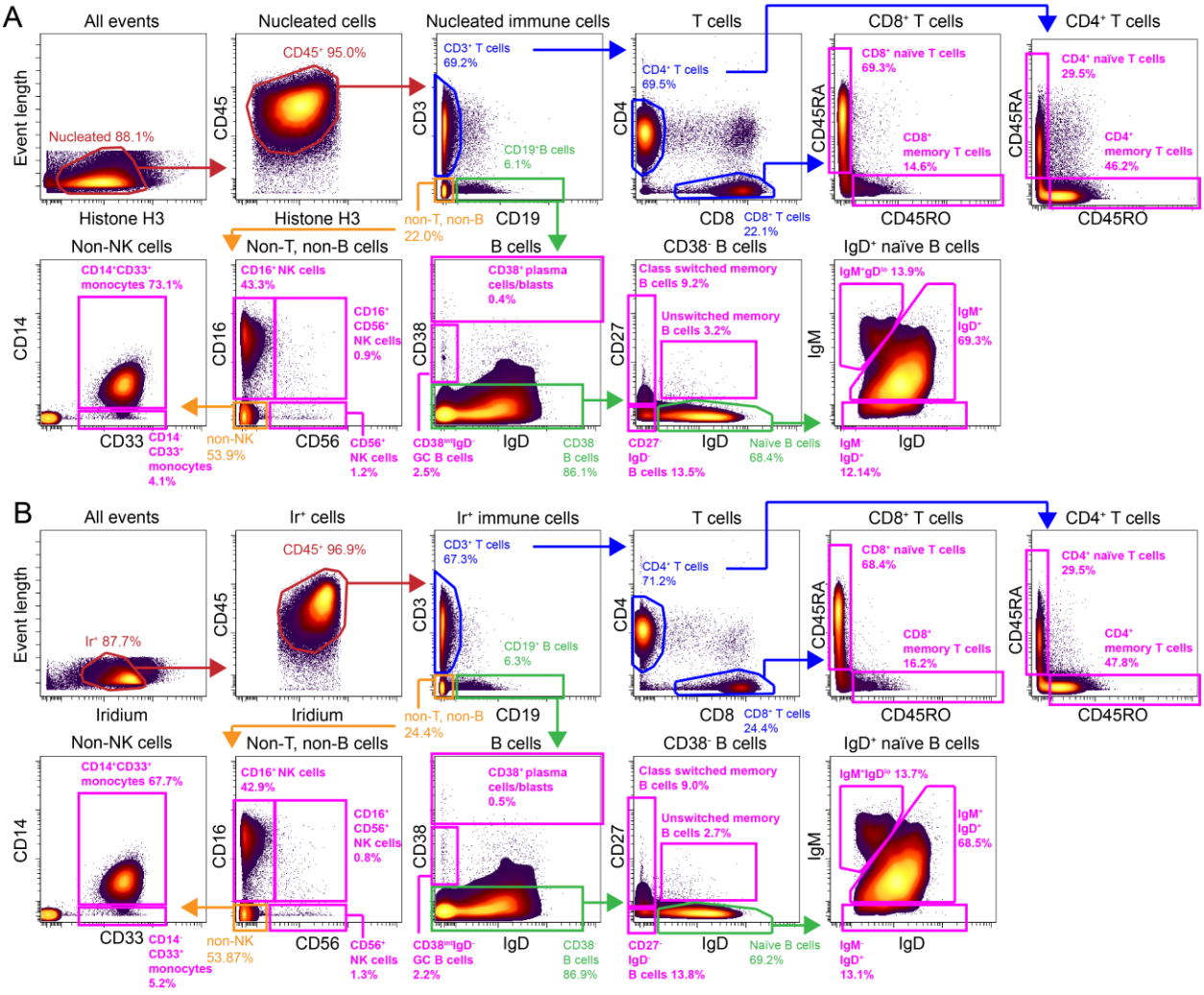

Figure 4-10 (S5) Histone H3 is an antibody-based nucleated cell marker for mass cytometry. Live surface stained healthy human PBMCs were stained intracellularly with HH3 antibody and iridium. Either HH3 (A) or iridium (Ir) (B) was used for the initial intact cell gates. $CD45^+$ events were identified. Sequential biaxial gating was used to identify known cell subsets from either $HH3^+CD45^+$ or Ir^+CD45^+ events. Gating subsets of $CD45^+$ immune cells is the same for both $HH3^+$ nucleated cells and Ir^+ intact cells. Pearson analysis and Spearman rank comparing abundance of terminal cell subsets (fuchsia) gated using either HH3 or iridium as intact cell marker are shown in Table S3.

Leelatian et al., Supplementary Figure S6

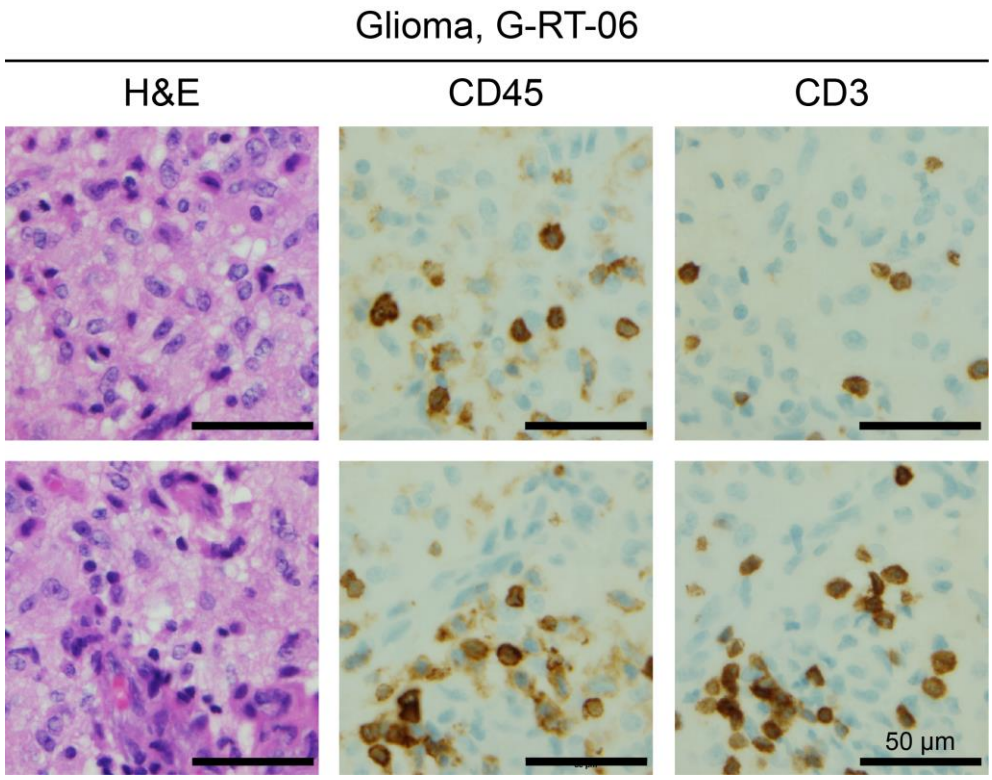

Figure 4-11 (S6) Glioma infiltrating immune cells were identified by immunohistochemistry. Hematoxylin and eosin (H&E) stains of FFPE sections of glioma, G-RT-06, are shown. IHC stains with CD45 and CD3 antibodies of the same sample are also depicted. Scale bars = 50 µm

Leelatian et al., Supplementary Figure S7

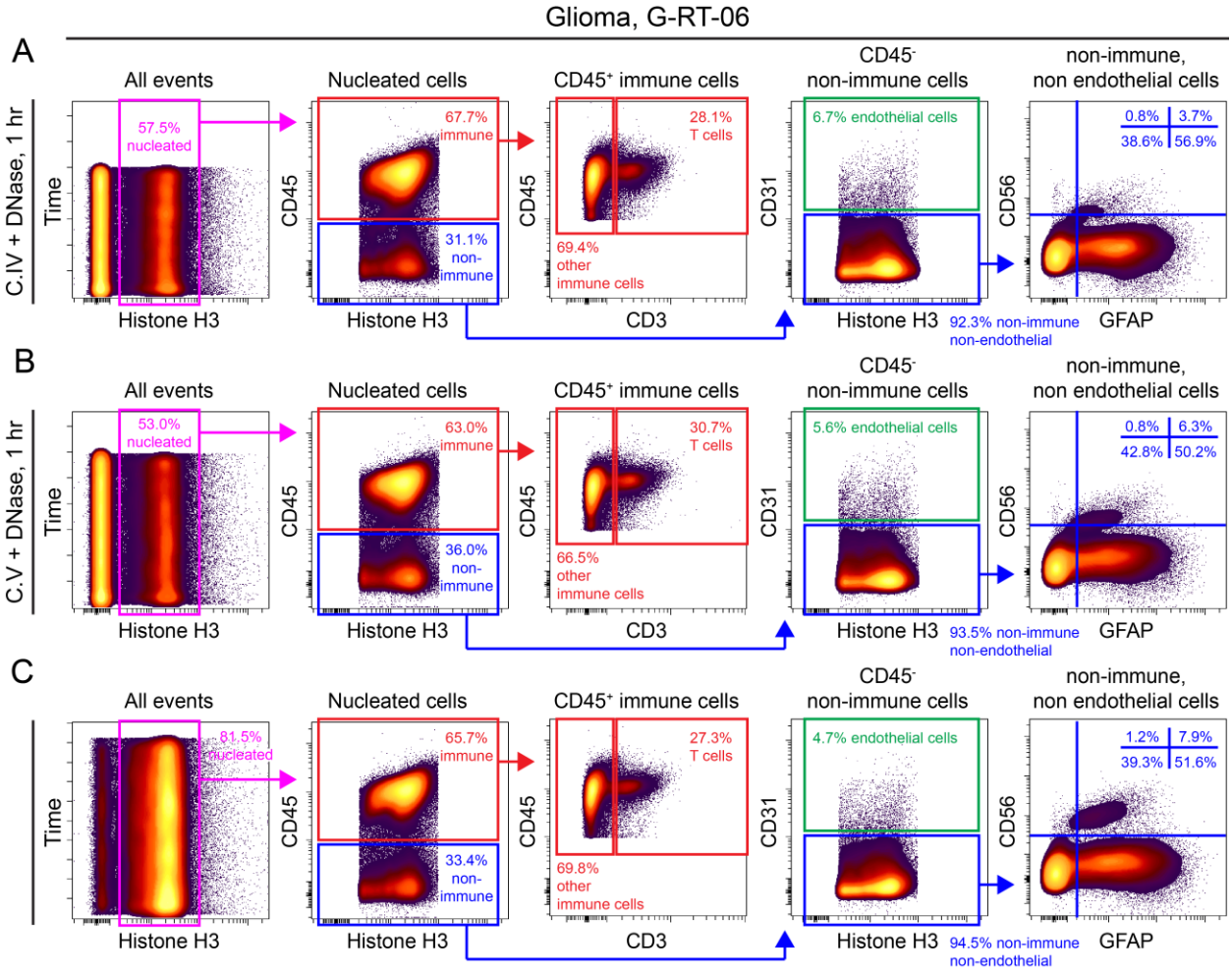

Figure 4-12 (**S7**) **Known cell subsets in glioma were identified by fluorescence flow cytometry after dissociation with either collagenase IV, V, or XI.** Sequential biaxial gating of glioma G-RT-06 after 1-hour dissociation with DNase plus either (A) Col IV, (B) Col V, or (C) Col XI is shown. The gates shown are the same used in DNase plus Col II dissociation of the same glioma shown in Figure 3A. Abundance of subsets are shown as percentages.

Leelatian et al., Supplementary Figure S8

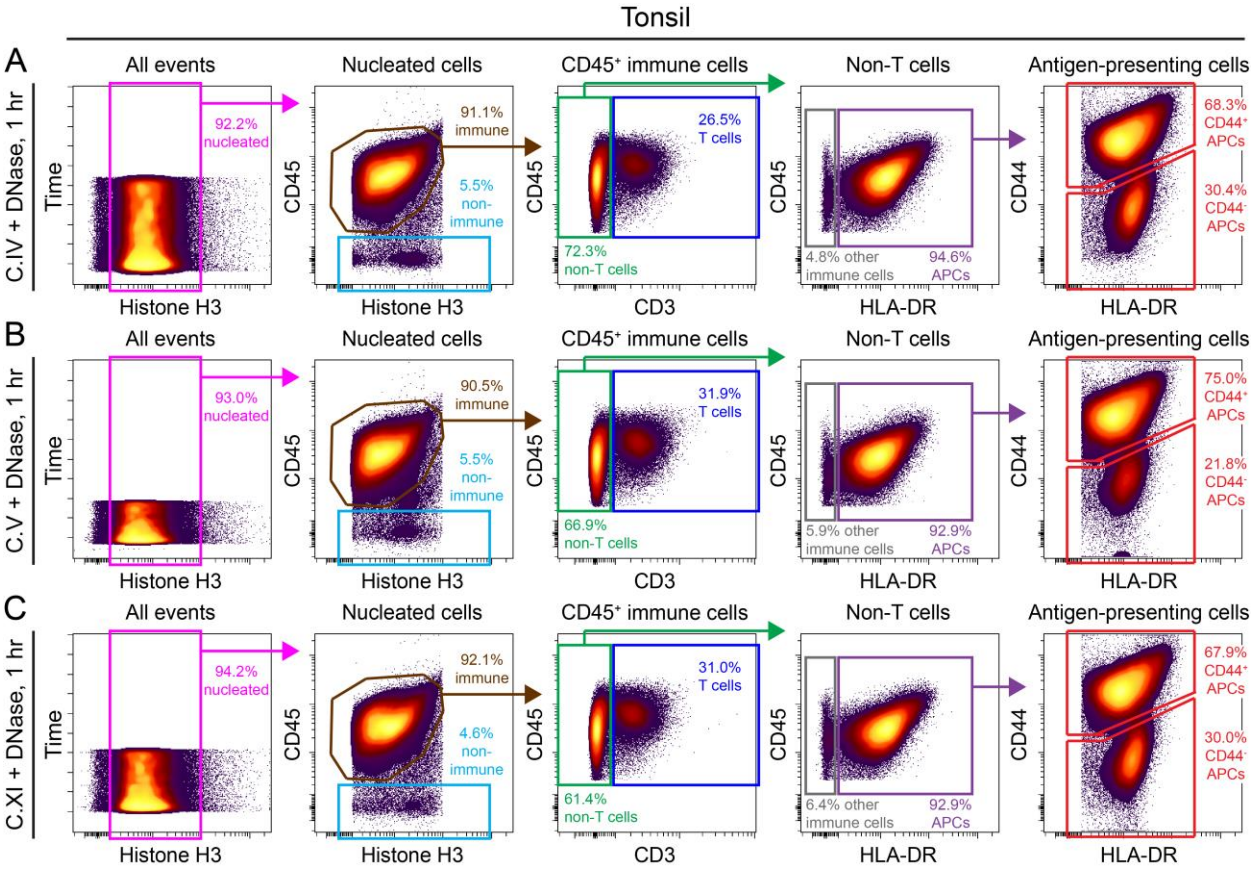

Figure 4-13 (**S8**) **Known cell subsets in tonsil were identified by fluorescence flow cytometry after dissociation with either collagenase IV, V, or XI.** Biaxial gating of patient-derived tonsil after 1-hour dissociation with DNase plus either (A) Col IV, (B) Col V, or (C) Col XI, is shown. Gating scheme is similar to that used to identify cell subsets of the same tonsil sample after DNase plus Col II dissociation shown in Figure 3C. Abundance of cell subsets are shown as percentages.

Leelatian et al., Supplementary Figure S9

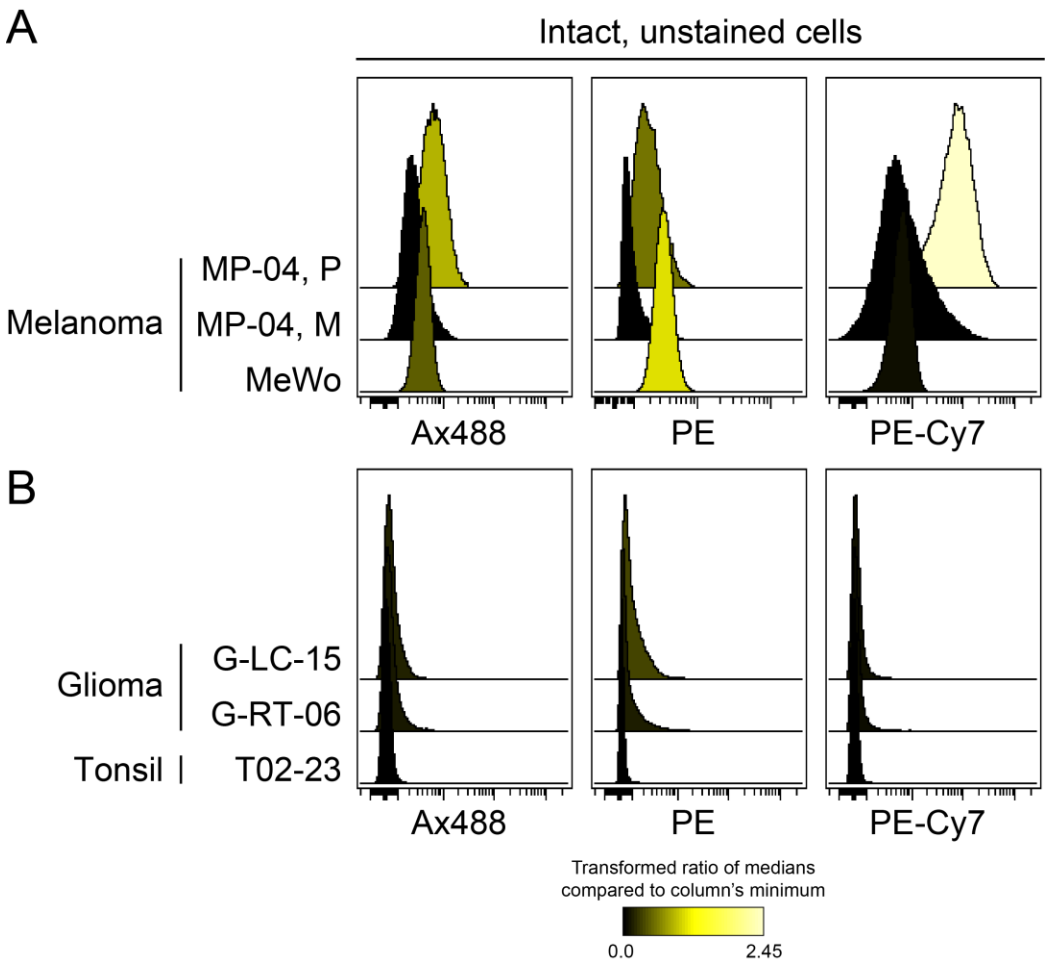

Figure 4-14 (S9) Unstained melanoma cells showed variable auto-fluorescence signal. (A) Unstained intact cells from primary (P) and metastatic (M) sites of melanoma MP-04, as well as MeWo melanoma cell line, and (B) two patient-derived glioma samples (G-LC-15, and G-RT-06) and one tonsil (T02-23), were measured for their auto-fluorescence signal on Ax488, PE, and PE-Cy7 channels. Histograms display transformed ratio of medians of signal intensity compared with the minimal signal of each column (channel).

Leelatian et al., Supplementary Figure S10

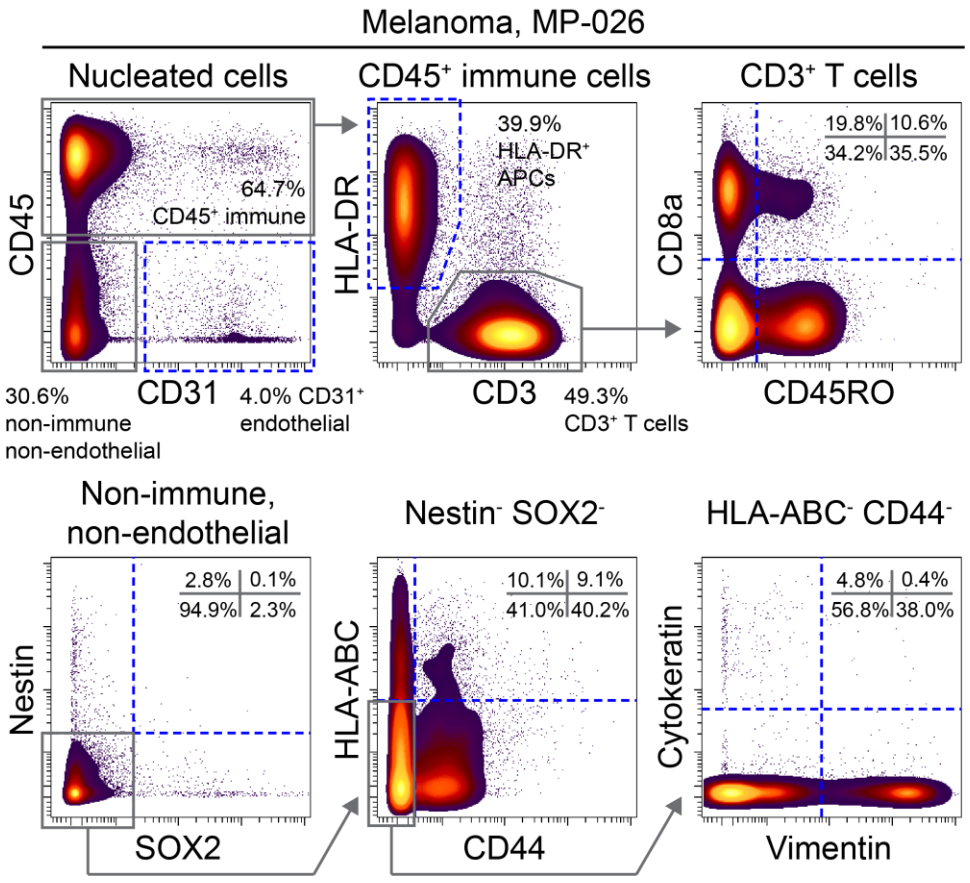

Figure 4-15 (**S10**) **– Cell subsets in melanoma can be characterized by mass cytometry.** HH3^{+} nucleated cells from melanoma sample MP-026, identified by mass cytometry, were characterized for cell subsets by biaxial analysis. Immune cell subsets, endothelial cells, and non-immune, non-endothelial cell subsets were identified using 12 cell identity markers (CD45, CD31, HLA-DR, CD3, CD8a, CD45RO, Nestin, SOX2, HLA-ABC, Cytokeratin, and Vimentin).

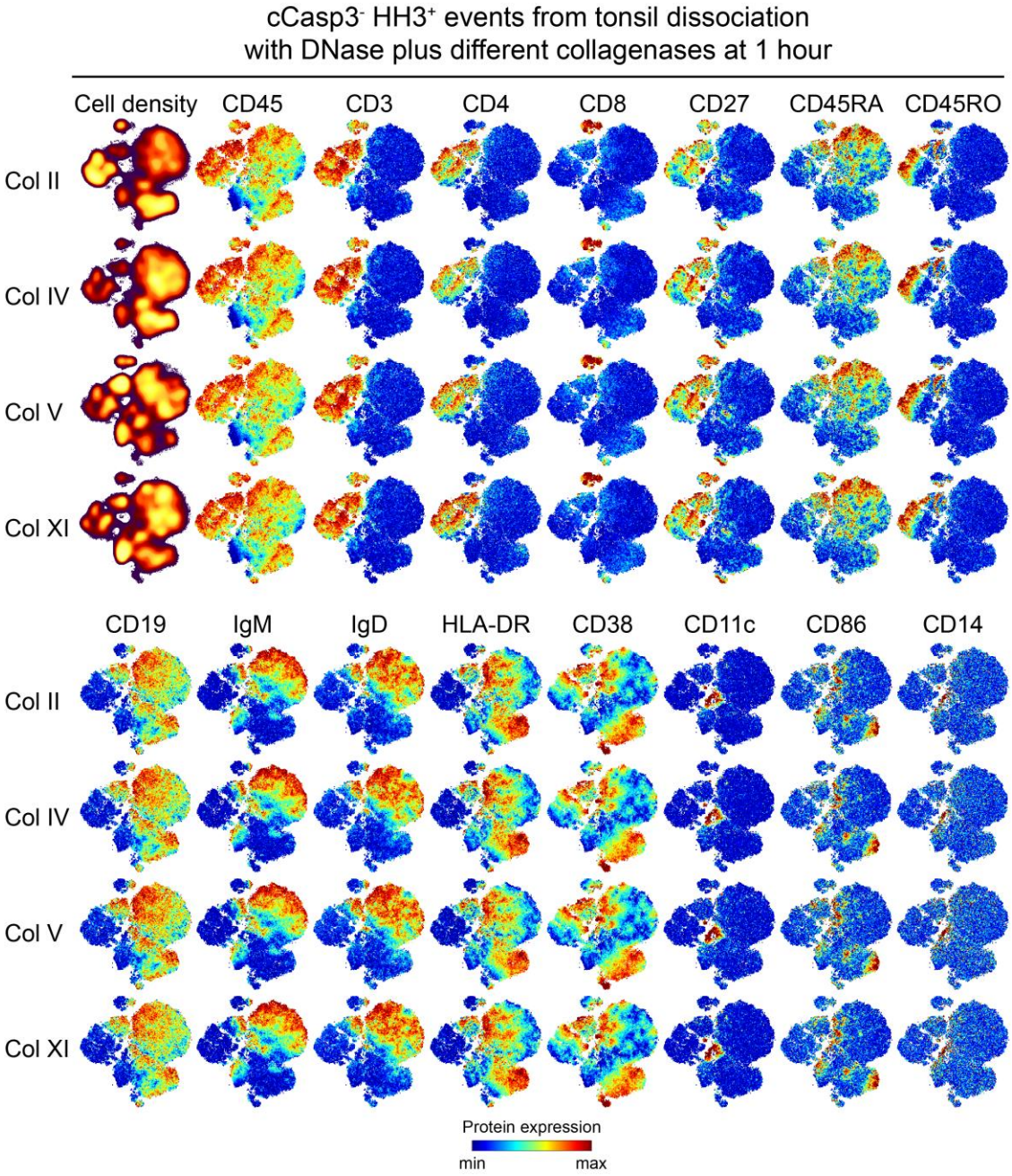

Figure 4-16 (**S11**) **Presence and abundance of tonsil cell subsets were comparable after 1-hour dissociation with different types of collagenases plus DNase.** Patient-derived tonsils were dissociated for 1 hour with DNase plus either Col II, IV, V, or XI. Nucleated ($HH3^+$) $cCasp3^-$ events were mapped simultaneously by viSNE. Contour plots of different dissociation conditions are shown to illustrate cell density (first column, top row). Heat plots show expression of 15 cell identity markers (CD45, CD3, CD4, CD8, CD27, CD45RA, CD45RO, CD19, IgM, IgD, HLA-DR, CD38, CD11c, CD86, and CD14).

Leelatian et al., Supplementary Figure S12

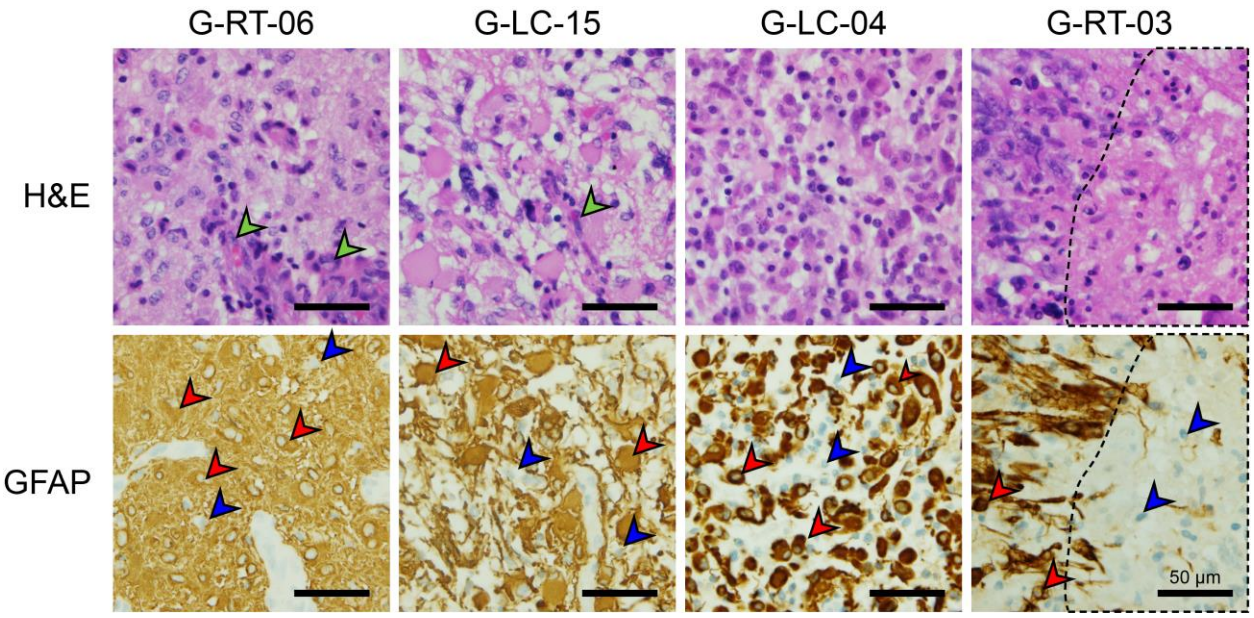

Figure 4-17 (**S12**) **GFAP$^+$ cell subsets are present in gliomas.** Hematoxylin and eosin (H&E) stains of 4 gliomas are shown (top row). Green arrowheads depict blood vessels or vascular proliferation, and dashed borders show area of necrosis. GFAP staining (bottom row) of the same tumors illustrates GFAP$^+$ (red arrowheads) and GFAP$^-$ (blue arrowheads) cells. Scale bars = 50 µm.

Leelatian et al., Supplementary Figure S13

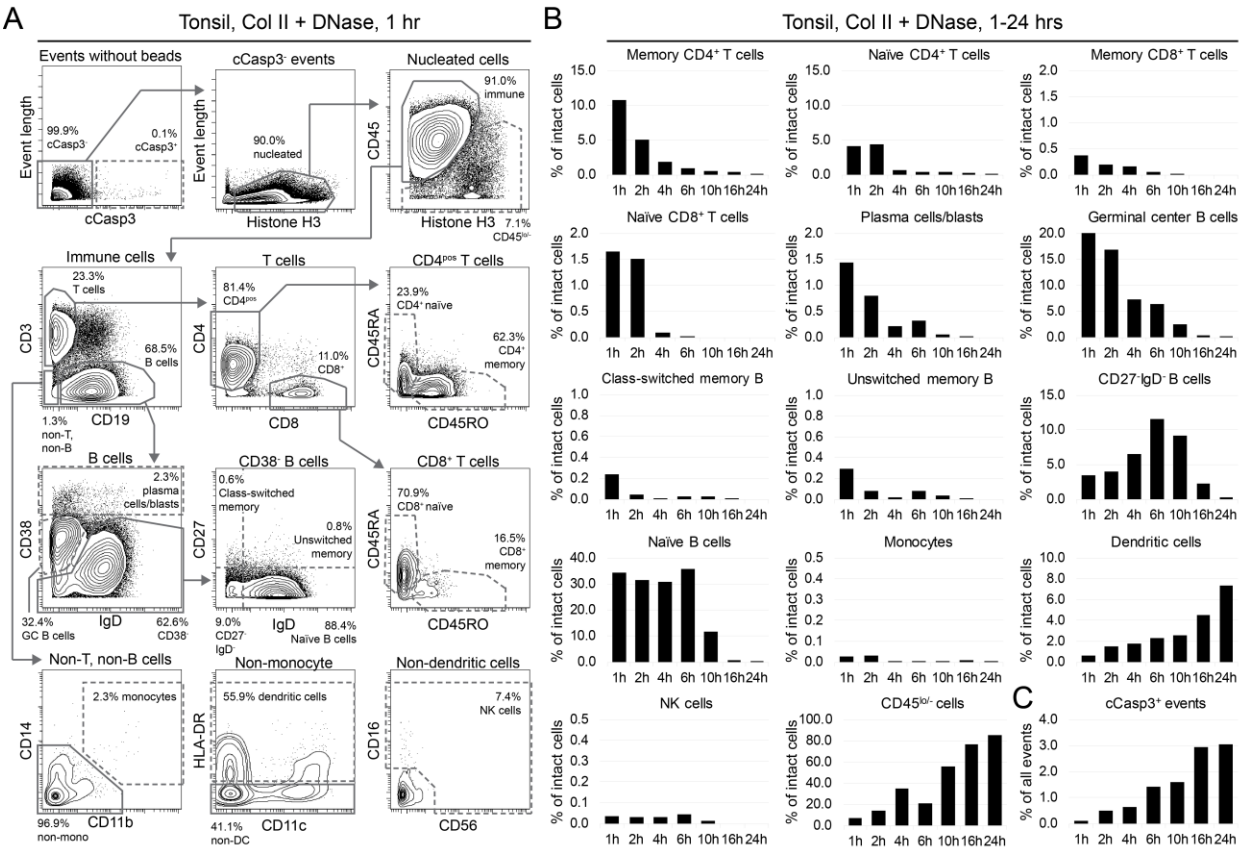

Figure 4-18 (S13) Disproportionate depletion and selection of immune cell subsets was observed in tonsil samples with collagenase II dissociation over time. (A) Biaxial gating was used to identify apoptotic ($cCasp3^+$) events, as well as intact nucleated immune cell subsets, in tonsils after 1-hour dissociation with Col II plus DNase. Terminal gates are outlined as dashed gates. (B) A similar gating scheme as in (A) was applied to cells obtained from different duration after dissociation with Col II plus DNase (x-axis) of the same tonsil sample. Abundance of terminal cell subsets were quantified as percentages compared to non-apoptotic nucleated ($cCasp3^-HH3^+$) cells (y-axis). (C) Abundance of apoptotic cells from different time points after dissociation is shown as percentage compared to all events.

Table 4-2 (S1) Fluorescence antibodies

Target	Dye	Clone	Company	Staining		Panels	
				Live	MeOH	Glio	Ton
CD3	BUV395	UCHT1	BD	✓		+	+
Histone H3	Pacific Blue	D1H2	CST		✓	+	+
CD45	BV786	HI30	BD		✓	+	+
CD19	Ax488	HIB19	BioLegend	✓			+
CD56	Ax488	HCD56	BioLegend	✓		+	
Nestin	Ax594	10C2	BioLegend		✓		
CD44	PE	BJ18	BioLegend		✓		+
CD31	PE-Cy7	WM59	BD		✓	+	
HLA-DR	Ax647	L243	BioLegend	✓			+
GFAP	Ax647	1B4	BD		✓	+	
MCAM	APC	SHM-57	BioLegend		✓		
Dead	Ax700	-	Invitrogen	✓		+	+

Table 4-3 (S2) Mass cytometry antibody panel for healthy PBMCs

Target	Mass	Clone	Company	Staining	
				Live	MeOH
CD4	145	RPA-T4	Fluidigm	✓	
IgD	146	IA6-2	Fluidigm	✓	
CD16	148	3G8	Fluidigm	✓	
CD45RO	149	UCHL1	Fluidigm	✓	
CD45RA	153	HI100	Fluidigm	✓	
CD45	154	HI30	Fluidigm	✓	
CD27	155	L128	Fluidigm	✓	
CD33	158	WM53	Fluidigm	✓	
CD14	160	M5E2	Fluidigm	✓	
CD19*	161	HIB19	BioLegend	✓	
CD38	167	HIT2	Fluidigm	✓	
CD8	168	SK1	Fluidigm	✓	
CD3	170	SP34-2	Fluidigm	✓	
IgM	172	MHM-88	Fluidigm	✓	
CD56*	175	HCD56	BioLegend	✓	
Histone H3	176	D1H2	Fluidigm		✓
Iridium	191	-	Fluidigm		✓

* Custom conjugated

Table 4-4 (S3) Pearson analysis and Spearman rank comparing histone H3 and Iridium as intact cell markers

PBMC subsets	Percent		Pear	Rank		Spear
	HH3	Ir	(R)	HH3	Ir	(ρ)
Plasma cells/blasts	0.02	0.03		1	1	
Germinal center B cells	0.2	0.1		2	2	
Unclass-switched memory B cells	0.2	0.2		3	3	
$CD16^{pos}CD56^{pos}$ NK cells	0.2	0.2		4	4	
$CD56^{pos}$ NK cells	0.3	0.3		5	5	
$IgM^{neg}IgD^{pos}$ naïve B cells	0.4	0.5		6	7	
Class-switched memory B cells	0.5	0.5		7	6	
$CD33^{pos}CD14^{neg}$ monocytes	0.5	0.7		8	9	
$IgM^{pos}IgD^{lo}$ naïve B cells	0.5	0.5	1.00	9	8	1.00
$CD27^{neg}IgD^{neg}$ B cells	0.7	0.8		10	10	
Memory $CD8^{pos}$ T cells	2.2	2.6		11	11	
$IgM^{pos}IgD^{pos}$ naïve B cells	2.4	2.6		12	12	
$CD14^{pos}CD33^{pos}$ monocytes	8.7	8.9		13	13	
$CD16^{pos}$ NK cells	9.5	10.5		14	14	
Naïve $CD8^{pos}$ T cells	10.5	11.4		15	15	
Naïve $CD4^{pos}$ T cells	14.1	14.1		16	16	
Memory $CD4^{pos}$ T cells	21.9	22.9		17	17	

HH3 = Histone H3; Ir = iridium; Pear = Pearson analysis; Spear = Spearman rank; ρ = Spearman rho
Percent = % of each subset compared to either $HH3^{pos}CD45^{pos}$ cells, or $Ir^{pos}CD45^{pos}$ cells

Table 4-5 (S4) **Mass cytometry antibody panels for dissociated solid tissues and tumors**

Target	Mass	Clone	Company	Staining			Panels		
				Live	Sap	MeOH	Glio	Mel	Ton
HLA-ABC	141	W3-32	Fluidigm	✓				+	
cCasp3	142	D3E9	Fluidigm			✓	+	+	+
CD11b	144	ICRF44	Fluidigm	✓					+
CD31	145	WM59	Fluidigm			✓	+	+	
CD4	145	RPA-T4	Fluidigm	✓					+
CD64	146	10.1	Fluidigm	✓			+		
IgD	146	IA6-2	Fluidigm	✓					+
CD8a	146	RPA-T8	Fluidigm	✓				+	
CD16	148	3G8	Fluidigm	✓					+
CD45RO	149	UCHL1	Fluidigm	✓			+	+	+
S100B*	153	19-S100B	BD			✓	+		
CD45RA	153	HI100	Fluidigm	✓					+
CD45	154	HI30	Fluidigm			✓	+	+	+
CD27	155	L128	Fluidigm	✓					+
CD86	156	IT2.2	Fluidigm	✓					+
Vimentin	156	RV202	Fluidigm			✓		+	
CD33	158	WM53	Fluidigm	✓					+
CD11c	159	Bu15	Fluidigm	✓					+
CD14	160	M5E2	Fluidigm	✓					+
PDGFRα*	161	16A1	BioLegend	✓			+		
CD19*	161	HIB19	BioLegend	✓					+
Cytokeratin	161	C-11	Fluidigm			✓		+	
SOX2*	163	O30-678	BD		✓		+	+	
CD24	166	ML5	Fluidigm	✓			+		
CD38	167	HIT2	Fluidigm	✓					+
Nestin*	168	10C2	BioLegend			✓		+	
CD8	168	SK1	Fluidigm	✓					+
CD44*	169	BJ18	BioLegend			✓	+	+	
CD3	170	SP34-2	Fluidigm	✓			+	+	+
GFAP*	171	1B4	BD			✓	+		
IgM	172	MHM-88	Fluidigm	✓					+
αSMA*	173	ab54723	Abcam			✓	+		
HLA-DR	174	L243	Fluidigm	✓			+	+	+
CD56*	175	HCD56	BioLegend	✓			+		+
Histone H3	176	D1H2	Fluidigm			✓	+	+	+

* Custom conjugated
Sap = 0.02% saponin; Glio = glioma; Mel = melanoma; Ton = tonsil

CHAPTER V

BRAF AND MEK INHIBITOR THERAPY ELIMINATES NESTIN EXPRESSING MELANOMA CELLS IN HUMAN TUMORS

Authors: Deon B. Doxie[1,2], Allison R. Greenplate [1,2,3], Jocelyn S. Gandelman[2,3,4], Kirsten E. Diggins[1,2], Caroline E. Roe[1,2,3], Kimberly B. Dahlman[2], Jeffrey A. Sosman[4], Mark C. Kelley[2,5], and Jonathan M. Irish[1,2,3]

This work is presented as it appears in its manuscript form to *Pigment Cell and Melanoma Research* 2018.

Preface

Chapter 5 utilizes single cell approaches demonstrated in Chapters 2-4 to characterize dabrafenib and trametinib responses in *BRAF*^{V600mut} melanoma. Recent studies that utilize transcriptional profiling have identified resistant cells in relapsed tumors, however, these results don't align to identify a common resistant cell phenotype. From biomarker characterization of 32 cells expressed by cells my analysis revealed patients contained distinctly heterogeneous populations of cells before therapy, however, a common phenotype emerged after combination targeted therapy. Treatment strategies have recently begun to move towards combining immune checkpoint blockade and targeted therapies in patients simultaneously. Because this approach revealed new in-vivo biology that has not been documented previously, I believe this approach could be useful for evaluating the treatment response of new treatment strategies.

Summary

Little is known about the in vivo impacts of targeted therapy on melanoma cell abundance and protein expression. Here, 21 antibodies were added to an established melanoma mass cytometry panel to measure 32 cellular features, distinguish malignant cells, and characterize dabrafenib and trametinib responses in $BRAF^{V600mut}$ melanoma. Tumor cells were biopsied before neoadjuvant therapy and compared to cells surgically resected from the same site after 4 weeks of therapy. Approximately 50,000 cells per tumor were characterized by mass cytometry and computational tools t-SNE/viSNE, FlowSOM, and MEM. The resulting single cell view of melanoma treatment response revealed initially heterogeneous melanoma tumors were consistently cleared of Nestin expressing melanoma cells. Melanoma cells subsets that persisted to week 4 were heterogeneous but expressed SOX2 or SOX10 proteins and specifically lacked surface expression of MHC I proteins by MEM analysis. Traditional histology imaging of tissue microarrays from the same tumors confirmed mass cytometry results, including persistence of NES- SOX10+ S100β+ melanoma cells. This quantitative single cell view of melanoma treatment response revealed protein features of malignant cells that are not eliminated by targeted therapy.

Significance

This study creates a 32-marker mass cytometry panel for melanoma and applies it to deeply characterize melanoma cell protein expression signatures before and after neoadjuvant therapy targeting BRAF and MEK. Targeted therapy is revealed to clear Nestin-expressing melanoma cells, which are considered a hallmark of aggressive, metastatic melanoma. Persisting subsets after targeted therapy also lacked surface expression of MHC I, which may inform strategies for combining targeted therapy and immunotherapy. This study reveals new in vivo biology of melanoma cells that can be used as a reference point for patient-derived xenograft and cell line research models.

Introduction

Study of melanoma and other solid tumors has increasingly moved towards approaches that monitor the collection of cell types within tumors including cancer cells, immune cells, fibroblasts, and other stromal cells (Irish, 2014). Studying the heterogeneous cells within patients' tumors could identify malignant or immunologic cell types that may predict treatment response or resistance (Johnson et al., 2016). Only recently have studies begun to perform single cell analysis on matched tumors from patients before and after therapy (Hugo et al., 2015; Tirosh et al., 2016). These single cell studies have focused on RNA expression and use measurements of selected proteins as a confirmation tool. Pairing longitudinal studies with single cell analysis of proteins involved in melanoma cell identity and function could lead to a better understanding of the evolution of resistance and therapy evasion (Irish, 2014; Meacham and Morrison, 2013).

Technological advances have led to the development of several platforms made to dissect cell diversity. Single-cell genomic approaches enable a detailed evaluation of genomic and transcriptional features of cancer cells (Patel et al., 2014; Tirosh et al., 2016). While studies that utilize transcriptional profiling have identified resistant cells in relapsed tumors, these results don't align to identify a common resistant cell phenotype (Hugo et al., 2015; Tirosh et al., 2016). Furthermore, discrepancies between mRNA and protein expression indicate not all transcripts are regulated in a way that leads to detectable levels of protein (Koussounadis et al., 2015; Zhang et al., 2014b). Mass cytometry uses metal labeled antibodies detected using time-of-flight mass spectrometry, permitting detection of more than 30 proteins per cell (Bendall et al., 2011; Bjornson et al., 2013). The use of metal

labeled, rather than fluorophore-labeled, antibody tags significantly reduces issues with spectral overlap and cell autofluorescence (Leelatian et al., 2017a; Nicholas et al., 2016). Due to these advantages, mass cytometry has gained acceptance for the study of solid tissues (Wang et al., 2016; Wogsland et al., 2017). More recently, standardized methods have been developed to create viable single cell suspensions from solid tumors and tissues (Leelatian et al., 2017b).

This study introduces the application of mass cytometry to study the cell diversity of human melanoma tumors by measuring 32 proteins simultaneously before and during ongoing targeted therapy from the same tumor sites. This work aims to characterize and track changes to cancer cell phenotype that appear during combination $BRAF^{V600E}$ and MEK inhibition. By simultaneously measuring several proteins in tens of thousands of cells, mass cytometry could reveal novel features defining subsets that may be used for future therapeutic development (Irish, 2014; Spitzer and Nolan). Ideally, by revealing new cell types and their signature features, a single cell systems biology approach might both provide ways to track heterogeneous melanoma cell subsets and discover new hypotheses for cellular mechanisms of resistance.

Materials & Methods

Cell Culture and Cell Lines. MeWo, A2058, WM115, and SKMEL28 cells were grown in Minimum Essential Medium (Mediatech, Inc., Manassas, VA), supplemented with 10% fetal bovine serum (Gibco standard FBS, Life Technologies, Grand Island, NY), 1% penicillin (Gibco), and 1% streptomycin (Gibco). Jurkat T cells were grown in RPMI (Mediatech, Inc., Manassas, VA) supplemented with 10% fetal bovine serum (Gibco standard FBS, Life

Technologies, Grand Island, NY), 1% penicillin (Gibco), and 1% streptomycin (Gibco). All cell lines were acquired as gifts from the laboratory of Dr. Vito Quaranta.

Tumor Collection and Dissociation. Lymph nodes and subcutaneous tumors from adults with metastatic melanoma were biopsied or surgically resected from 15 individual patients accordance with the Declaration of Helsinki. Institutional ethics approval was obtained from the Vanderbilt Institutional Review Board (project numbers 121165 and 030220). All patients had provided written informed consent prior to inclusion in the study. All patients in this study presented with either several subcutaneous legions or distal metastasis. All tumors within the study were thought to arise as cutaneous legions because no evidence of disease was present in mucosal epithelium or retinas. 11 patients received two weeks of $BRAF^{V600E}$ inhibitor dabrafenib followed by two weeks of dabrafenib and MEK inhibitor trametinib (Supplementary Table S1 and (Johnson et al., 2015)). Pretreatment (Pre-Tx) tumors were naïve to $BRAF^{V600E}$ inhibitor dabrafenib MEK inhibitor trametinib. More details of patients from this clinical study can be found with clinical trial code NCT01701037. Core biopsies were obtained before therapy and remaining tumors were surgically resected after four weeks of therapy. Tumor samples were enzymatically digested into a single-cell suspension and cryopreserved with techniques developed specifically to isolate viable melanoma tumor cells (Leelatian et al., 2017a; Leelatian et al., 2017b). Finally, before and after cryopreservation all samples were inspected with a hemocytometer and trypan blue staining (Thermo Fisher Scientific, Waltham, MA).

Tissue Microarrays and Immunohistochemistry. Melanoma tumors from the study were prepared and processed into TMAs by the VUMC Translational Pathology Shared

Resource (TPSR) (Supplementary Table S1). Immunohistochemistry of serial sections (<10 µm) from TMAs was performed by the VUMC TPSR. Digital images were obtained with an Ariol SL-50 automated scanning microscope and the Leica SCN400 Slide Scanner from VUMC Digital Histology Shared Resource.

Fluorescence Flow Cytometry. Lives cells from patient 001 (MP-001) and Jurkat T cells were stained with fluorescent antibodies to analyze signaling status. Before stimulating cells for signaling, Alexa fluorophore 700 (Thermo Fisher Scientific, Waltham, MA) was added, as previously described (Irish and Doxie, 2014; Leelatian et al., 2017a). Alexa fluorophores can be used to test membrane permeability as a way to exclude dead and dying cells (Irish and Doxie, 2014; Krutzik and Nolan, 2006). Unstimulated cells and stimulated cells were allowed to rest in an incubator for 30 minutes in RPMI (Mediatech, Inc., Manassas, VA), supplemented with 10% fetal bovine serum (Gibco standard FBS, Life Technologies, Grand Island, NY). Stimulated cells were treated with 3.3 mM hydrogen peroxide for 4 minutes. After 34 minutes cells were fixed with 1.6% paraformaldehyde (Electron Microscopy Services, Fort Washington, PA) for 10 min at room temperature, washed with PBS (HyClone Laboratories, Logan, UT), pelleted at 800 × *g,* and permeabilized with 100% ice-cold methanol (Fisher Scientific, Waltham, MA) at −20°C overnight following established protocols (Irish et al., 2010b; Krutzik and Nolan, 2003; Leelatian et al., 2015). Cells were washed twice with cell staining media composed of PBS and 1% BSA (Fisher Scientific, Waltham, MA) and pelleted at 800 *x g*. Each sample was stained with 100 µl staining media for 15 minutes at room temperature. MP-001 was stained with phospho-specific antibodies p-SRC, p-ERK, and p-AKT for 15 minutes (BD

Biosciences, San Jose, CA and Cell Signaling Technology, Danvers, MA). Jurkat T cells were stained with p-SRC and p-ERK for 15 minutes (BD Biosciences, San Jose, CA). After staining, cells were washed twice with PBS, pelleted at 800 *x g*, and resuspended in PBS for analysis on a 5-laser LSRII (BD Biosciences, San Jose, CA) at the Vanderbilt Flow Cytometry Shared Resource.

Mass Cytometry. Live cells from tumors obtained from the same dissociation conditions as fluorescence flow cytometry analysis were stained for cell surface markers, fixed, permeabilized, and washed in concordance with established dissociation and mass cytometry protocols (Leelatian et al., 2015; Leelatian et al., 2017b). Rhodium intercalator was utilized as a membrane permeability reagent to computationally remove dead cells from the data (Ornatsky et al., 2008) (Fluidigm). Permeabilization with 0.02% Saponin (Millipore, Darmstadt, Germany) in PBS was also included before methanol permeabilization as part of an optimized multi-step protocol to detect SOX2 and MITF. Saponin staining was performed for 30 minutes with anti-SOX2 and MITF antibodies. Cell staining after methanol permeabilization was performed for 15 minutes at room temperature with iridium intercalator and metal-tagged antibodies (Supplemental Table S2). After staining, cells were washed once with PBS, once with deionized water, pelleted at 800 *x g*, resuspended in deionized water, and collected using a CyTOF 1 (Fluidigm) mass cytometer.

Data Analysis. Cytobank was used to store .fcs files and perform data analysis including viSNE gating of major tumor cell populations (Amir el et al., 2013; Kotecha et al., 2010). Statistical analysis of cells gated from samples before and after therapy was performed

using commercial 2D graphing and statistics software GraphPad Prism. Tracking the percent abundance of cells from FlowSOM analysis was performed in STATA 14.2. MEM and FlowSOM analysis were performed in program language R. (Diggins et al., 2018; Diggins et al., 2017; Van Gassen et al., 2015b) (https://mem.vueinnovations.com).

Single Cell Analysis of Human Melanoma Tumors. Viable nucleated cells were gated with total histone H3 and rhodium intercalator for 7 sets of matched tumors (MP-029, MP-031, MP-032, MP-034, MP-055, MP-059, and MP-062) using established methods (Leelatian et al., 2017a; Leelatian et al., 2017b). The patient-specific viSNE analyses were performed with 28 of 32 markers to avoid channels potentially affected by gadolinium MRI contrast agent that the patients received before surgery (Supplementary Table S2). Major populations of cells were identified and quantified using expert gating performed on patient-specific viSNE maps of the pre- post-therapy tumors. (Supplementary Table S3).

To study how cellular heterogeneity was affected by therapy, cells were placed into a workflow that emphasized unsupervised subset identification, characterization, and data visualization with FlowSOM, MEM and viSNE analysis (Diggins et al., 2015; Diggins et al., 2018; Diggins et al., 2017; Van Gassen et al., 2015a). To identify subsets enriched before and after therapy, the viSNE analysis was performed using 17 markers with a variance greater than 0.2 (Supplementary Table S2). FlowSOM cluster analysis was conducted using t-SNE axes as inputs for clustering.

Additional patient's melanoma cells included within Figure 4 were gated as CD45 negative. Cells from these patients were analyzed using shared markers from the optimized

melanoma mass cytometry panel (MP-004, MP-012, MP-019, MP-022, MP-023, MP-040, and MP-054) (Supplementary Table S2).

Statistics. Non-parametric Kolmogorov-Smirnov tests with a significance threshold of p=0.05 were used to compare differences in median mass intensity in Figure 4. Wilcoxon signed rank tests with a significance threshold of p=0.05 were used to compare differences in cellular abundance of cell subsets from matched patient samples in Supplementary Fig. S2 and S3. Statistical tests were performed using commercial 2D graphing and statistics software GraphPad Prism.

Data Availability. Mass cytometry data for this manuscript can accessed via FlowRepository (https://flowrepository.org/).

Results

32-antibody mass cytometry panel and unsupervised computational analysis characterize protein expression in single cells from human melanoma tumors. Human melanoma tumor core biopsies and surgically resected human tumors were dissociated into single cell suspensions (Supplementary Table S1) (Leelatian et al., 2017a). Melanoma tissue samples comprising 14 sample pairs from 7 patients were placed into an analysis workflow to stain cell suspensions with an updated panel that contained 21 additional markers (Supplementary Table S2) (Leelatian et al., 2017a). Mass cytometry data generated from a pre-therapy (Pre-Tx) biopsy of tumor cells from melanoma patient (MP) number 59 (MP-059) and the general data analysis workflow are shown in Figure 1. Pre-Tx samples were from tumors naïve to $BRAF^{V600E}$ inhibitor dabrafenib and MEK inhibitor trametinib and were obtained just prior to the initiation of therapy, which culminated

in surgical resection after four weeks (see Methods). Tumor heterogeneity was visualized using the Cytobank implementation of viSNE/t-SNE (Amir el et al., 2013), which organized cells in a two dimensional graph so that cells with similar protein expression patterns were placed near each other to form islands of phenotypically similar cells (Fig. 1A). Next, marker enrichment modeling (MEM, (Diggins et al., 2018; Diggins et al., 2017) objectively described the enriched protein features of the observed tumor cell types (Fig. 1B). The scale for MEM starts at +10 (most enriched), continues through 0 (no enrichment), and ends at -10 (most excluded). For example, one MEM label was ▲$CD45^{+3}$ $CD49F^{+3}$ $CD19^{+2}$ $MHCI^{+1}$ ▼$SOX10^{-4}$ $S100\beta^{-4}$ $MCAM^{-2}$ $CD44^{-2}$ $BCAT^{-1}$ $\alpha\text{-}SMA^{-1}$ (Fig. 1B, MP-059 Pre-Tx tumor cell population #7), which indicted these cells were relatively enriched for B lineage CD19 and leukocyte CD45 proteins and specifically lacking melanoma cell proteins, including S100β, SOX10, and MCAM (Fig. 1B). This computational workflow using viSNE and MEM reduces bias that can arise in manual gating and characterizes phenotypically unusual cells that may be overlooked or hidden in traditional analyses (Diggins et al., 2015; Diggins et al., 2017; Irish, 2014).

From the protein expression and cellular abundance data in the viSNE and MEM analysis, cells were classified into one of the five major groups (Supplementary Table S3). The most abundant stromal populations were defined as follows: 1) leukocytes ($CD45^{hi}$ and MHC class I), 2) fibroblasts (Thy-1/CD90, α-SMA), 3) endothelial cells (PECAM/CD31 and MHC class I) and 4) epithelial cells (cytokeratin and MHC class I) (Fig. 1B, 1C, and 1D). The panel was also developed to detect epithelial cells, however, epithelial cells were not detected within the tumors of this study (Supplementary Table S3). Cells negative for

markers of stromal cell populations were identified as melanoma cells. Melanoma cells varied in phenotype, however, these cells reliably displayed features consistent with melanoma cell identity including loss of MHC class I or expression of Nestin, SOX10, SOX2, MCAM, or S100β (Fig. 1B, 1C, and 1D).

In addition to the melanoma and tumor cell identity markers in the mass cytometry panel used here (Figure 1), panel design experiments also included analysis of phospho-proteins that had been previously validated for fluorescence and mass cytometry (Irish et al., 2004b; Irish et al., 2010b; Krutzik and Nolan, 2003). For example, phospho-flow analysis of viable post-treatment melanoma tumor cells obtained at following dabrafenib and trametinib revealed essentially no remaining phosphorylation of ERK1/2 or other kinases (Supplementary Fig. S1). Furthermore, stimulation with 3.3 mM peroxide, a positive control for phosphorylation that inhibits protein tyrosine phosphatase activity in leukocytes and melanoma cells (Irish et al., 2010b; Polikowsky et al., 2015), revealed melanoma cell signaling potential was suppressed (Supplementary Fig. S1). Melanoma cells obtained after BRAF and MEK inhibitor treatment were viable according to two standard tests, hemocytometer analysis of trypan blue exclusion and flow cytometer analysis of Alexa fluorophore exclusion (see Methods). These results demonstrated a profound lack of signaling capacity in melanoma cells following BRAF and MEK inhibitor treatment. Because observed signaling responses were effectively suppressed after kinase inhibitor therapy, antibodies detecting phospho-proteins were not included in the optimized melanoma mass cytometry antibody panel (Supplementary Table S2), which was tailored to focus on

features of melanoma cell identity, neural stem and progenitor cells, trafficking, and immune interaction.

BRAF and MEK inhibitor treatment alters tumor phenotype through elimination or expansion of distinct melanoma cell subsets. Analysis of changes in the major stromal cell types from melanoma tumors was compared before and after therapy. The stromal population was quantified from the expert drawn gates of 14 individual viSNE analyses of cells from 7 matched tumor samples obtained Pre-Tx or following surgical resection after BRAF and MEK targeted therapy (Week 4). No significant difference was found between bulk populations of Pre-Tx and Week 4 fibroblasts, endothelial cells, or leukocytes (Supplementary Fig. S2). Previous reports have shown changes in subsets of infiltrating T cells (Frederick et al., 2013). A relative increase in CD3 T cells and cytotoxic $CD8^+$ T cells was observed in tumors following therapy ($p=0.02$ for both, Supplementary Table S3).

To establish a methodology to identify features of cell populations that escaped targeted therapy, Pre-Tx and Week 4 tumor cells from MP-059 were analyzed simultaneously in a new viSNE map (Fig. 2A). Features for viSNE analysis were selected based on a variance of 0.2 or greater across 14 melanoma tissue samples (Supplementary Table S2) following established methods (Irish et al., 2004b; Irish et al., 2010b). Cells from this viSNE analysis were next characterized by MEM to quantify feature enrichment and phenotypic stability over time during treatment (Fig. 2B).

Analysis with viSNE and MEM indicated Pre-Tx cells were enriched for neural crest stem cell markers Nestin, SOX10, SOX2, CD49F, and melanoma diagnostic biomarker S100β (Ordonez, 2014). In contrast, Week 4 cells lost Nestin and CD49F expression and

expressed other markers of neural crest identity including NGFR, SOX10, and SOX2. Furthermore, Week 4 cells specifically lacked immune interaction protein MHC I (Fig. 2C) (Garcia-Lora et al., 2003). The overall change in tumor phenotype was calculated as change (Δ) in MEM (ΔMEM) by subtracting Week 4 MEM enrichment scores from those measure in the Pre-Tx sample (Diggins et al., 2018). ΔMEM analysis revealed Nestin, a neural cell filament (Park et al., 2010), and CD49F, a stem-cell niche associated integrin (Krebsbach and Villa-Diaz, 2017), were the melanoma cell features whose enrichment changed the most from Pre-Tx to Week (Fig. 3). These results provided a quantitative workflow to characterize and track changes in tumor heterogeneity.

Combined viSNE analysis of melanoma tumors identifies patient-specific changes in tumor phenotype following BRAF and MEK inhibitor treatment. To systematically identify subset phenotypes that escape therapy, matched tumors were placed into an analysis workflow that identifies and characterizes subset phenotypes from a sequential viSNE, FlowSOM, and MEM analysis (Supplementary Fig. S4A). Using this unsupervised approach minimizes the influence of human bias between users and could reveal information about populations that may be overlooked with biaxial gating alone. Equal numbers of melanoma cells from 7 pairs of samples Pre-Tx and Week 4 melanoma tumors were next analyzed in one new viSNE map (Fig. 3). Analysis of the pre-therapy samples within one viSNE map made it apparent that melanoma cell phenotypes were largely distinct for each patient Pre-Tx (Fig. 3A). Some tumors were relatively homogenous in phenotype (Fig. 3A, MP-029, MP-032, and MP-062), whereas other tumors contained multiple phenotypically distinct cell types that formed well-separated ‘islands’ in the

common viSNE map (Fig. 3A, MP-031, MP-034, MP-055, and MP-059). These results were observed when heat plots of cell density for each sample were overlaid on a black and white contour plot showing the density of all cells. Analysis of Week 4 cells for each patient revealed the emergence of subset phenotypes that did not exist before therapy (Fig. 3A, MP-029, MP-032, MP-034, and MP-059), or little change from the pre-existing phenotype (Fig. 3A, MP-031, MP-055, and MP-062).

An unsupervised analysis approach was next used to identify melanoma cell subsets that evaded therapy. FlowSOM, a machine learning tool based on self-organizing maps (Van Gassen et al., 2015b), was used to automatically identify cell subsets within the common viSNE map of Pre-Tx and Week 4 (Fig. 3B). Manual analysis by experts was conducted prior to FlowSOM analysis and revealed approximate 30 phenotypically distinct cell types within the combined set of Pre-Tx and Week 4 melanoma tumors. FlowSOM analysis was used to automatically identify 30 phenotypically distinct cell subsets in Pre-Tx and Week 4 tumor samples (Fig. 3B) and then percent abundance for each cell subset was quantified (Fig. 3C, Supplementary Table S4).

Cell subsets were categorized into three groups by comparing Pre-Tx and Week 4 subset abundance (Supplementary Figure S4). An intra-tumoral cell subset was considered to have regressed when >75% of its cells were observed Pre-Tx, meaning that it decreased in abundance by at least 50% on treatment. In contrast, a subset was considered to have emerged when >75% of its cells were seen at Week 4. All other subsets demonstrated less than 50% change from Pre-Tx to Week 4 and were considered to have persisted (Supplementary Figure S4). Thus, the terms *regressing*, *persisting*, and *emerging* used

here refer to changes in the abundance of cells within a single tumor and are not comparable to overall clinical assessments of patient responses to treatment. Once subsets were categorized, MEM was used to identify common phenotypic signatures of each melanoma cell group. Compared to the other subsets, regressing melanoma cell subsets (Fig 3C, e.g. subsets 24, 27, 1, and 26) were enriched for neural crest stem cell proteins Nestin, CD49F, SOX2, and SOX10, melanocyte biomarker S100β, and immune interaction protein MHC I (Supplementary Table S4 and Supplementary Fig. S4). In contrast, the emerging melanoma cell subsets especially lacked Nestin and CD49F (Supplementary Table S4 and Supplementary Fig. S4). The phenotypes of the persisting cells were more heterogeneous, and no proteins were especially enriched in these cells (e.g., Supplementary Figure S4, SOX2, SOX10, and CD49F). However, persisting cells contrasted with both regressing and emerging cell subsets, in that they most commonly lacked MHC class I protein expression (Supplementary Figure S4 and Supplementary Table S4).

Significant loss of Nestin protein expression was observed in melanoma cells at Week 4 following dabrafenib and trametinib. Since the melanoma cell subsets with the greatest changes in abundance on treatment also shared similar phenotypes, median protein expression was next analyzed in aggregate comparisons of all Pre-Tx cells to all Week 4 cells. Unpaired comparisons of 4 melanoma cell lines, 14 Pre-Tx samples, and 11 Week 4 samples showed that median Nestin protein expression was significantly lower in Week 4 samples than in Pre-Tx samples ($p=0.04$, Fig. 4A). Melanoma cell lines generally expressed high levels of Nestin protein (MeWo, A2058, and WM115), although SKMEL28

cells were an exception and only moderately expressed Nestin. CD49F, MCAM, MHC II, and CCR4 were also expressed in Pre-Tx melanoma cells, but no statistically significant difference in median protein expression was observed between Pre-Tx and Week 4 (Fig. 4). Paired comparison of the 21 most highly expressed melanoma cell proteins in Pre-Tx and Week 4 samples also showed significant decreases in median expression of Nestin, MHC class I, CD49F, and EGFR protein (Supplementary Figure S6). Features previously associated with response (MITF) or resistance (AXL, EGFR) were expressed at low levels in tumor samples and did not change significantly over time (Supplementary Fig S6).

Parallel mass cytometry and immunohistochemical analysis show loss of Nestin protein expression in melanoma cells at Week 4 following dabrafenib and trametinib. Standard formalin fixed, paraffin-embedded archival tissue blocks of the same tumor specimens studied by mass cytometry were available for four tumors. However, images from immunohistochemistry (IHC) staining of tissue will include all cells, whereas the mass cytometry analyses here used gating to analyze proteins specifically within melanoma cells. To compare mass cytometry findings to traditional IHC, mass cytometry data were re-analyzed to calculate the percentage of Nestin expressing cells within all live tumor cells (Fig. 5). Next, hematoxylin counterstain and expression of Nestin, SOX10, and S100β were evaluated by IHC in subcellular sections (<10 μm) of tissue microarrays (TMAs) from four tumors also analyzed by mass cytometry. A comparable loss of Nestin expression between Pre-Tx and Week 4 was apparent in both mass cytometry and IHC (Fig. 5C). Furthermore, Week 4 melanoma cell abundance and Nestin heterogeneity were also observed to be comparable in both mass cytometry and IHC in all TMAs (Fig. 5C, SOX10

and S100β expression in Nestin negative cells). While Nestin was most abundant Pre-Tx, different intensities in Nestin expression among neighboring melanoma cells also provided another indicator of intra-tumor cellular heterogeneity (e.g. Patient 22, Fig. 5C and Supplementary Fig. S7).

To investigate these results further, Kaplan-Meier statistical analysis was performed on 11 patient sets, which revealed no significant association between Nestin or CD49F expression and outcome (Supplementary Fig. S8). Analysis of tumor size suggested that low expression of Nestin and CD49F might be more common in larger tumors (Supplementary Fig. S9). Additional analysis of publicly available single-cell RNA-Seq data from therapy naïve and relapse samples revealed increased Nestin transcript expression at the time of relapse in some samples (Supplementary Fig. S10) (Tirosh et al., 2016). Taken together with the protein measurements made at Week 4 here, these findings suggest that melanoma cells lacking Nestin protein after treatment may be capable of repopulating the Nestin-expressing melanoma cell population by the time of relapse.

Discussion

These results reveal the loss of Nestin-expressing tumor cells, a hallmark of aggressive, metastatic disease, immediately after targeted BRAFV600E and MEK inhibitor therapy. Nestin expression has previously been associated with advanced stage melanoma, stem-ness, and dissemination of circulating melanoma cells (Akiyama et al., 2013; Fusi et al., 2010; Ladstein et al., 2014). However, Nestin negative cells persisted and emerged after therapy, and these cells maintained other features of neural crest identity, including SOX2, CD49F, and SOX10 expression (Simoes-Costa and Bronner, 2015). To date, the depletion

of Nestin has been shown to produce invasive phenotypes in melanoma, however, a direct link between MAPK inhibition and melanoma phenotype has not been previously established (Lee et al., 2014). Three central elements of the approach here were the focus on single cell measurements of core cell identity proteins, comparison of cells from one tumor over time, and unsupervised computational analysis. This approach was especially useful in revealing phenotypically distinct populations of melanoma cells present in resected Week 4 tumor samples. The melanoma cells observed at Week 4 contrasted significantly with the cells observed in the same tumors prior to the start of BRAF and MEK inhibitor treatment (Fig. 3, Fig. 4, and Supplementary Fig. 4) and with cells characterized at the time of relapse in other studies (Hugo et al., 2015; Tirosh et al., 2016). Thus, while relapse is likely driven by diverse mechanisms among patients, the populations of cells initially involved in evading a single treatment may have common, targetable features.

While the selection of stem-like subsets has been implicated as the primary means of relapse in other cancers, cellular plasticity and therapy-induced reprogramming could be responsible for the shift in phenotype in melanoma (Holzel et al., 2013). Neural cell plasticity and therapy-induced reprogramming have previously been observed in models of melanoma, including the emergence of melanoma tumors that display a dependence on MAPK inhibition to support tumor growth (Das Thakur et al., 2013; Handoko et al., 2013; Sun et al., 2014). IHC data published previously for tumors from patients on this trial showed a decrease in Ki67 positive cells to an average of 2.9% at Week 4 (Johnson et al., 2015). This result indicates that proliferation is largely absent by Week 4 and suggests it is unlikely that the changes in tumor composition observed here can be explained solely by

the growth of an intrinsically-resistant subset. Furthermore, analysis of therapy naïve and relapse samples suggests that the Pre-Tx cellular composition of the tumor recovers after the end of targeted therapy and prior to the time of relapse (Tirosh et al., 2016).

While the increase in T cell infiltration suggested a robust response to therapy, melanoma cells were not completely eradicated (Frederick et al., 2013). Melanoma subsets observed after therapy were either emerging novel subsets not present before therapy or persisting MHC class I negative cells. Lack of MHC class I expression has been implicated in impaired immune surveillance (Garcia-Lora et al., 2003). It was also apparent that individual melanoma cells almost never co-expressed Nestin and PD-L1 (N = 7 pairs, Supplementary Figure 5). At the sample level, low median PD-L1 expression was seen on some melanoma cell subsets (e.g. Subsets 1, 6, 11, Supplementary Figure S4). In these subsets of PD-L1 expressing melanoma cells, a deficit in Nestin protein expression was observed. Furthermore, in subsets where median Nestin expression was higher (e.g. subsets 27, 26, and 24), median PD-L1 expression was low to zero. Taken together, loss of Nestin might represent a transient identity influenced by therapy, and loss or a sustained lack of MHC proteins coupled with PD-L1 expression could facilitate evasion from the immune system to enable a broader range of genomic and non-genomic alterations to arise at relapse (Hugo et al., 2015; Johnson et al., 2014). Targeting antitumor immunity after this therapeutic window could be a favorable period to kill residual cells before tolerance develops into clinical resistance.

The results presented here introduce a longitudinal mass cytometry study of human melanoma tumors and establish a reference for future longitudinal solid tumor studies. The

measurement of 32 markers of cell identity, trafficking, and immune interaction was especially valuable in clarifying the identity of melanoma cells which displayed unexpected phenotypes, such as the abnormal neural crest phenotype that persisted following treatment. The observed loss of Nestin and persistence of MHC class I negative subsets in patients could have negative consequences for other targeted therapies and immunotherapy. With the range of therapeutic options for melanoma rapidly growing, combining clinical studies with single cell analysis could identify novel features to track clinical responses and reveal unexpected consequences of treatment.

Author contributions

All authors discussed data visualization, contributed intellectually to the manuscript, and approved the final manuscript. M.C.K., J.M.I., D.B.D., J.A.S., and K.B.D. initially designed clinical research. M.C.K. and J.A.S. designed the clinical trial, consented and enrolled patients, and M.C.K. collected tissue for research. D.B.D., J.M.I., A.R.G., and M.C.K. designed mass cytometry panels. D.B.D. created and characterized custom conjugated mass cytometry antibodies. D.B.D., A.R.G., C.E.R. collected, normalized, and annotated mass cytometry data. D.B.D., K.E.D., A.R.G., J.S.G., and J.M.I. contributed statistical and computational analyses of mass cytometry. D.B.D., K.B.D., M.C.K., and J.M.I. contributed to histology experiments with tissue microarrays. D.B.D., A.R.G., J.S.G, and J.M.I. prepared figures. D.B.D., A.R.G., and J.M.I. drafted the manuscript.

Acknowledgments

This study was supported by NIH/NCI T32 CA009592 (D.B.D), R25 GM062459 (D.B.D), R25 CA136440 (K.E.D.), F31 CA199993 (A.R.G.), R00 CA143231 (J.M.I.), the Vanderbilt-

Ingram Cancer Center (VICC, P30 CA68485), Vanderbilt Medical Scholars (J.S.G) and VICC Ambassadors.

Figure Legends

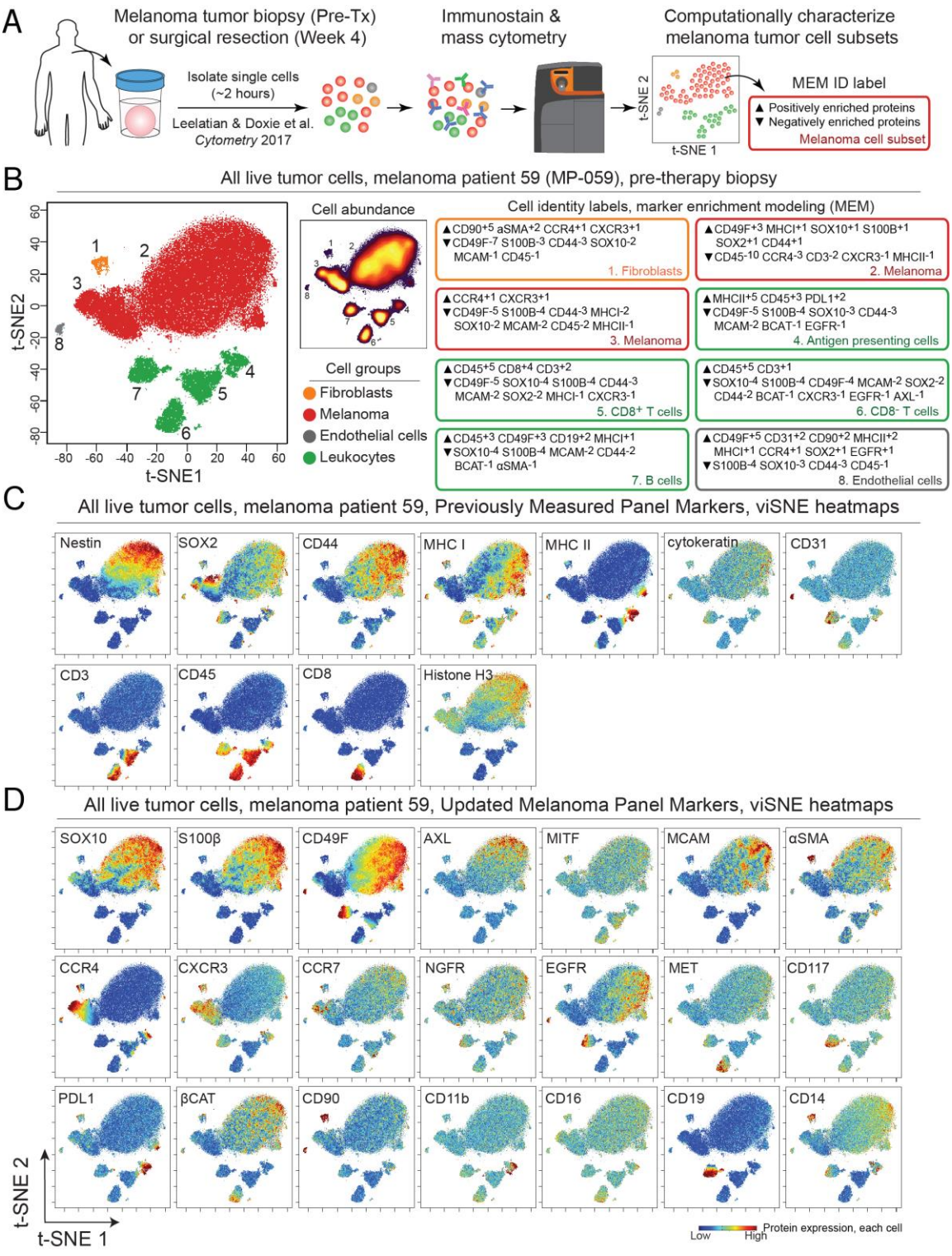

Figure 5-1. A 32-antibody mass cytometry panel and unsupervised computational analysis characterize protein expression in single cells from human melanoma tumors. (A) An overview of the analysis approach is shown. Melanoma tumor samples from patients enrolled in Phase II interventional study NCT01701037 were obtained as a biopsy prior to neoadjuvant therapy (Pre-Tx) using dabrafenib and trametinib therapy or from surgical resection after 4 weeks of therapy (Week 4). Viable single cells were isolated following established protocols (Leelatian et al., 2016; Leelatian et al., 2017b), analyzed by mass cytometry, and characterized using a modular, unsupervised computational workflow created for melanoma from dimensionality reduction tool t-SNE/viSNE (Amir el et al., 2013), clustering tool FlowSOM (Van Gassen et al., 2015a), and cell subset identification and protein enrichment characterization with MEM (Diggins et al., 2017). In (B), viSNE plots and MEM labels used to identify and characterize cells from melanoma tumors are shown. viSNE plots display all live cells from one Pre-Tx melanoma tumor (MP-059) arranged according to protein expression and shaded based on cell type (B, left) or abundance (B, middle, density plot). MEM labels quantified protein enrichment (▲ up to +10) or specific absence (▼ down to -10) in the indicated tumor cell subset. For example, melanoma cells in subset 2 had the label ▲CD49F^{+3} MHCI^{+1} SOX10^{+1} S100β^{+1} SOX2^{+1} CD44^{+1} ▼CD45^{-10} CCR4^{-3} CD3^{-2} CXCR3^{-1} MHC II^{-1}, which identified this population as melanoma cells based on enrichment of SOX2, S100β, and SOX10 proteins and a lack of MHC II protein expression. In (C) and (D), viSNE plots show the same cells from (B) but display per-cell expression of the indicated protein on a rainbow scale where red indicates high expression and blue indicates low expression. Antibodies for protein targets listed in (C) comprised a validated backbone melanoma cell identity panel (Leelatian et al., 2016). (D) An additional 21 proteins were added to the melanoma mass cytometry panel here to characterize features of melanoma cell subsets.

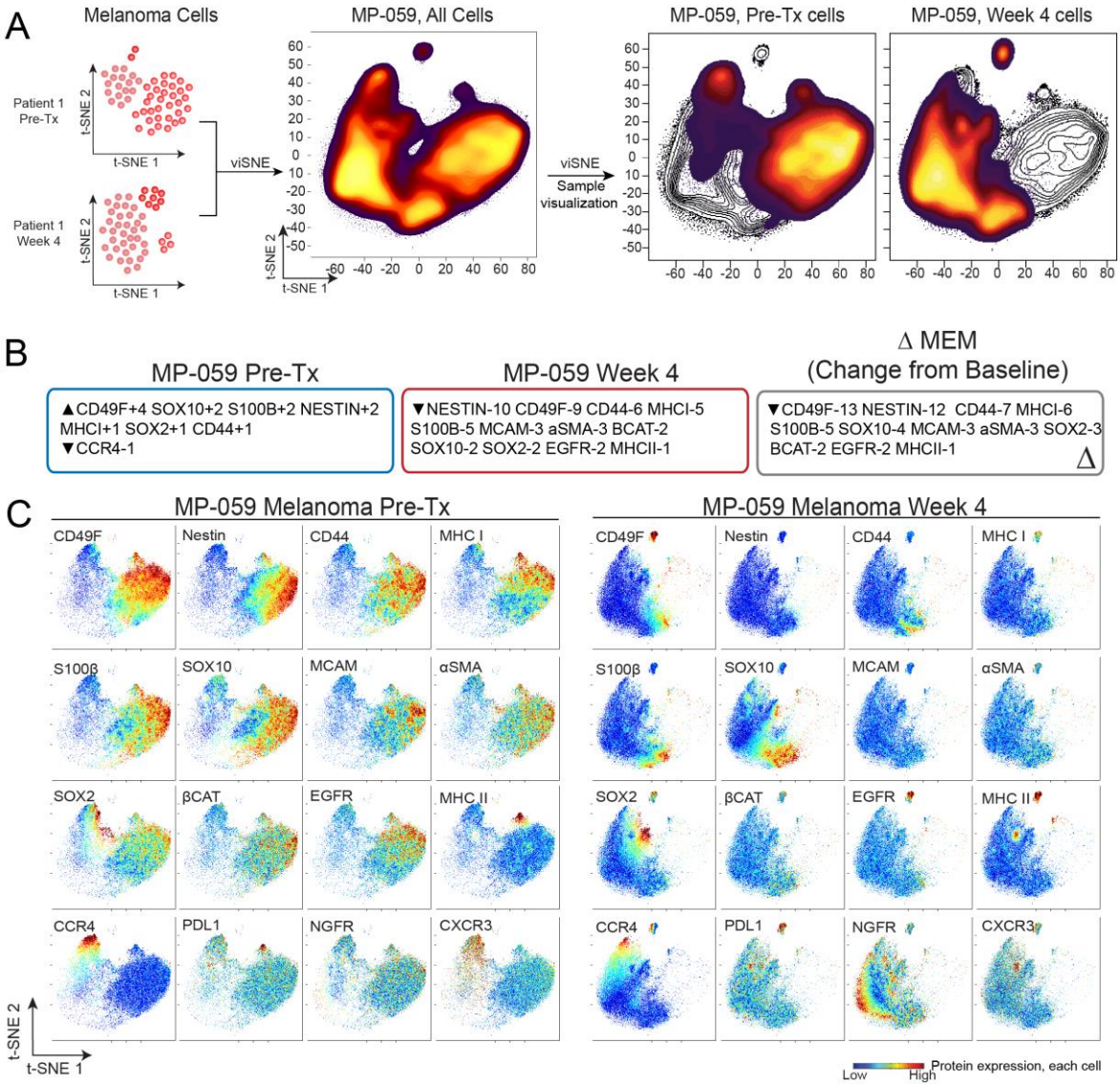

Figure 5-2 BRAF and MEK inhibitor treatment alters tumor phenotype through elimination or expansion of distinct melanoma cell subsets in MP-059. (A) viSNE density plots show phenotypic change over time for a single melanoma tumor (MP-059). Pre-Tx and Week 4 melanoma cells were computationally separated from other stromal cell types as in Figure 1 and combined for a new viSNE analysis. (B) MEM labels quantify enrichment of 17 of 32 measured proteins in Pre-Tx and Week 4 melanoma cells from one tumor (MP-059). Features for MEM analysis were selected with a variance > 0.2 from 7 pairs of Pre-Tx and Week 4 tumors. Only significantly enriched proteins are shown. The overall change in tumor phenotype (ΔMEM) was calculated by subtracting Week 4 MEM enrichment scores from those measured in the Pre-Tx sample. (C) viSNE plots show protein expression in cells (heat) from the combined viSNE analysis of MP-059 melanoma cells from Pre-Tx and Week 4. The 16 proteins with the greatest difference in expression across melanoma cells are shown.

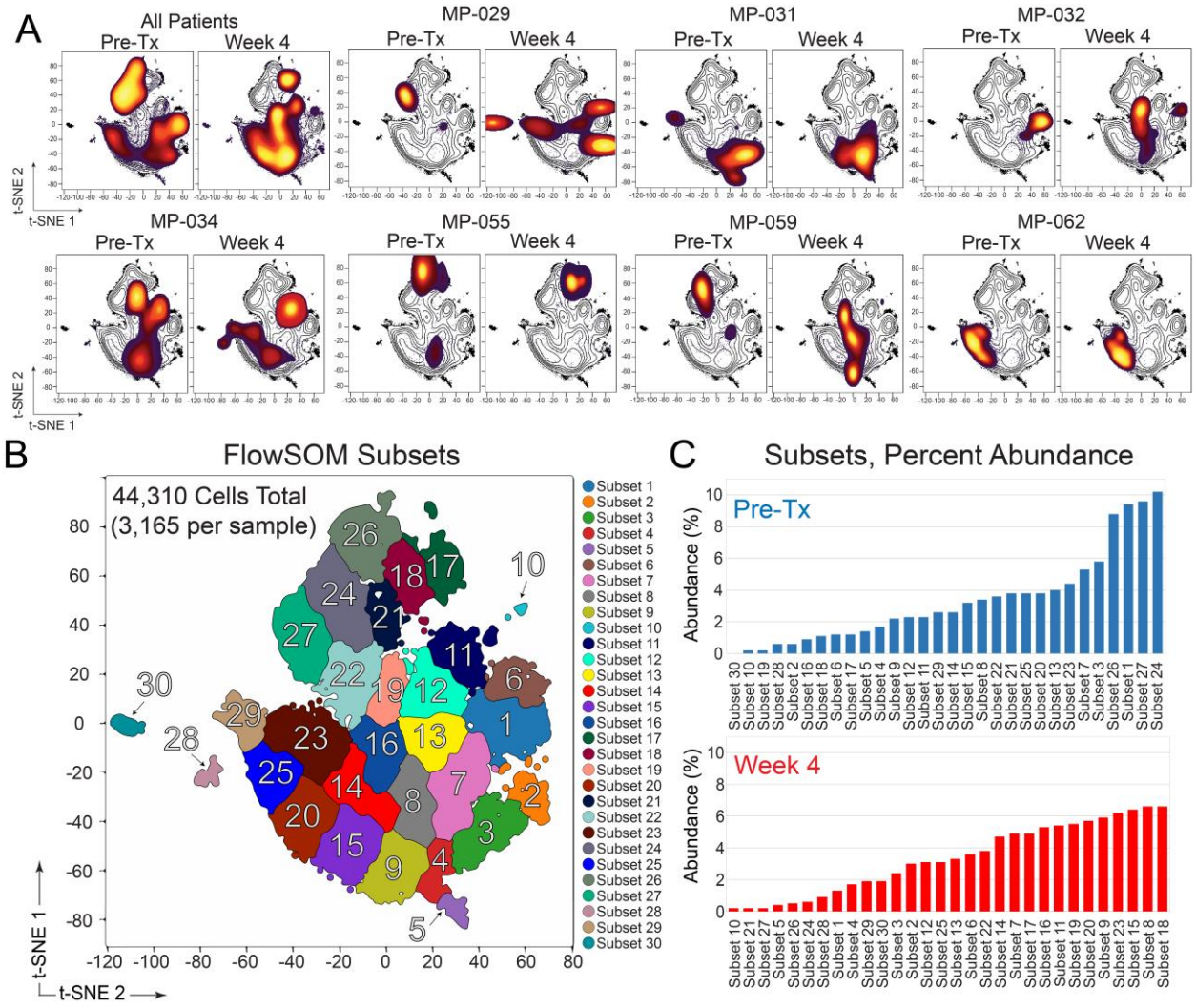

Figure 5-3 Combined viSNE analysis of melanoma tumors identifies patient specific changes in tumor phenotype following BRAF and MEK inhibitor treatment. (A) viSNE density plots show phenotype and abundance of melanoma cells from paired samples of Pre-Tx and Week 4 tumors (N = 7 tumors). A combination viSNE density plot (upper left) shows all patients combined in two plots at Pre-Tx and Week 4. (B) FlowSOM cluster analysis of all patients (Pre-tx and Week 4 combined, as in A) automatically identified phenotypically distinct subsets. (C) Abundance (% of Pre-Tx or % of Week 4 cells) for all subsets identified by FlowSOM is shown, organized from least to most common in Pre-Tx or Week 4 melanoma tumors. Subset labels from (B) and (C) are the same and additional information on patients and subset phenotypes is shown in Supplementary Table S4 and Supplementary Figure S5.

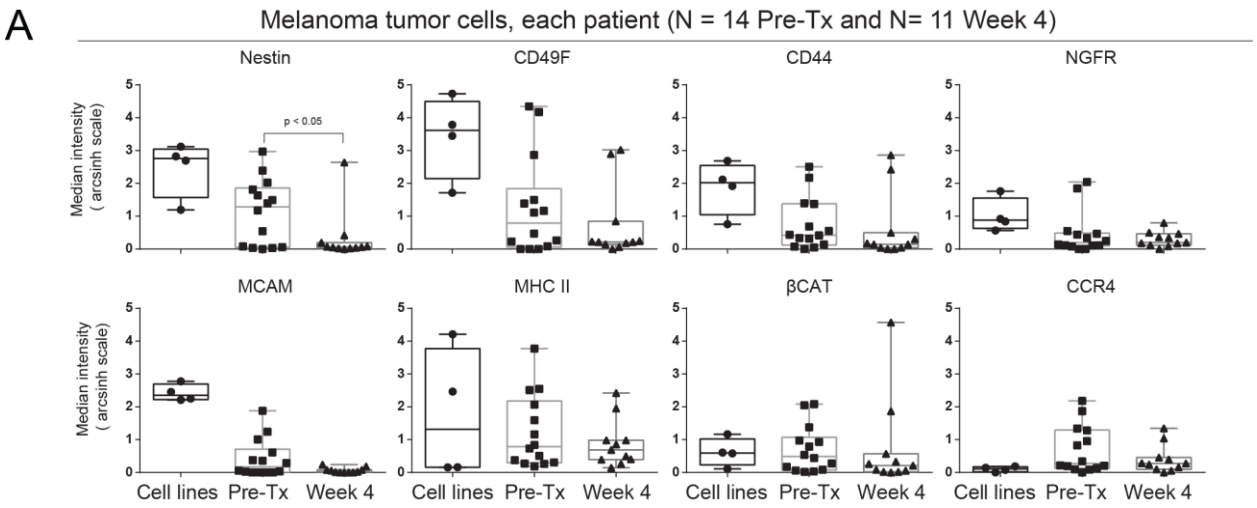

Figure 5-4 Significant loss of Nestin protein expression was observed in melanoma cells at Week 4 following dabrafenib and trametinib. (A) Box and whisker plots of mass cytometry data show the median intensity of 8 proteins for melanoma cell lines (A2058, MeWo, WM155, and SKMEL28), Pre-Tx therapy naïve melanoma tumors, and post-therapy Week 4 melanoma tumors. Melanoma tumor cells were gated as $CD45^{lo/-}$.

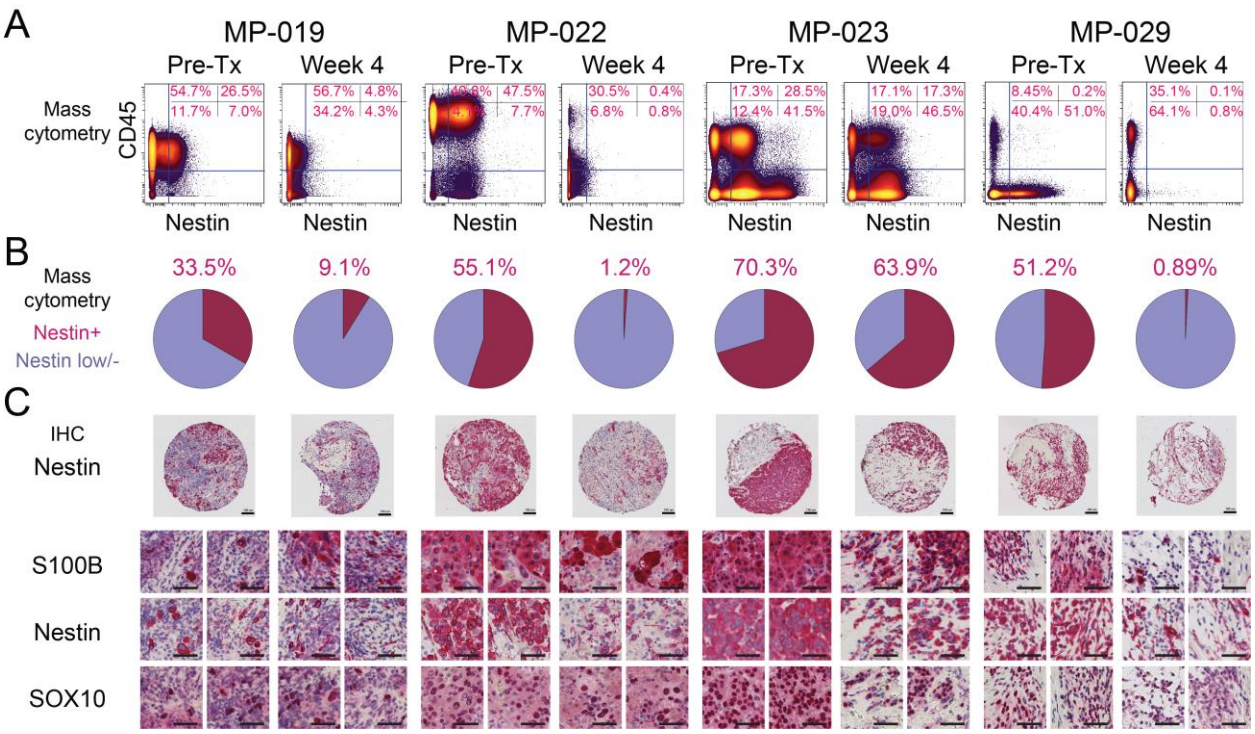

Figure 5-5 Parallel mass cytometry and immunohistochemical analysis show loss of Nestin protein expression in melanoma cells at Week 4 following dabrafenib and trametinib. (A) To compare mass cytometry findings to traditional IHC, which includes all tumor cells in an image, mass cytometry data were re-gated to include all live cells. Traditional biaxial plots of mass cytometry data shown CD45 protein expression (leukocytes) versus Nestin protein expression Pre-Tx and at Week 4 following treatment for four tumors. (B) Pie graphs show the percentage of cells expressing Nestin observed by mass cytometry in each tumor Pre-Tx and at Week 4. (C) Paraffin-embedded core biopsies from tissue microarrays of the same tumors as in (A) were analyzed by immunohistochemistry for Nestin protein and, in in higher magnification views, for Nestin and traditional histology markers of melanoma, S100β and SOX10. Serial slices are shown for two fields of view per TMA per time point. Scale bars indicate 100 μm in all images.

Supplementary Figure Legends

Table 5-1 (S1) Patient Clinical Features

Supplementary Table S1. Patient Clinical Features

Patient	Age	Sex	Histology Subtype	Biopsy[±] Site	Primary Site	SNaPshot genotype*	Prior treatment[§]	Status	Relapse	Therapy After Relapse	Trial Code
MP-001	N/A	F	N/A	LN	N/A	$BRAF^{V600E}$	GSK1120212 GSK2118436	N/A		N/A	----------
MP-004	N/A	M	N/A	LN	N/A	$BRAF^{V600E}$	None	N/A		N/A	----------
MP-012	N/A	M	N/A	LN	N/A	$BRAF^{V600E}$	None	N/A		N/A	----------
MP-019	43	M	N/A	Axillary LN	N/A	$BRAF^{V600E}$	None	Deceased	✓	Radiation and Dabrafenib	1263-001
MP-022	53	F	Nodular	Inguinal LN	Thigh	$BRAF^{V600E}$	None	Disease Free		None	1263-003
MP-023	66	M	Not Specified	Neck LN	Scalp	$BRAF^{V600E}$	None	Deceased	✓	Pembrolizumab	1263-004
MP-029[†]	37	F	Nodular	Axillary Ln	Back	$BRAF^{V600E}$	None	Deceased	✓	Ipilimumab	1263-005
MP-031[†]	24	F	Not Specified	Axillary LN	Chest	$BRAF^{V600E}$	None	Disease Free		None	1263-006
MP-032[†]	43	F	Nodular	Chest	Chest	$BRAF^{V600E}$	None	Deceased	✓	None	1263-007
MP-034[†]	59	F	SSM	Groin, Thigh	Leg	$BRAF^{V600E}$	None	Deceased	✓	Wide Local Excision	1263-008
MP-040	N/A	M	N/A	LN	N/A	$BRAF^{V600E}$	None	N/A		N/A	----------
MP-054	62	M	Nodular	Upper Back	Neck	$BRAF^{V600E}$	None	Disease Free		None	1263-010
MP-055[†]	50	F	SSM	Neck, Scalp	Scalp	$BRAF^{V600E}$	None	Deceased	✓	None	1263-011
MP-059[†]	F	72	Nodular	Thigh, in transit disease	Thigh	$BRAF^{V600E}$	None	Disease Free		None	1263-012
MP-062[†]	M	76	Not Specified	Scalp	Scalp	$BRAF^{V600E}$	None	Deceased	✓	Radiation	1263-013

[±]All patients studied in this manuscript presented with either several subcutaneous legions or distal metastasis. All tumors in the study are presumed to have arisen as cutaneous legions because no primary disease was present in mucosal epithelium or retina. * SNaPshot genotyping tests 48 mutations in *NRAS, BRAF, KIT, CTNNB1, GNA11, and GNAQ* (Lovly C et al., *PLoS ONE* 2012;7(4):e35309.) [§] Treatment ≤1 month prior refers to any treatment that occurred less than 1 month before biopsy Patients with trial codes 1263-XXXX were offered BRAFi GSK2118436 for 2 weeks immediately following baseline biopsy. Patients also received combination BRAFi + MEKi (GSK1120212 and GSK2118436) for 2 weeks immediately following BRAFi. At the end of one month the patients' tumors were surgically resected [†]Patients analyzed with a 32 marker mass cytometry panel (Table S2) and included in Figures 3 and 4.

Table 5-2 (S2) Melanoma mass cytometry panel

Supplementary Table S2. Melanoma mass cytometry panel

Target	Mass	Clone	Dilution	Vendor	Staining			viSNE Analysis	
					Live	Saponin	MeOH	All Cells	Cancer
CD271*	139	ME20.4	2 µg/mL	BioLegend	✓			+	+
HLA-ABC	141	W3-32	1:200	Fluidigm	✓			+	+
CD19	142	HIB19	1:200	Fluidigm	✓			+	
CD117	143	104D2	1:100	Fluidigm	✓			+	
CD11b	144	ICRF44	1:200	Fluidigm	✓			+	
CD31	145	WM59	1:200	Fluidigm			✓	+	
CD8a	146	RPA-T8	1:200	Fluidigm	✓			+	
β-Catenin	147	D10A8	1:100	Fluidigm			✓	+	+
CD16	148	3G8	1:200	Fluidigm	✓			+	
CCR4	149	205410	1:100	Fluidigm	✓			+	+
SOX10*	150	A-2	4 ug/ml	Santa Cruz			✓	+	+
CD146*	151	SHM-57	2 µg/mL	Biolegend	✓			+	+
S100B*	153	19-S100B	1 µg/mL	BD			✓	+	+
CD45	154	HI30	1:400	Fluidigm			✓	+	
CXCR3	156	G02587	1:200	Fluidigm	✓				
CD90	159	5E10	1:200	Fluidigm	✓			+	+
CD14	160	M5E2	1:100	Fluidigm	✓				
Cytokeratin*	161	C-11	0.5 µg/mL	Abcam			✓	+	
c-MET*	162	L6E7	1 µg/mL	CST	✓			+	
SOX2*	163	O30-678	1 µg/mL	BD		✓		+	+
CD49F	164	G0H3	1:200	Fluidigm	✓			+	+
EGFR*	165	AY13	1 µg/mL	BioLegend	✓			+	+
CD44	166	BJ18	1:200	Fluidigm			✓	+	+
CCR7	167	G043H7	1:200	Fluidigm	✓			+	
Nestin*	168	10C2	2 µg/mL	BioLegend			✓	+	+
AXL*	169	C89E7	4 µg/mL	Cell Signaling			✓	+	
CD3	170	SP34-2	1:100	Fluidigm	✓				
MITF*	171	D5	4 µg/mL	Dako		✓		+	+
αSMA*	173	Not Listed	0.5 µg/mL	Abcam			✓	+	+
HLA-DR	174	L243	1:200	Fluidigm	✓			+	+
PD-L1	175	29E.2A3	1:100	Fluidigm	✓			+	+
Histone H3	176	D1H2	1:200	Fluidigm			✓		

***Denotes custom conjugates made from labeling kits.**

Table 5-3 (S3) Percent Cell Abundance

Supplementary Table S3. Percent Cell Subset Abundance*

Melanoma patient samples	MP-029		MP-031		MP-032		MP-034		MP-055		MP-059		MP-062	
	Pre-Tx	Week 4	Pre-Tx	Week 4	Pre-Tx	Week 4	Pre-Tx	Week 4	Pre-Tx	Week 4	Pre-Tx	Week 4	Pre-Tx	Week 4
Melanoma	87.0	52.7	3.9	23.9	67.3	54.4	74.1	81.6	41.8	20.7	78.3	75.9	69.2	40.8
Leukocyte	9.10	33.9	92.8	60.2	26.1	37.6	11.4	12.7	53.3	78.5	75.9	19.9	40.8	13.4
Fibroblast	1.30	2.80	0	0.90	0	1.40	0.50	0	1.90	0	1.30	4.20	0	0
Endothelial	0.70	9.60	0.4	1.2	0	0.6	0.20	1.10	0	0.60	0.60	0	0.61	0
Epithelial	0	0	0	0	0	0	0	0	0	0	0	0	0	0
CD3 T cells	5.50	27.6	31.3	32.9	8.50	25.5	5.4	10.2	20.3	43.2	11.1	13.8	3.2	3.40
CD8 T cells	1.70	11.7	9.70	13.0	4.50	15.2	2.0	4.40	10.6	12.3	4.9	5.60	1.70	1.70
B cells	0.38	1.78	56.31	21.0	0.84	8.57	0.41	1.03	28.6	32.4	5.02	2.57	0.56	0.35
APC's	2.73	1.59	2.08	2.63	12.67	1.44	0.90	0.71	3.22	1.83	5.02	3.14	0	0

***includes all patients characterized by optimized mass cytometry panel (Supplementary Table S2)**

Table 5-4 (S4) Melanoma subsets total abundance, Week 4 vs Pre-Tx

Supplementary Table S4 - Melanoma subset total abundance, Week 4 vs. Pre-Tx abundance, and phenotype						
No.	Type	Total (%)	Pre-Tx (%)	Week 4 (%)	Enriched proteins §	
24	Regresser	5.4%	94.6%	5.4%	▲CD49+6 SOX10+3 S100B+3 CD44+3 NESTIN+3 MHCI+2	▼MHCII−2 CCR4−1
1	Regresser	5.4%	87.7%	12.3%	▲ MHCII+3 MHCI+2 CCR4+2 S100B+2 CD44+2 aSMA+1	▼CD49−5 SOX10−2 SOX2−2
27	Regresser	4.9%	97.9%	2.1%	▲NESTIN+4 S100B+3 CD49+3 MHCI+2 MCAM+2 CD44+2	▼MHCII−2 CCR4−1
26	Regresser	4.6%	94.7%	5.3%	▲CD49+9 MHCI+5 S100B+5 CD44+5 MCAM+4 SOX2+3 NESTIN+3 SOX10+2	▼MHCII−2 CCR4−1
21	Regresser	2.0%	94.7%	5.3%	▲CD49+7 SOX10+4 MHCI+3 S100B+3 SOX2+3 CD44+3 BCAT+2 MCAM+2 aSMA+2	-
5	Regresser	0.9%	78.5%	21.5%	▲EGFR+5 CD44+2	▼SOX2−5 CD49−5 MHCI−3 SOX10−3 S100B−3 MHCII−2
23	Persister	5.3%	41.6%	58.4%	▲SOX2+3 MHCII+1	▼CD49−4 MHCI−3 SOX10−3 S100B−3 CD44−3 aSMA−2
7	Persister	5.1%	52.1%	47.9%	▲MHCII+2	▼CD49−6 SOX2−5 S100B−4 SOX10−3 CD44−3 MHCI−2
8	Persister	5.0%	33.8%	66.2%	-	▼CD49−6 SOX2−5 MHCI−4 S100B−4 CD44−4 SOX10−3 aSMA−2 MHCII−2
15	Persister	4.8%	33.2%	66.8%	-	▼CD49−6 MHCI−4 S100B−4 SOX2−4 CD44−4 SOX10−3 aSMA−2 MHCII−2
20	Persister	4.7%	39.9%	60.1%	▲SOX2+5	▼CD49−6 MHCI−4 S100B−4 CD44−4 SOX10−3 MHCII−2
3	Persister	4.1%	71.1%	28.9%	▲CD90+1	▼CD49−6 SOX2−5 S100B−4 MHCI−3 SOX10−3 CD44−3 aSMA−2 MHCII−1
9	Persister	4.1%	27.5%	72.5%	-	▼CD49−6 SOX2−5 MHCI−4 S100B−4 SOX10−3 CD44−3 aSMA−2 MHCII−2
11	Persister	3.8%	29.4%	70.6%	▲CD49+4 aSMA+3 S100B+2 CD44+2 MHCII+2 SOX10+1	▼MHCI−2
22	Persister	3.7%	49.2%	50.8%	▲SOX10+2 S100B+2 CD49+2 MHCI+1 CD44+1	▼SOX2−2 MHCII−2
14	Persister	3.7%	35.3%	64.7%	▲MHCII+2	▼ CD49−6 MHCI−4 S100B−4 SOX10−3 SOX2−3 CD44−3
13	Persister	3.6%	54.7%	45.3%	▲CCR4+3 SOX10+1 SOX2+1	▼CD49−4 S100B−3 CD44−3 MHCII−2 MHCI−1
25	Persister	3.4%	54.9%	45.1%	▲SOX2+5	▼CD49−5 MHCI−4 SOX10−3 S100B−3 CD44−3 MHCII−2
12	Persister	2.7%	42.5%	57.5%		
6	Persister	2.4%	25.4%	74.6%	▲MHCII+6 SOX10+2 MHCI+1	▼CD49−4 NGFR−1
29	Persister	2.2%	57.5%	42.5%	▲SOX2+7 CD49+3	▼S100B−3 CD44−3 SOX10−2
4	Persister	1.7%	49.6%	50.4%	▲EGFR+1	▼ CD49−6 SOX2−5 MHCI−4 S100B−4 SOX10−3 CD44−3 aSMA−2 MHCII−2
28	Persister	0.7%	39.1%	60.9%	▲aSMA+10 MHCII+3	▼CD49−5 MHCI−4 SOX10−3 S100B−3 CD44−3 SOX2−2
10	Persister	0.2%	44.9%	55.1%	▲SOX10+10 CD44+3 MCAM+2	▼SOX2−5 CD49−5 MHCI−4 S100B−3 aSMA−2 MHCII−2
18	Emerging	3.9%	14.1%	85.9%	▲CD49+9 CD44+5 S100B+4 MHCI+3 SOX10+2 SOX2+2	▼MHCII−2 CCR4−1
16	Emerging	3.1%	13.9%	86.1%	▲SOX10+3	▼CD49−6 MHCI−4 SOX2−4 S100B−3 CD44−3 MHCII−2
17	Emerging	3.0%	19.2%	80.8%	▲MHCI+6 CD44+6 S100B+4 SOX10+2 SOX2+2 CD49+2 aSMA+2	▼CCR4−1
19	Emerging	2.8%	4.1%	95.9%	▲SOX10+4 S100B+3 CD49+3 MHCI+2 CD44+2	▼SOX2−3 aSMA−2
2	Emerging	1.8%	16.5%	83.5%	▲CD90+6 MHCI+3 S100B+2 SOX2+1 MHCII+1	▼ CD49−5
30	Emerging	0.9%	0.2%	99.8%	▲BCAT+9	▼CD49−5 MHCI−4 SOX10−3 S100B−3 SOX2−3 CD44−3 MHCII−2

Total percentage is calculated for each subset out of all melanoma subsets. Pre-Tx vs. Week 4 percentages are calculated out of the total for each subset. § MEM enrichment scores calculated for the subset vs. all other melanoma cells.

Doxie et al., Supplementary Figure S1

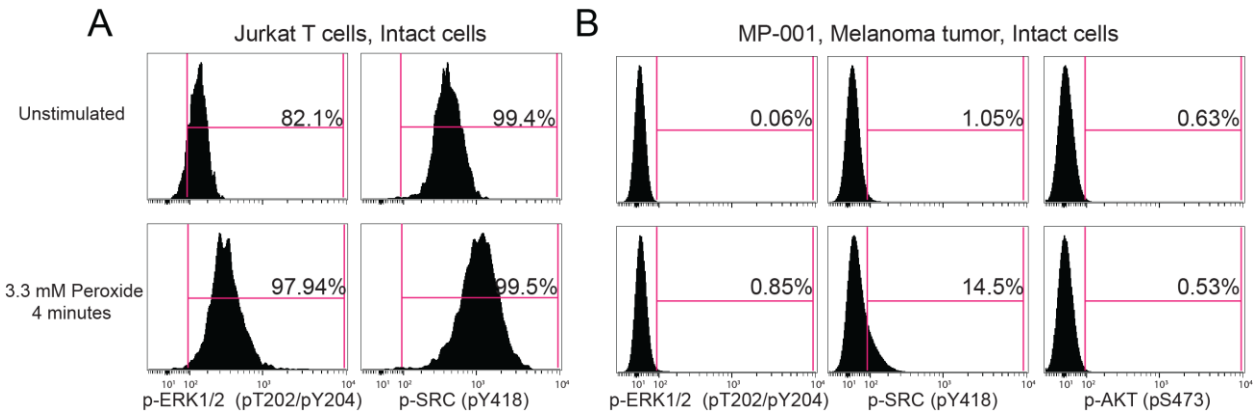

Figure 5-6 (S1) Little or no phosphorylation of ERK, SRC, or AKT was observed in melanoma tumor cells after BRAK and MEK inhibitor therapy. Post-therapy BRAF and MEK inhibitor-treated melanoma tumor cells and signaling positive control Jurkat T cells were stained with phospho-specific antibodies to quantify signaling potential. In (A) Jurkat T cells show high basal phosphorylation and induction of ERK and SRC phosphorylation following stimulation by phosphatase inhibitor peroxide (3.3 mM for 4 minutes). In (B) melanoma tumor cells from patient MP-001 showed low basal and potentiated signaling activity in unstimulated cells (top row) or following peroxide stimulation (bottom row).

Doxie et al., Supplementary Figure S2

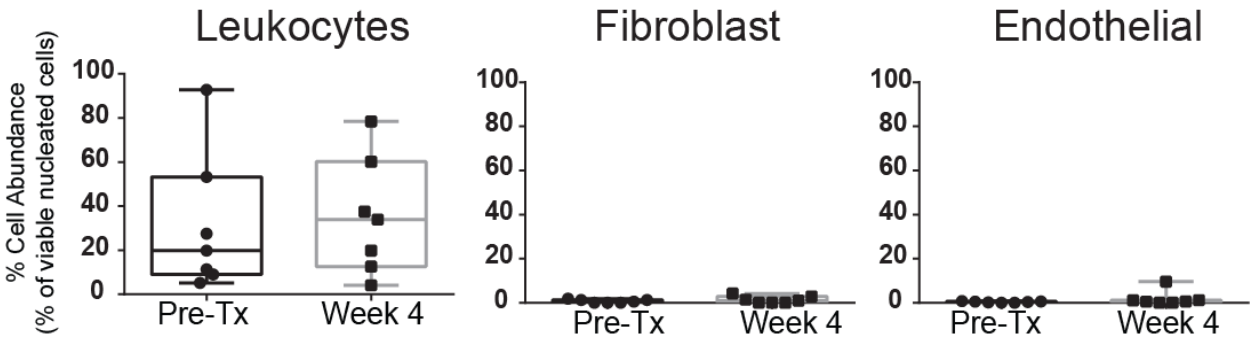

Figure 5-7 (S2) Targeting BRAF^{V600E} and MEK in melanoma did not significantly change the abundance of stromal leukocytes, fibroblasts, or endothelial cells. Sample level statistical analysis of 14 tumors viSNE gated cell populations (7 Pre-Tx tumors and 7 matched Week 4 post-therapy tumors). Wilcoxon signed rank tests were performed with a threshold of p=0.05.

Doxie et al., Supplementary Figure S3

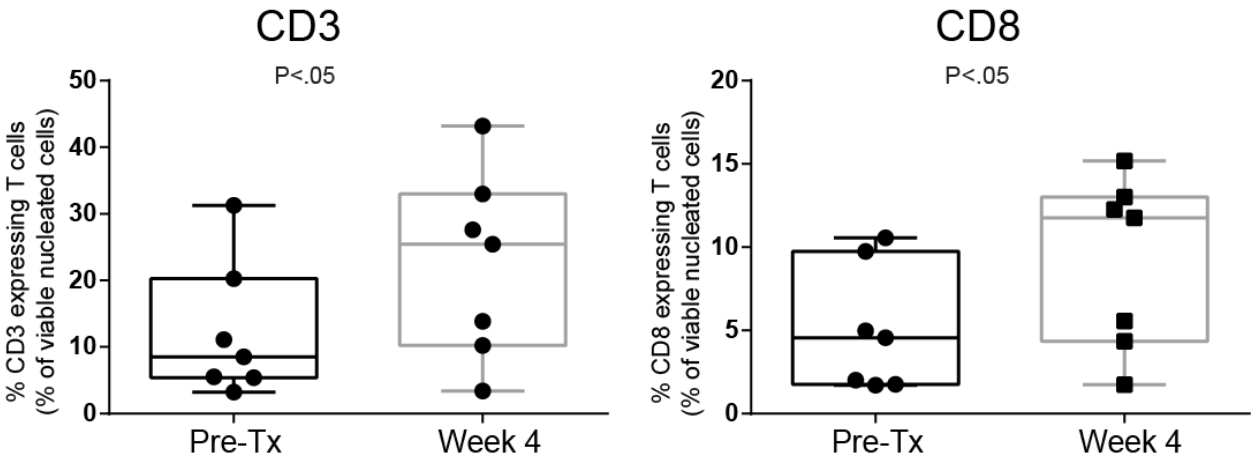

Figure 5-8 (S3) Targeting BRAF^{V600E} and MEK in melanoma tumors increased CD3^{+} T cell and CD8^{+} effector T cell infiltration. Sample level statistical analysis of 14 tumors % CD3 expressing T cells and % CD8 T cells (7 Pre-Tx tumors and 7 matched Week 4 post-therapy tumors). Wilcoxon signed rank tests were performed with a significance threshold of p=0.05 (p=0.02, and p=0.02).

Doxie et al., Supplementary Figure S4

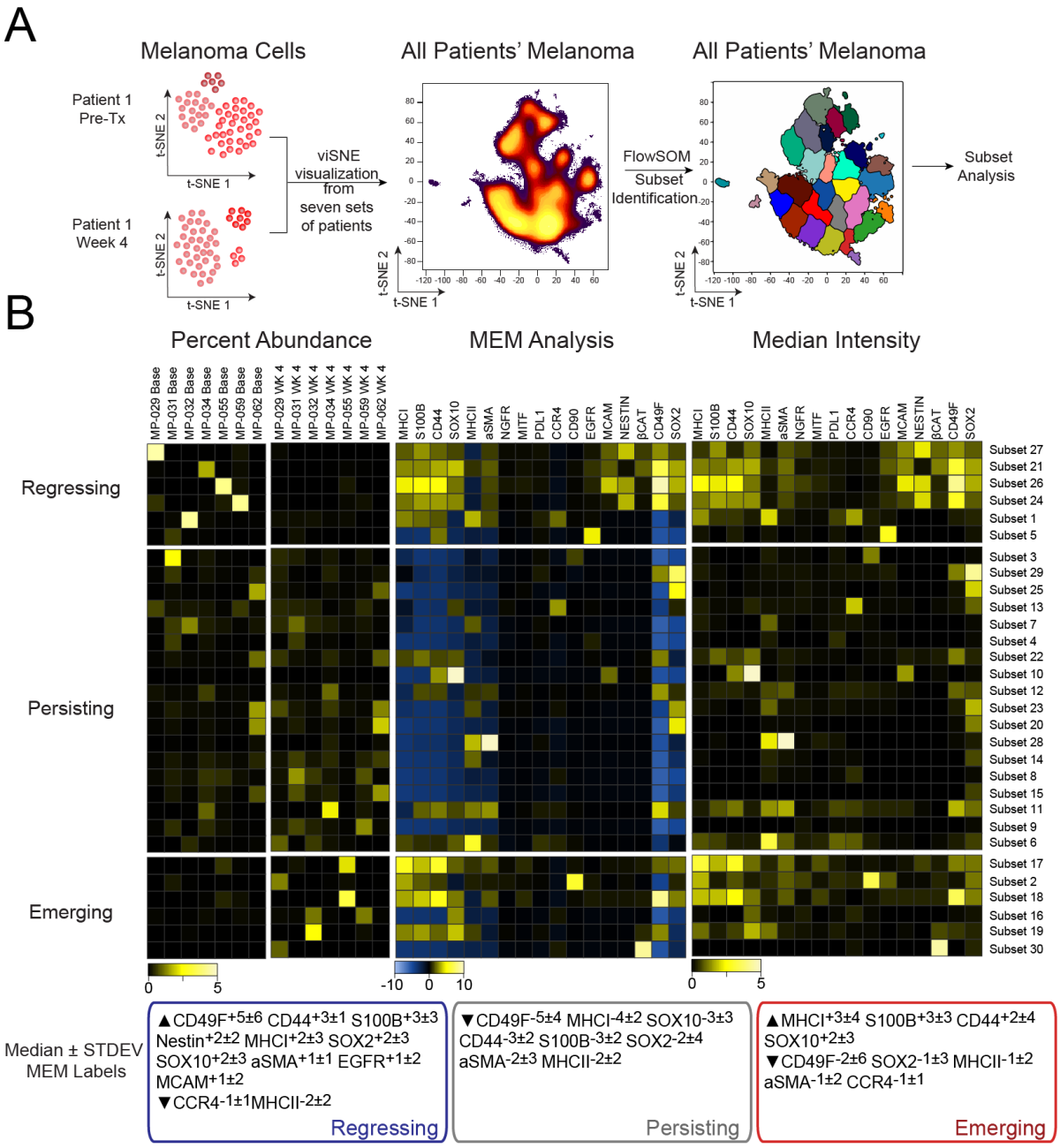

Figure 5-9 (S4) FlowSOM and MEM analysis quantitatively characterized features of melanoma subsets before and after therapy. (A) Subsets identified from a common viSNE map of all patients were identified with FlowSOM. (B) Marker enrichment modeling (MEM) analysis quantitatively labeled 30 cell subsets with 17 markers with the highest variance for melanoma cells across patients. Represented alongside MEM analysis are two additional heat maps of the percent abundance and median intensity for the same subsets.

Doxie et al., Supplementary Figure S5

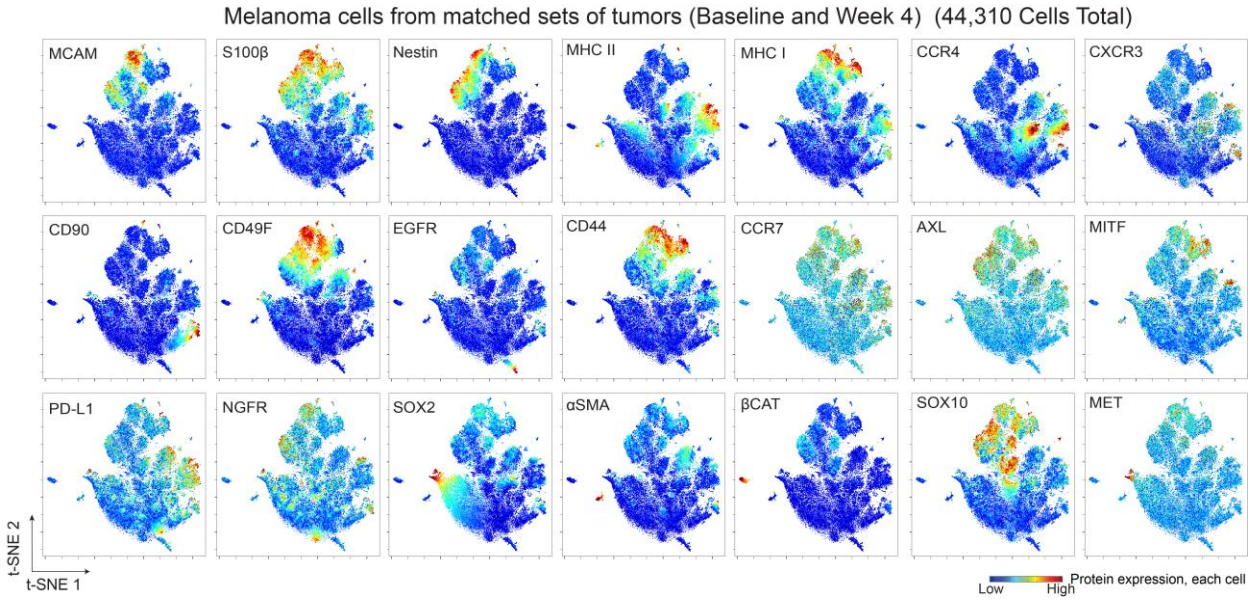

Figure 5-10 (S5) Visualization of cell phenotypes before and after therapy in patients with viSNE analysis. A viSNE analysis of all Pre-Tx and Week 4 melanoma cells from 7 matched samples. The viSNE plots display protein expression as heat for proteins with the greatest variance across patient samples.

Doxie et al., Supplementary Figure S6

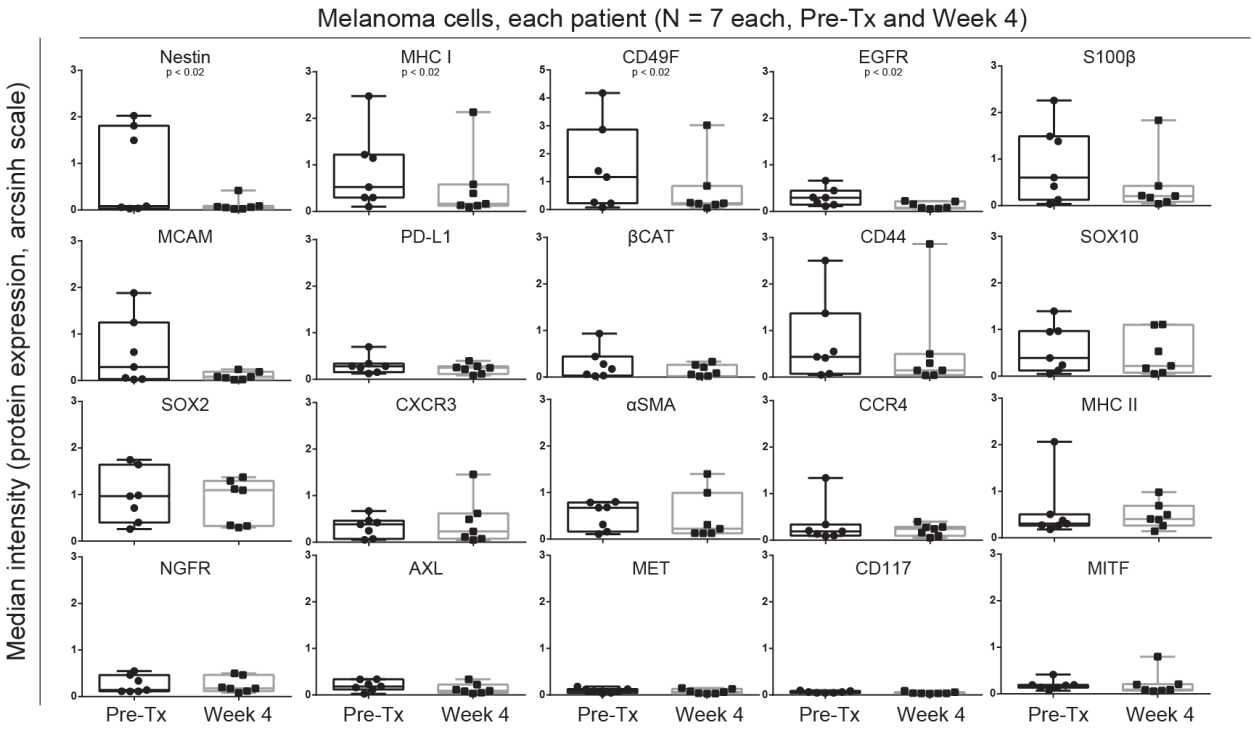

Figure 5-11 (S6). Median intensity for all features in Pre-Tx and Week 4 melanoma cells from all tumors studied with the optimized mass cytometry panel (Supplementary Table S2). Aggregate analysis of median intensity (arcsinh scale) for 20 measured proteins in melanoma cells gated as in Figure 1 from 14 tumor samples representing matched pairs of Pre-Tx and Week 4 from 7 individual patients. These graphs display additional data for samples shown in Figure 3 and Supplementary Figure S4 (e.g. AXL, MITF, and EGFR displayed here). Wilcoxon signed rank tests were performed and p-values less than 0.05 are shown.

Doxie et al., Supplementary Figure S7

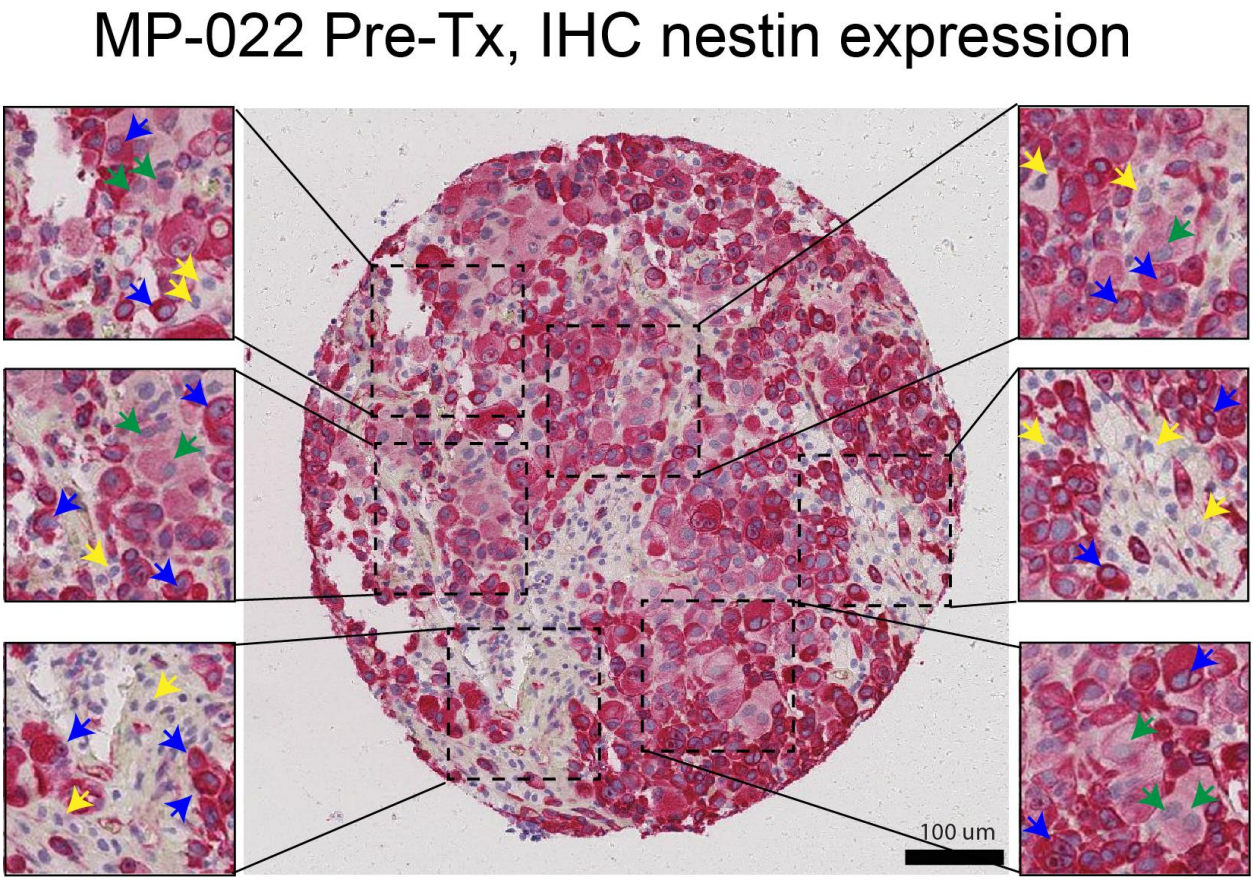

Figure 5-12 (S7). IHC of Nestin expression showed intra-tumor cellular diversity that was comparable to mass cytometry. Frozen, fixed, and paraffin embedded core biopsies at three points of treatment were used to acquire TMA's (tissue microarrays). Subcellular sections from the TMA <10 μm were used for immunohistochemistry of Nestin. Nestin expression was found to be high, medium or negative for tumor cells within several regions (blue=high, green=mid, yellow=negative).

Doxie et al., Supplementary Figure S8

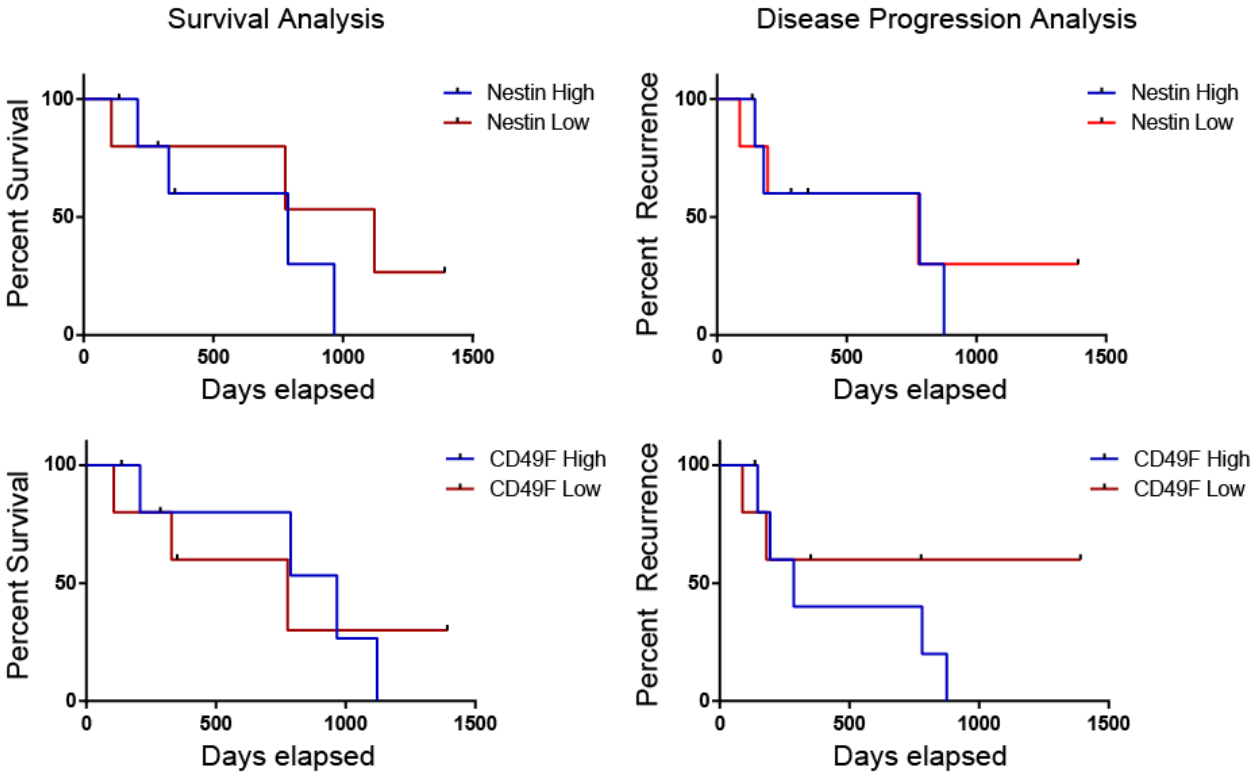

Figure 5-13 (S8). Kaplan-Meier curves for survival and progression in melanoma patients. Kaplan-Meier statistical analysis of 11 Pre-Tx tumors CD45 low/negative cells divided into two groups by median Nestin or CD49F expression. Patients with high expression of Nestin and CD49F did not have better overall survival and time to progression.

Doxie et al., Supplementary Figure S9

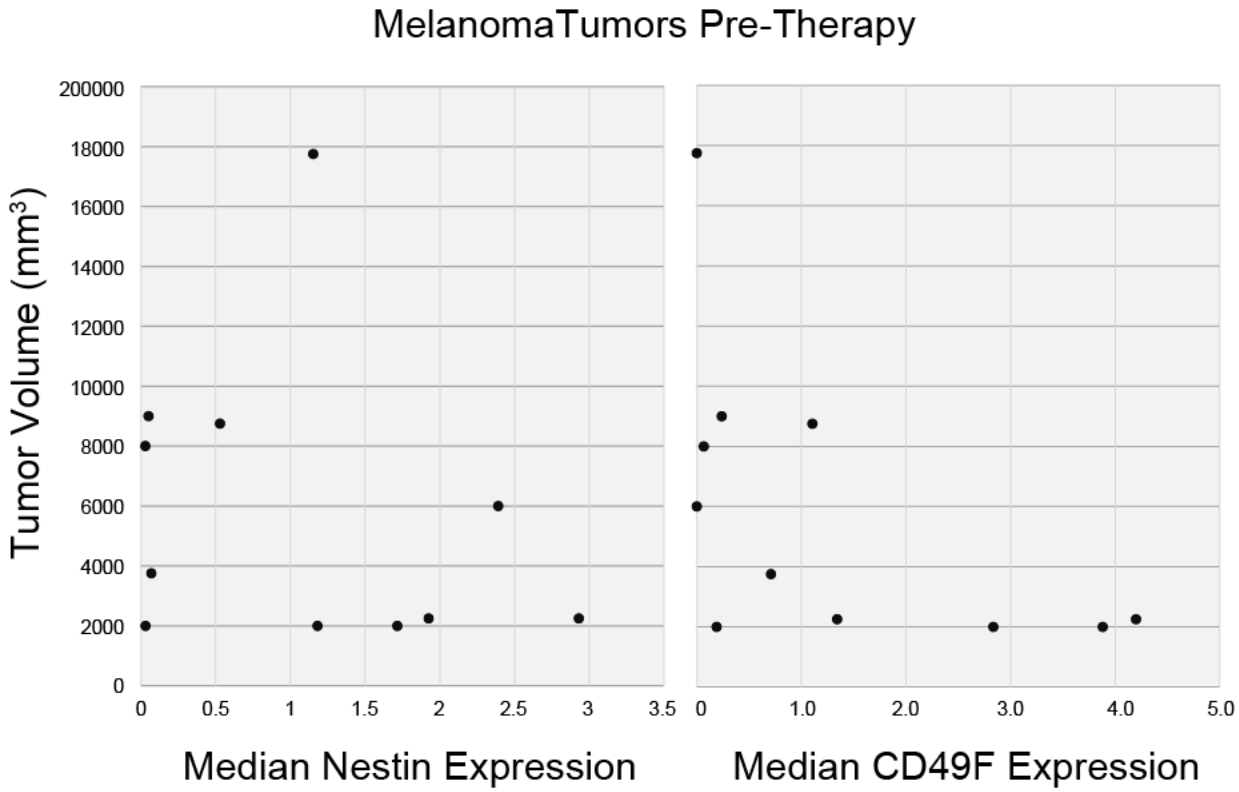

Figure 5-14 (S9). Tumor volume plotted against median Nestin or median CD49F protein expression in melanoma cells. Dot plots show eleven patients' Pre-Tx tumor volume compared to the median level Nestin protein expression or the median level of CD49F protein expression.

Doxie et al., Supplementary Figure S10

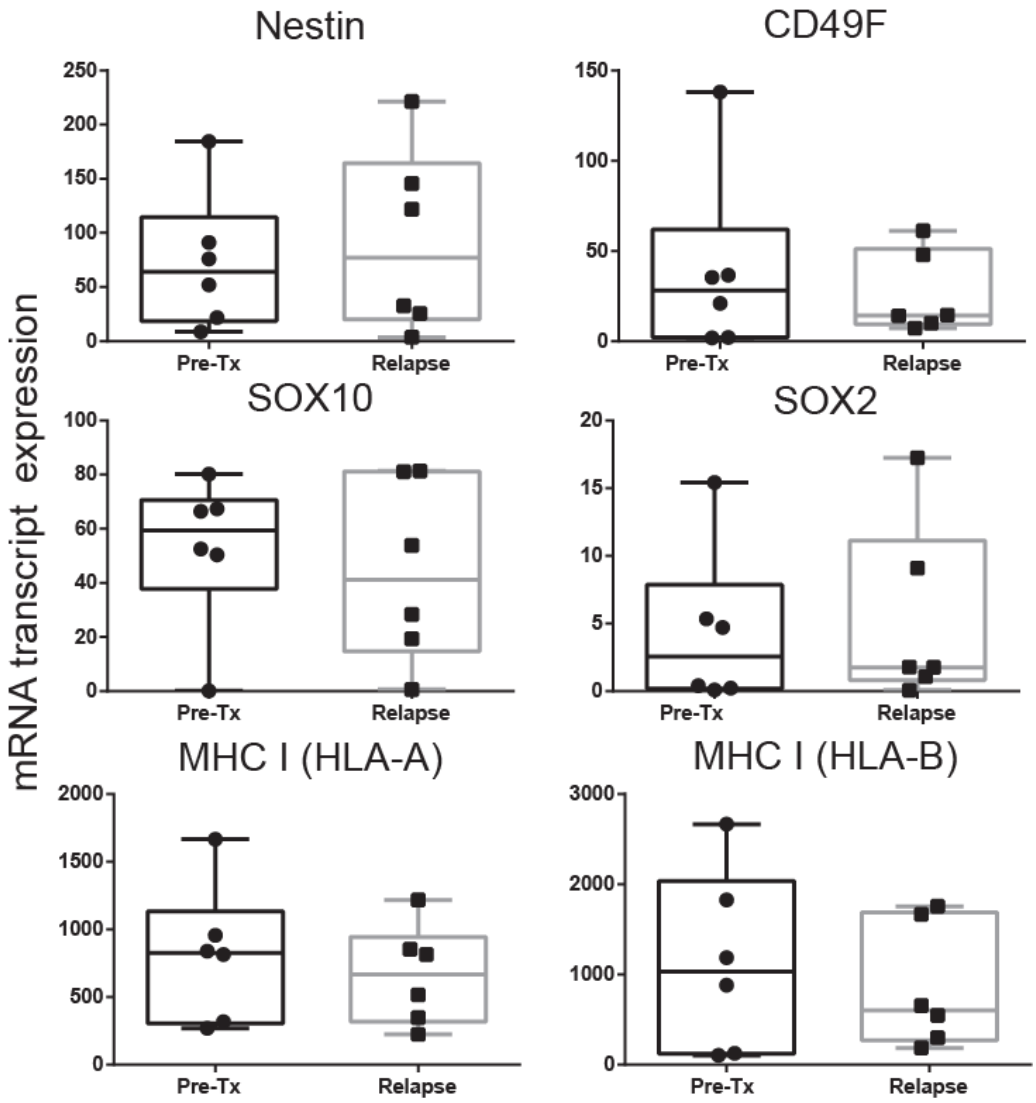

Figure 5-15 (S10) mRNA expression for Nestin, CD49F, SOX10, SOX2, MHC I (HLA-A), and MHC I (HLA-B) was not significantly decreased at the time of relapse in data from Tirosh et al. Box and whisker plots are pooled mRNA expression from 12 tumors and 6 patients' melanoma cells published by Tirosh et al., *Science* 2016. Tumors were therapy naïve or at the time of relapse following MAPK inhibitor treatment, in contrast with the time of surgical resection following 4 weeks of treatment, as here. The expression level of proteins that changed significantly here was quantified as $E_p(I)=\log_2(TPM(I)+1)$ where (I) is a set of cells and *TPM* is transcript per million. Wilcoxon signed rank tests were performed with a threshold of p=0.05

CHAPTER VI

CONCLUSIONS AND FUTURE DIRECTIONS

In this dissertation, single cell analysis approaches were utilized to identify and characterize complex cancer cell phenotypes, track cell populations and identify potential cellular mechanisms of therapy evasion. This approach is well suited to study melanoma because subclonal heterogeneity is widely suggested to be responsible for the array of resistance mechanisms to targeted therapies (Hugo et al., 2015; Van Allen et al., 2014). Furthermore, before my research began the field was burdened with a convoluted understanding of how tumor heterogeneity affects tumor growth (Quintana et al., 2010). In this dissertation, I hypothesized single cell dissection of melanoma tumors aided by computational would identify cells not eliminated by therapy would be revealed by a consistent protein expression pattern. In Chapters 2-5 of this dissertation, I demonstrated the progressive development of single cell mass cytometry tools and analysis approaches to investigate this hypothesis.

When my research began, high dimensional single cell approaches were a novel method to answer biological questions. To elucidate the utility of a high dimensional cytometric analysis approach, Chapter 2 presents a review that explores how his approach enables a multiplex view of single cell identity, signaling proteins, cell cycle status, proliferation, apoptosis, and biomarkers of clinical relevance. This approach was applied in Chapters 3 and 5 to identify and characterize biologically significant cellular phenotypes in melanoma. Going forward, I believe the content discussed in this review should be applicable to research in both basic science and translational research settings.

Furthermore, the discovery and validation of clinical signaling profiles discussed in Chapter 2 may be informative for studies that aim to reveal clinically relevant profiles from patients.

Modifications to signaling are a common feature of melanoma resistance to targeted therapy and immunotherapy. To identify aberrantly signaling melanoma cells, Chapter 3 presents the adaptation of the phospho-flow assay to dissect phosphorylation-induced signaling in melanoma cells. This approach resulted in a successful collaboration with Dr. Doug Johnson and Dr. Justin Balko that identified the MHC-II tumor positive phenotype as a positive prognostic feature of patients receiving anti-PD-1 immunotherapy. Furthermore, phospho-flow analysis revealed dysregulated JAK-STAT signaling was associated with the poor immuno-therapy prognosis phenotype. This work illustrated that extracellular protein expression or signaling activity can be used to identify clinically relevant melanoma subsets. From this work, it will be useful to further dissect the biological mechanism of aberrant MHC II expression in melanoma cells. The functional significance of MHC II's role in anti-PD-1 immunotherapy has yet to be elucidated. Experiments utilizing JAK inhibitors on human tumor co-cultures and xenograft models could reveal if dysregulated STAT signaling will enhance the potency of cell killing with immunotherapy.

The tools developed for population identification, cell fate, and function discussed in Chapter 2 can also be utilized to dissect heterogeneity of solid tissues. While tissue disaggregation and fluorescence cytometry have been utilized in the past, it was unknown if dissociation protocols developed previously would be effective for mass cytometry analysis. Moreover, systematic evaluation of protocols had not been evaluated for the maintenance of cellular diversity. In Chapter 4, the systematic evaluation of disaggregation reagents

revealed incubation of collagenase and DNase under 1 hour maintained tissue heterogeneity in suspension. This finding enabled the development of a workflow that would later be applied to tumors in a clinical study of human melanoma and adenocarcinoma. Going forward, the experimental methodology presented in Chapter 4 should be a starting point to identify effective disaggregation conditions for tissue types we did not test.

In Chapter 5. a 32-marker mass cytometry panel for melanoma was used to deeply characterize melanoma cell protein expression signatures before and after neoadjuvant therapy targeting BRAF and MEK. This work draws from the approaches and techniques demonstrated in Chapters 2-4 to reveal new in vivo biology of melanoma cells that had not been observed previously. Initially, heterogeneous melanoma tumors were consistently cleared of Nestin expressing melanoma cells. Moreover, persisting subset phenotypes also lacked surface expression of MHC I, which has also been observed as a mechanism of evasion of immunosurveillance. This study design and analysis approach could serve as a reference point to investigate novel combinatorial treatment strategies that aim to track cellular mechanisms of disease progression.

Since the conclusion of the study presented in Chapter 5, metastatic melanoma treatment has rapidly progressed to testing MAPK inhibitors with immunotherapies as a novel treatment strategy (Karachaliou et al., 2017). The overarching hypothesis is these combination therapies will create high response rates observed with small molecule inhibitors alone, and durable long-term remissions observed from single agent immunotherapies. Recently a phase I clinical trial reports combination checkpoint

immunotherapies and targeted therapies utilizing MAPK inhibitors and anti-PD-1/antiPDL1 are well tolerated, however, one study reports CTLA-4 and MAPK inhibitors can result in severe gastrointestinal events (Minor et al., 2015; Ribas et al., 2016). While an objective response rate of 60% for 15 patients treated with pembrolizumab, dabrafenib, and trametinib appear promising, currently combinatorial immunotherapy and targeted therapy regimens are considered investigational (Ribas et al., 2016).

Going forward, I recommend the workflow presented in Chapter 5 be applied to a larger cohort of patients (including a training and testing set) receiving combination checkpoint immunotherapy and targeted therapy. Utilizing a single cell approach could determine if this strategy eliminates cells that evade BRAF and MEK combination therapy. Ideally, I would acquire pre-therapy, post-therapy and relapse samples if patients presented with new tumors. Access to patient outcomes could also determine if the subsets identified are predictors of progression or survival. If enough cell suspensions were generated, I would also pair mass cytometry with single cell transcript profiling and cell sorting techniques. From this combination of single cell approaches, I would also aim to identify whether genetic mechanisms of resistance arise from nestin negative populations of melanoma cells. It may not be necessary to sort cell populations, however, it may strongly infer if certain cellular phenotypes are likely to develop mechanisms of resistance. Because intracellular loss of nestin was significantly associated with treatment response, an extracellular surrogate of nestin expression would be needed to sort cell populations. In most patients, I observed integrin alpha six was frequently associated with nestin

expression. To quantitatively determine which features were closely associated with nestin a Pearson's correlation could be used.

If patient samples could not be acquired, I would suggest using melanoma cells generated from syngeneic mouse models of melanoma. The SM1 and D4M melanoma cell lines have been established from conditional mouse models of metastatic melanoma, and are readily transplantable into immune competent hosts. D4M cells recapitulate human disease by expression of constitutively high p-ERK signaling and increased melanoma antigen after BRAF inhibition (Jenkins et al., 2014). SM1 cells have been utilized to show that $BRAF^{V600E}$ inhibitor vemurafenib improves the antitumor activity of adoptive cell immunotherapy and anti-PD-1 immunotherapy (Hu-Lieskovan et al., 2015; Koya et al., 2012). While the SM1 cell line has been tested with immune checkpoint inhibitors and targeted therapy, using a mouse model to test optimal timing and sequences of treatment is currently relevant to human trials. Furthermore, how therapy affects cellular heterogeneity after different points of treatment has not been shown in murine models.

If patients or mouse models relapse from these combinations of therapy, I would hypothesize that loss of immunosurveillance would mediate evasion from cell death. Low expression of MHC class I and dysregulation of immune presentation machinery has been observed to impair immune recognition (Garrido et al., 2016). In Chapter 5, I observed MHC I and II expression to decrease after BRAF and MEK inhibition, and subsets lacking MHC I were most stable in population abundance. A syngeneic mouse model testing combination checkpoint immunotherapy and targeted therapies reported increased MHC expression, however, this has not been observed in humans yet (Hu-Lieskovan et al.,

2015). However, boosting innate immune responses from NK cells or reactivating machinery to present antigen are possible methods to remove MHC negative cells (Garrido et al., 2016).

In Chapter 5, we were unable to determine if populations observed before therapy are likely to mediate relapse. Surprisingly, data from Tirosh et al. show no difference in nestin expression before treatment and at disease progression. Because melanoma patients' disease progresses rapidly after signfiicant loss of tumor burden, this suggests cellular plasticity could also play a role in shifting melanoma cell identity (Holzel et al., 2013). Furthermore, IHC data published previously from patient's tumors in Chapter 5 showed a decrease in Ki67 positive cells to an average of 2.9% at Week 4 (Johnson et al., 2015). Therefore, if intrinsically resistant cells are present I would expect the biological activity to remain unchanged. For example, in BRAF mutated colon cancer a 5% response rate to BRAF inhibition has been observed indicating an intrinsic resistance mechanism is present (Prahallad et al., 2012).

Instead of the selection of an intrinsically resistant stable cell population, I hypothesize therapy reprograms cells for a transient identity that is capable of shifting phenotype. In melanoma cells a slow cycling reversible phenotype has been documented to establish drug sensitive parent phenotypes upon drug withdrawal (Sharma et al., 2010). Moreover, two studies have utilized transcript profiling to reveal a gradual change in the transcriptome of melanoma cells exposed to BRAF inhibitors (Shaffer et al., 2017; Song et al., 2017). These studies conclude that drug exposure results in transient reprogramming that decreases MAPK dependency. The transient MAPK dependency is then followed by

reactivation of MAPK signaling from an acquired resistance mechanism (Song et al., 2017). However, cells could also reprogram away from MAPK signaling dependency (Song et al., 2017). These results could explain how successful rechallenge with BRAF inhibitors is possible for patients with metastatic melanoma (Seghers et al., 2012).

To date, slow growth phenotypes have been documented using human cell lines in vitro, patient-derived tumor xenografts, and murine melanoma in immune competent mice. I believe the next step would be to test this hypothesis with single cell transcript profiling and mass cytometry analysis from patient tumors receiving checkpoint immune therapy (e.g. anti-PD-1) and targeted therapies (dabrafenib and trametinib). In this study I would collect samples before therapy, after therapy, and during progression. I would also identify if this approach reveals loss of nestin expression overlapped with the slow growing phenotypes observed by other investigators. Ideally I would look for a gene and protein expression signature from single cells consistent with slow cycling behavior. In this model I propose that cellular reprogramming and genetic mechanisms of resistance might not be mutually exclusive. Furthermore, drug tolerant transient cell populations could serve as a resevior for acquired mechanisms of resistance to develop.

Overall, longitudinal analysis and single cell characterization of melanoma tumors revealed dynamic shifts in tumor phenotype that were not observed in other models of the disease. Because a common phenotype emerged in the cells that were not eliminated, other therapeutic windows before disease progression should also be studied to eliminate cells before progression develops. If this methodology were taken into the clinic to treat and

study melanoma, I believe the result would be a shift in the development of therapeutics to target cellular programs of cancer instead of individual mechanisms of resistance that may not be present in all cells.

Going forward, I believe mass cytometry could also be used to study other layers of cell biology other than protein expression and phosphorylated proteins in solid tumors. To date mass cytometry has also been utilized to study mRNA transcripts, DNA synthesis, and probes against hypoxic cellular states (Behbehani et al., 2012; Edgar et al., 2014; Frei et al., 2016). However, mass cytometry analysis comes with important limitations for clinical research that must be considered before planning studies. Because cells are ionized, it is not possible to recover cells after analysis. Additionally, due to the delivery mechanism, mass cytometry throughput speed is about 10-fold slower than fluorescence cytometry. Furthermore, mass cytometry shares some of the same limitations as fluorescence flow cytometry. High quality validated reagents must be selected and titrated before investigation. Since this project started (Irish and Doxie, 2014), many reagents and panels of antibodies have been developed for specific cell types and are now commercially available. Finally, data collected from the same clinical study at several institutions would benefit greatly from the use of a universally adopted standard to analyze data. Each instrument has its own ionization efficiency profile, but normalization reagents have been developed for quantitative comparisons between instruments (Finck et al., 2013; Tricot et al., 2015).

I believe the most practical use of mass cytometry in the clinic would be during evaluation of clinical studies to characterize malignant disease and monitoring the immune

system simultaneously. Just as measurements of tumor volume, tissue collection, and side effects are documented in clinical studies, mass cytometry analysis could be performed on samples that may be otherwise discarded or unused by a pathologist. Panels that leverage malignant cell phenotypes and functional properties could identify prognostic cell phenotypes and therapeutic targets such as upregulated signaling, expression of checkpoint inhibitors or aberrations in cell cycling (Behbehani, 2017). Similarly, panels that leverage immune cell phenotypes and functional properties could identify immune infiltration and states of suppression or action. Ideally, data collected from clinical studies could be used as a reference point for assessments in the clinic that lead to earlier detection of disease progression or adaptive changes to therapeutic strategy (Behbehani, 2017).

In conclusion, the methods described in this dissertation revealed new *in-vivo* biology of melanoma, and I believe this approach could have significant clinical applications in the future. Furthermore, as mass cytometry analyses are being applied to clinical studies of cancer, future studies should also consider longitudinal collection of samples in addition to patient outcomes. The study in Chapter 5 demonstrated that significant changes in cell identity after targeted therapy could represent a new target or therapeutic window that would have been overlooked by studying disease progression alone. Overall, the concepts of subset evasion, transient phenotypes, and the emergence of resistant cell phenotypes should be considered as potential mechanisms of disease resistance as therapeutic strategies advance.

APPENDIX

A. MASS CYTOMETRY AND COMPUATIONAL ANALYSIS DEFINES ADENOCARCINOMA POPULATIONS

This work consists of unpublished data that has been presented at AACR 2017.

Doxie DB, Lehman JM, Zou Y, Ortega MS, Roe CE, Irish JM, Massion PP. Single cell mass cytometry analysis of human lung adenocarcinoma. **Cancer Research AACR Abstracts**, 2017.

Preface

While the majority of my dissertation research focused on the analysis of solid melanoma tumors with the exception of Chapter 3. The tools and approaches demonstrated in my dissertation can be applied to other solid tumor types. Dissecting solid tumor heterogeneity in other cancers with single cell analysis tools should ultimately enable the discovery of novel features defining subsets that may be used for future therapeutic development. As a use case, I collaborated with Dr. Pierre Massion and Maria F. Senosain to develop mass cytometry panels and computational tools to dissect adenocarcinoma heterogeneity. Dr. Pierre Massion's overarching goal is to use single cell analysis tools to identify subset phenotypes associated with poor outcome at earlier points in disease progression. Ultimately, if poor outcome subsets can be identified before late-stage disease develops, personalized treatment strategies could be developed to more effectively target aggressive cellular phenotypes. To accomplish this I applied approaches discussed in Chapter 4 to retrieve viable single cells from human adenocarcinoma tumors. My analysis demonstrated the feasibility of mass cytometry analysis on human adenocarcinoma tumors that had not

been shown previously. Furthermore, computational tools viSNE and MEM analysis characterized novel and known tumor cell phenotypes.

Introduction

Lung cancer is the leading cause of cancer-related mortality in the world (Jemal et al., 2009). Lung adenocarcinoma is the most common subtype. Tumor heterogeneity among adenocarcinomas presents a challenge in the management of the disease (Jordan et al., 2017). Understanding heterogeneity may have implications in understanding the biological processes driving progression. Single cell platforms like mass cytometry offer an opportunity to profile tumor heterogeneity and to identify populations of driven by the activation of signaling pathways. In this collaborative project, mass cytometry panels and computational tools were developed specifically to quantitatively characterize human adenocarcinoma tumor heterogeneity.

Methods

Adenocarcinomas were collected at the time of surgery and dissociated into suspension and cryopreserved. Mass cytometry analysis of tumors and adenocarcinoma cell lines was performed with a 30 marker antibody panels and rhodium intercalator dye to identify dead cells. The antibody panel included markers to characterize identity, cell cycle status, and signaling events. Gating with dimensionality reduction tool viSNE was used to compare major populations of cells.

Results

Validation of mass cytometry panels was performed with adenocarcinoma cell lines and human tumors. Mass cytometry analysis of PC9 (lung), A549 (lung), H520 (squamous) and

SW620 (colon) cells identified carcinoma cell lines exhibited phenotypically distinct cells between samples by expression of cytokeratin, CK7, and EGFR (Figure A-1). Furthermore, vimentin associated with epithelial to mesenchymal transition, p-STAT signaling molecules, and immune suppression ligand PD-L1 was not uniformly expressed on PC9, H520, and A549 cells (Figure A-1). This approach revealed mass cytometry panels and computational tool viSNE visualize heterogeneity between and within carcinoma samples.

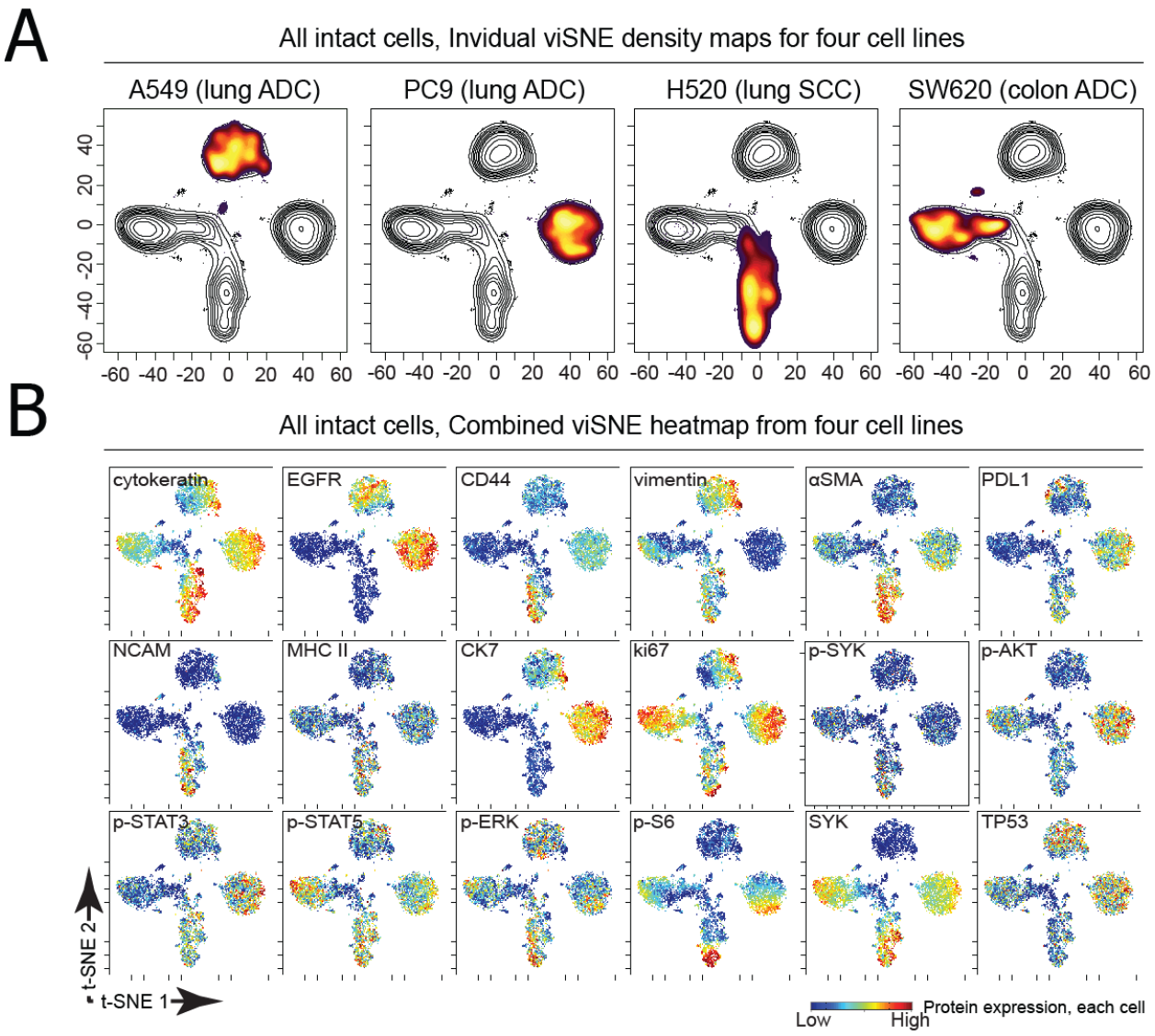

Figure A-16 Mass cytometry analysis and computational tools visualize diverse carcinoma cell phenotypes. (A) Four carcinoma cells were analyzed by mass cytometry and characterized using dimensionality reduction tool t-SNE/viSNE. Density plots show the identity, abundance, and phenotypic diversity of carcinoma cell lines tested with an adenocarcinoma signaling focused panel. Abundance is displayed as heat specifically for each sample. Density diagrams overlay black and white contour plots of all cells run within one viSNE analysis simultaneously. (B) A combination viSNE heat plot shows all cells combined in one analysis to display per-cell expression of the indicated proteins on a rainbow scale where red indicates high expression and blue indicates low expression.

Disaggregation of an adenocarcinoma tumor was performed with established protocols to create single cell suspensions (Leelatian et al., 2017a). Viable cells were detected after excluding dead cells with rhodium intercalator and biaxial gating of histone $H3^{+}$ nucleated cells. Tumor heterogeneity was visualized using the Cytobank implementation of viSNE/t-SNE (Amir el et al., 2013), which organized cells in a two dimensional graph so that cells with similar protein expression patterns were placed near each other to form islands of phenotypically similar cells. Using a 30-marker panel and expert gating several subsets were identified within islands formed by dense cellular events and marker expression patterns. The most abundant stromal populations were defined as leukocytes ($CD45^{hi}$ and MHC class I) and endothelial cells (PECAM/CD31 and MHC class I) (Figure A-2 and Figure A-3). Adenocarcinoma cells were defined as epithelial cells that express cytokeratin and lack of MHC class I (Figure A-2 and Figure A-3). Next, marker enrichment modeling (MEM, (Diggins et al., 2018; Diggins et al., 2017) objectively described the enriched protein features of the observed tumor cell types. MEM of adenocarcinoma cells identified subsets were specifically enriched for cytokeratin and p-STAT3 signaling transcription factor (Figure A-3). Furthermore, MEM analysis objectively described leukocyte subsets consistent with antigen present cell, and neutrophil, and T cell identity (Figure A-3).

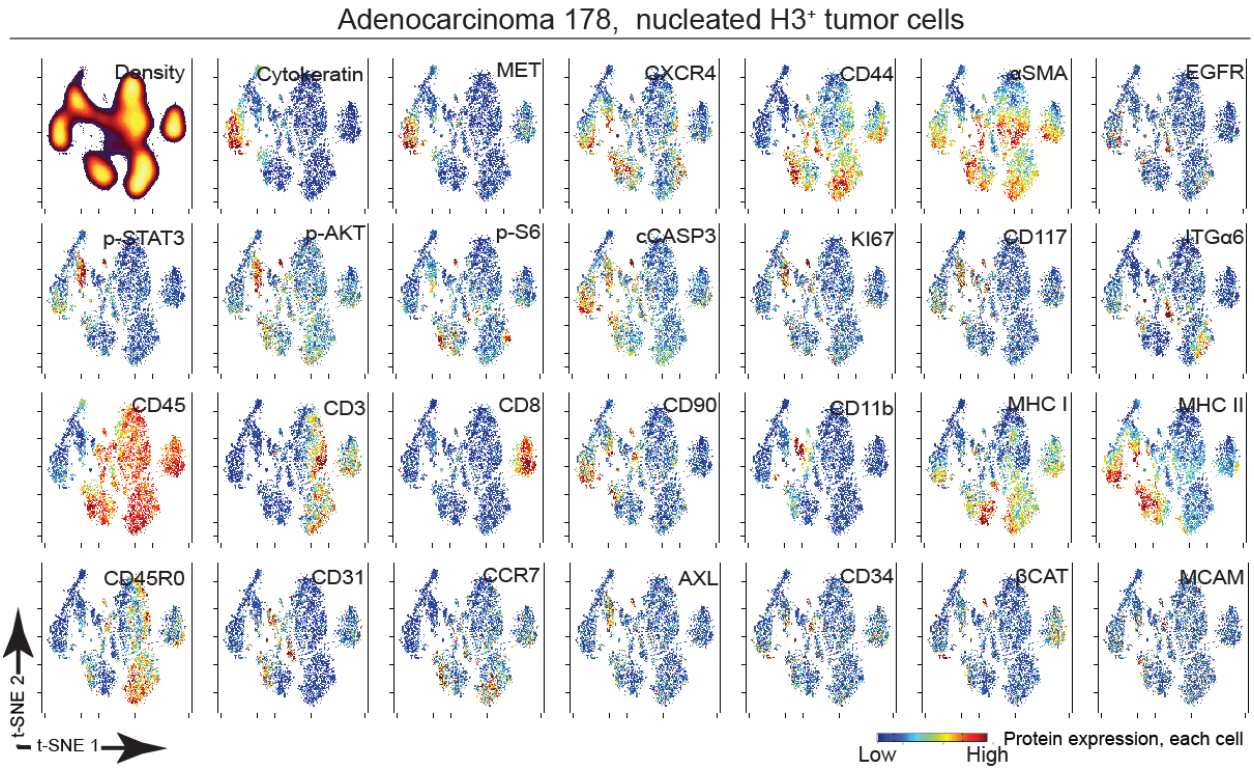

Figure A-17 Mass cytometry analysis and computational tools characterize adenocarcinoma solid tumor heterogeneity. Viable single cells were isolated following established protocols , analyzed by mass cytometry and characterized using dimensionality reduction tool t-SNE/viSNE. Heat plots display per-cell expression of the indicated label as either cellular abundance or protein on a rainbow scale where red indicates high expression and blue indicates low expression.

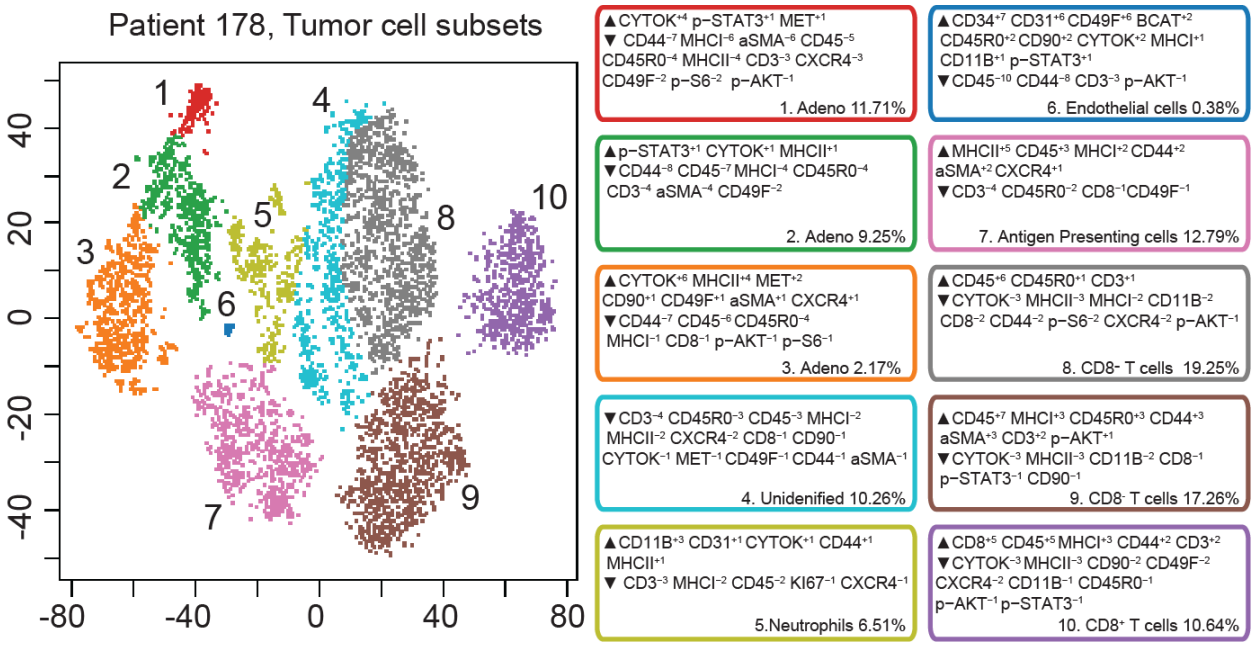

Figure A-18 Marker enrichment modeling quantitatively characterizes cellular phenotypes consistent with known tumor cell identities. MEM labels from patient 178's viSNE analysis were used to identify and characterize cells from an adenocarcinoma tumor (populations displayed in color). MEM labels quantified protein enrichment (▲ up to +10) or specific absence (▼ down to -10) in the indicated tumor cell subset. For example, adenocarcinoma cells in subset 1 had the label ▲CYTOK^{+4} p-STAT3^{+1} MET^{+1} ▼CD44^{-7} MHCI^{-6} aSMA^{-6} CD45^{-5}, which identified this population as adenocarinoma cells based on enrichment of CYTOK and MET proteins and a lack of MHC I protein expression.

Conclusions

Populations of infiltrating stromal cells and cancer cells were identified in lung adenocarcinoma. The single cell phenotyping from tumors was consistent with the profile found in two lung adenocarcinoma cell lines. Preliminary differences in basal signaling pathways responsible for growth were observed within adenocarcinoma cell populations. This work demonstrates the feasibility of mass cytometry to identify and characterize tumor heterogeneity. Work is underway to define phenotypes within the epithelial and leukocyte populations that could predict tumor behavior and immune response within the microenvironment.

REFERENCES

Afanas'ev, I. B. (2010). Signaling by reactive oxygen and nitrogen species in skin diseases. Current drug metabolism *11*, 409-414.

Aghaeepour, N., Finak, G., Flow, C. A. P. C., Consortium, D., Hoos, H., Mosmann, T. R., Brinkman, R., Gottardo, R., and Scheuermann, R. H. (2013). Critical assessment of automated flow cytometry data analysis techniques. Nature methods *10*, 228-238.

Akiyama, M., Matsuda, Y., Ishiwata, T., Naito, Z., and Kawana, S. (2013). Nestin is highly expressed in advanced-stage melanomas and neurotized nevi. Oncology reports *29*, 1595-1599.

Al-Hajj, M., Wicha, M. S., Benito-Hernandez, A., Morrison, S. J., and Clarke, M. F. (2003). Prospective identification of tumorigenic breast cancer cells. Proceed ings of the National Academy of Sciences of the United States of America *100*, 3983-3988.

Alexandrescu, D. T., Ichim, T. E., Riordan, N. H., Marincola, F. M., Di Nardo, A., Kabigting, F. D., and Dasanu, C. A. (2010). Immunotherapy for melanoma: current stat us and perspectives. Journal of immunotherapy (Hagerstown, Md : 1997) *33*, 570-590.

Amir el, A. D., Davis, K. L., Tadmor, M. D., Simonds, E. F., Levine, J. H., Bendall, S. C., Shenfeld, D. K., Krishnaswamy, S., Nolan, G. P., and Pe'er, D. (2013). viSNE enab les visualization of high dimensional single-cell data and reveals phenotypic heterogeneity of leukemia. Nature biotechnology *31*, 545-552.

Andreeff, M., Slater, D. E., Bressler, J., and Furth, M. E. (1986). Cellular ras oncogene expression and cell cycle measured by flow cytometry in hematopoietic cell lines. Blood *67*, 676-681.

Armstrong, J. S., Steinauer, K. K., Hornung, B., Irish, J. M., Lecane, P., Birrell, G. W., Peehl, D. M., and Knox, S. J. (2002). Role of glutathione depletion and reactive oxygen species generation in apoptotic signaling in a human B lymphoma cell line. Cell Death Differ *9*, 252-263.

Azimi, F., Scolyer, R. A., Rumcheva, P., Moncrieff, M., Murali, R., McCarthy, S. W., Saw, R. P., and Thompson, J. F. (2012). Tumor -infiltrating lymphocyte grade is an independent predictor of sentinel lymph node status and survival in patients with cutaneous melanoma. Journal of clinical oncology : official journal of the American Society of Clinical Oncology *30*, 2678-2683.

Baerlocher, G. M., Vulto, I., de Jong, G., and Lansdorp, P. M. (2006). Flow cytometry and FISH to measure the average length of telomeres (flow FISH). Nature protocols *1*, 2365-2376.

Baitsch, L., Baumgaertner, P., Devevre, E., Raghav, S. K., Legat, A., Barba, L., Wieckowski, S., Bouzourene, H., Deplancke, B., Romero, P.*, et al.* (2011). Exhaustion of tumor-specific CD8(+) T cells in metastases from melanoma patients. The Journal of clinical investigation *121*, 2350-2360.

Bandura, D. R., Baranov, V. I., Ornatsky, O. I., Antonov, A., Kinach, R., Lou, X., Pavlov, S., Vorobiev, S., Dick, J. E., and Tanner, S. D. (2009). Mass cytometry: technique for real time single cell multitarget immunoassay based on inductively coupled plasma time-of-flight mass spectrometry. Analytical chemistry *81*, 6813-6822.

Barcellos-Hoff, M. H., Lyden, D., and Wang, T. C. (2013). The evolution of the cancer niche during multistage carcinogenesis. Nature reviews Cancer *13*, 511-518.

Becher, B., Schlitzer, A., Chen, J., Mair, F., Sumatoh, H. R., Teng, K. W., Low, D., Ruedl, C., Riccardi-Castagnoli, P., Poidinger, M.*, et al.* (2014). High -dimensional analysis of the murine myeloid cell system. Nature immunology *15*, 1181-1189.

Behbehani, G. K. (2017). Applications of Mass Cytometry in Clinical Medicine: The Promise and Perils of Clinical CyTOF. Clinics in laboratory medicine *37*, 945-964.

Behbehani, G. K., Bendall, S. C., Clutter, M. R., Fantl, W. J., and Nolan, G. P. (2012). Single-cell mass cytometry adapted to measurements of the cell cycle. Cytometry Part A : the journal of the International Society for Analytical Cytology *81*, 552-566.

Behbehani, G. K., Thom, C., Zunder, E. R., Finck, R., Gaudilliere, B., Fragiadakis, G. K., Fantl, W. J., and Nolan, G. P. (2014). Transient partial permeabilization with saponin enables cellular barcoding prior to surface marker staining. Cytometry Part A : the journal of the International Society for Analytical Cytology *85*, 1011-1019.

Belloc, F., Belaud-Rotureau, M. A., Lavignolle, V., Bascans, E., Braz-Pereira, E., Durrieu, F., and Lacombe, F. (2000). Flow cytometry detection of caspase 3 activation in preapoptotic leukemic cells. Cytometry *40*, 151-160.

Bendall, S. C., and Nolan, G. P. (2012). From single cells to deep phenotypes in cancer. Nature biotechnology *30*, 639-647.

Bendall, S. C., Nolan, G. P., Roederer, M., and Chattopadhyay, P. K. (2012). A deep profiler's guide to cytometry. Trends in immunology *33*, 323-332.

Bendall, S. C., Simonds, E. F., Qiu, P., Amir el, A. D., Krutzik, P. O., Finck, R., Bruggner, R. V., Melamed, R., Trejo, A., Ornatsky, O. I.*, et al.* (2011). Single -cell mass cytometry of differential immune and drug responses across a human hematopoietic continuum. Science (New York, NY) *332*, 687-696.

Bernatchez, C., Radvanyi, L. G., and Hwu, P. (2012). Advances in the trea tment of metastatic melanoma: adoptive T-cell therapy. Seminars in oncology *39*, 215-226.

Bjornson, Z. B., Nolan, G. P., and Fantl, W. J. (2013). Single -cell mass cytometry for analysis of immune system functional states. Current opinion in immunology *25*, 484-494.

Blankenstein, T., Coulie, P. G., Gilboa, E., and Jaffee, E. M. (2012). The determinants of tumour immunogenicity. Nature reviews Cancer *12*, 307-313.

Bodenmiller, B., Zunder, E. R., Finck, R., Chen, T. J., Savig, E. S., Bruggner, R. V., Simonds, E. F., Bendall, S. C., Sachs, K., Krutzik, P. O., and Nolan, G. P. (2012). Multiplexed mass cytometry profiling of cellular states perturbed by small-molecule regulators. Nature biotechnology *30*, 858-867.

Boiko, A. D., Razorenova, O. V., van de Rijn, M., Swetter, S. M., Johnson, D. L., Ly, D. P., Butler, P. D., Yang, G. P., Joshua, B., Kaplan, M. J.*, et al.* (2010). Human melanoma -initiating cells express neural crest nerve growth factor receptor CD271. Nature *466*, 133-137.

Bourton, E. C., Plowman, P. N., Zahir, S. A., Senguloglu, G. U., Serrai, H., Bottley, G., and Parris, C. N. (2012). Multispectral imaging flow cytometry reveals distinct frequencies of gamma-H2AX foci induction in DNA double strand break repair defective human cell lines. Cytometry Part A : the journal of the International Society for Analytical Cytology *81*, 130-137.

Bruns, H. A., and Kaplan, M. H. (2006). The role of constitutively active Stat6 in leukemia and lymphoma. Critical reviews in oncology/hematology *57*, 245-253.

Byrd, J. C., Furman, R. R., Coutre, S. E., Flinn, I. W., Burger, J. A., Blum, K. A., Grant, B., Sharman, J. P., Coleman, M., Wierda, W. G.*, et al.* (2013). Targeting BTK with ibrutinib

in relapsed chronic lymphocytic leukemia. The New England journal of medicine *369*, 32-42.

Calo, V., Migliavacca, M., Bazan, V., Macaluso, M., Buscemi, M., Gebbia, N., and Russo, A. (2003). STAT proteins: from normal control of cellular events to tumorigenesis. Journal of cellular physiology *197*, 157-168.

Carney, W. P., Petit, D., Hamer, P., Der, C. J., Finkel, T., Cooper, G. M., Lefebvre, M., Mobtaker, H., Delellis, R., Tischler, A. S., and et al. (1986). Monoclonal antibody specific for an activated RAS protein. Proceedings of the National Academy of Sciences of the United States of America *83*, 7485-7489.

Castillo, R., Mascarenhas, J., Telford, W., Chadburn, A., Friedman, S. M., and Schattner, E. J. (2000). Proliferative response of mantle cell lymphoma cells stimulated by CD40 ligation and IL-4. Leukemia *14*, 292-298.

Chan, K. S., Espinosa, I., Chao, M., Wong, D., Ailles, L., Diehn, M., Gill, H., Presti, J., Jr., Chang, H. Y., van de Rijn, M.*, et al.* (2009). Identification, molecular characterization, clinical prognosis, and therapeutic targeting of human bladder tumor-initiating cells. Proceedings of the National Academy of Sciences of the United States of America *106*, 14016-14021.

Chapman, P. B., Hauschild, A., Robert, C., Haanen, J. B., Ascierto, P., Larkin, J., Dummer, R., Garbe, C., Testori, A., Maio, M.*, et al.* (2011). Improved survival with v emurafenib in melanoma with BRAF V600E mutation. The New England journal of medicine *364*, 2507-2516.

Chow, S., and Hedley, D. (1995). Flow cytometric determination of glutathione in clinical samples. Cytometry *21*, 68-71.

Cooperman, J., Neely, R., Teachey, D. T., Grupp, S., and Choi, J. K. (2004). Cell division rates of primary human precursor B cells in culture reflect in vivo rates. Stem Cells *22*, 1111-1120.

Crawford, T. Q., Jalbert, E., Ndhlovu, L. C., and Barbour, J. D. (2014). Concomitant evaluation of PMA+ionomycin-induced kinase phosphorylation and cytokine production in T cell subsets by flow cytometry. Cytometry Part A : the journal of the International Society for Analytical Cytology *85*, 268-276.

Dalerba, P., Kalisky, T., Sahoo, D., Rajendran, P. S., Rothenberg, M. E., Leyrat, A. A., Sim, S., Okamoto, J., Johnston, D. M., Qian, D.*, et al.* (2011). Single -cell dissection of transcriptional heterogeneity in human colon tumors. Nature biotechnology *29*, 1120-1127.

Daniel, V. C., Marchionni, L., Hierman, J. S., Rhodes, J. T., Devereux, W. L., Rudin, C. M., Yung, R., Parmigiani, G., Dorsch, M., Peacock, C. D., and Watkins, D. N. (2009). A primary xenograft model of small-cell lung cancer reveals irreversible changes in gene expression imposed by culture in vitro. Cancer research *69*, 3364-3373.

Das Thakur, M., Salangsang, F., Landman, A. S., Sellers, W. R., Pryer, N. K., Levesque, M. P., Dummer, R., McMahon, M., and Stuart, D. D. (2013). Modelling vemurafenib resistance in melanoma reveals a strategy to forestall drug resistance. Nature *494*, 251-255.

Davies, H., Bignell, G. R., Cox, C., Stephens, P., Edkins, S., Clegg, S., Teague, J., Woffendin, H., Garnett, M. J., Bottomley, W.*, et al.* (2002). Mutations of the BRAF gene in human cancer. Nature *417*, 949-954.

Denu, J. M., and Tanner, K. G. (1998). Specific and reversible inactivation of protein tyrosine phosphatases by hydrogen peroxide: evidence for a sulfenic acid intermediate and implications for redox regulation. Biochemistry *37*, 5633-5642.

Dickinson, B. C., and Chang, C. J. (2008). A targetable fluorescent probe for imaging hydrogen peroxide in the mitochondria of living cells. Journal of the American Chemical Society *130*, 9638-9639.

Diggins, K. E., Ferrell, P. B., Jr., and Irish, J. M. (2015). Methods for discovery and characterization of cell subsets in high dimensional mass cytometry data. Methods (San Diego, Calif) *82*, 55-63.

Diggins, K. E., Gandelman, J. S., Roe, C. E., and Irish, J. M. (2018). Generating Quantitative Cell Identity Labels with Marker Enrichment Modeling (MEM). Current protocols in cytometry / editorial board, J Paul Robinson, managing editor [et al] *83*, 10.21.11-10.21.28.

Diggins, K. E., Greenplate, A. R., Leelatian, N., Wogsland, C. E., and Irish, J. M. (2017). Characterizing cell subsets using marker enrichment modeling. Nature methods *14*, 275-278.

Donnenberg, V. S., Landreneau, R. J., Pfeifer, M. E., and Donnenberg, A. D. (2013). Flow cytometric determination of stem/progenitor content in epithelial tissues: an example from nonsmall lung cancer and normal lung. Cytometry Part A : the journal of the International Society for Analytical Cytology *83*, 141-149.

Dudley, M. E., Wunderlich, J. R., Yang, J. C., Sherry, R. M., Topalian, S. L., Restifo, N. P., Royal, R. E., Kammula, U., White, D. E., Mavroukakis, S. A.*, et al.* (2005). Adoptive cell transfer therapy following non-myeloablative but lymphodepleting chemotherapy for the treatment of patients with refractory metastatic melanoma. Journal of clinical oncology : official journal of the American Society of Clinical Oncology *23*, 2346-2357.

Edgar, L. J., Vellanki, R. N., Halupa, A., Hedley, D., Wouters, B. G., and Nitz, M. (2014). Identification of hypoxic cells using an organotellurium tag compatible with mass cytometry. Angewandte Chemie (I nternational ed in English) *53*, 11473-11477.

Erdmann, F., Lortet-Tieulent, J., Schuz, J., Zeeb, H., Greinert, R., Breitbart, E. W., and Bray, F. (2013). International trends in the incidence of malignant melanoma 1953 -2008--are recent generations at higher or lower risk? International journal of cancer Journal international du cancer *132*, 385-400.

Erlanson, M., and Landberg, G. (1998). Flow cytometric quantification of cyclin E in human cell lines and hematopoietic malignancies. Cytometry *32*, 214-222.

Fienberg, H. G., Simonds, E. F., Fantl, W. J., Nolan, G. P., and Bodenmiller, B. (2012). A platinum-based covalent viability reagent for single-cell mass cytometry. Cytometry Part A : the journal of the International Society for Analytical Cytology *81*, 467-475.

Finck, R., Simonds, E. F., Jager, A., Krishnaswamy, S., Sachs, K., Fantl, W., Pe'er, D., Nolan, G. P., and Bendall, S. C. (2013). Normalization of mass cytometry data with bead standards. Cytometry Part A : the journal of the International Society for Analytical Cytology *83*, 483-494.

FitzGerald, M. G., Harkin, D. P., Silva-Arrieta, S., MacDonald, D. J., Lucchina, L. C., Unsal, H., O'Neill, E., Koh, J., Finkelstein, D. M., Isselbacher, K. J.*, et al.* (1996). Prevalence of germ-line mutations in p16, p19ARF, and CDK4 in familial melanoma: analysis of a clinic-based population. Proceedings of the National Academy of Sciences of the United States of America *93*, 8541-8545.

Flaherty, K. T., Infante, J. R., Daud, A., Gonzalez, R., Kefford, R. F., Sosman, J., Hamid, O., Schuchter, L., Cebon, J., Ibrahim, N.*, et al.* (2012). Combined BRAF and MEK

inhibition in melanoma with BRAF V600 mutations. The New England journal of medicine *367*, 1694-1703.

Frederick, D. T., Piris, A., Cogdill, A. P., Cooper, Z. A., Lezcano, C., Ferrone, C. R., Mitra, D., Boni, A., Newton, L. P., Liu, C.*, et al.* (2013). BRAF inhibition is associated with enhanced melanoma antigen expression and a more favorable tumor microenvironment in patients with metastatic melanoma. Clinical cancer research : an official journal of the American Association for Cancer Research *19*, 1225-1231.

Frei, A. P., Bava, F. A., Zunder, E. R., Hsieh, E. W., Chen, S. Y., Nolan, G. P., and Gherardini, P. F. (2016). Highly multiplexed simultaneous detection of RNAs and proteins in single cells. Nature methods *13*, 269-275.

Fusi, A., Ochsenreither, S., Busse, A., Rietz, A., and Keilholz, U. (2010). Expression of the stem cell marker nestin in peripheral blood of patients with melanoma. The British journal of dermatology *163*, 107-114.

Garcia-Lora, A., Algarra, I., and Garrido, F. (2003). MHC class I antigens, immune surveillance, and tumor immune escape. Journal of cellular physiology *195*, 346-355.

Garibyan, L., and Fisher, D. E. (2010). How sunlight causes melanoma. Current oncology reports *12*, 319-326.

Garraway, L. A., and Janne, P. A. (2012). Circumventing cancer drug resistance in the era of personalized medicine. Cancer discovery *2*, 214-226.

Garrido, F., Aptsiauri, N., Doorduijn, E. M., Garcia Lora, A. M., and van Hall, T. (201 6). The urgent need to recover MHC class I in cancers for effective immunotherapy. Current opinion in immunology *39*, 44-51.

Gerdes, M. J., Sevinsky, C. J., Sood, A., Adak, S., Bello, M. O., Bordwell, A., Can, A., Corwin, A., Dinn, S., Filkins, R. J., *et al.* (2013). Highly multiplexed single -cell analysis of formalin-fixed, paraffin-embedded cancer tissue. Proc Natl Acad Sci U S A *110*, 11982-11987.

Gerner, M. Y., Kastenmuller, W., Ifrim, I., Kabat, J., and Germain, R. N. (2012). Histo -cytometry: a method for highly multiplex quantitative tissue imaging analysis applied to dendritic cell subset microanatomy in lymph nodes. Immunity *37*, 364-376.

Girotti, M. R., Pedersen, M., Sanchez-Laorden, B., Viros, A., Turajlic, S., Niculescu-Duvaz, D., Zambon, A., Sinclair, J., Hayes, A., Gore, M., *et al.* (2013). Inhibiting EGF receptor or SRC family kinase signaling overcomes BRAF inhibitor resistance in melanoma. Cancer discovery *3*, 158-167.

Goldstein, A. M., and Tucker, M. A. (2001). Genetic epidemiology of cutaneous melanoma: a global perspective. Archives of dermatology *137*, 1493-1496.

Green, M. R., Gentles, A. J., Nair, R. V., Irish, J. M., Kihira, S., Liu, C. L., Kela, I., Hopmans, E. S., Myklebust, J. H., Ji, H., *et al.* (2013). Hierarchy in somatic mutations arising during genomic evolution and progression of follicular lymphoma. Blood *121*, 1604-1611.

Gross, P., Honnorat, N., Varol, E., Wallner, M., Trappanese, D. M., Sharp, T. E., Starosta, T., Duran, J. M., Koller, S., Davatzikos, C., and Houser, S. R. (2016). Nuquantus: Machine learning software for the characterization and quantification of cell nuclei in complex immunofluorescent tissue images. Scientific reports *6*, 23431.

Hamid, O., Robert, C., Daud, A., Hodi, F. S., Hwu, W. J., Kefford, R., Wolchok, J. D., Hersey, P., Joseph, R. W., Weber, J. S., *et al.* (2013). Safety and tumor responses with

lambrolizumab (anti -PD-1) in melanoma. The New England journal of medicine *369*, 134-144.

Hanahan, D., and Weinberg, R. A. (20 11). Hallmarks of cancer: the next generation. Cell *144*, 646-674.

Handoko, H. Y., Boyle, G. M., Ferguson, B., Muller, H. K., Soyer, H. P., and Walker, G. J. (2013). Plasticity of melanoma in vivo: murine lesions resulting from Trp53, but not Cdk4 or Arf deregulation, display neural transdifferentiation. Pigment cell & melanoma research *26*, 731-734.

Hasegawa, D., Bugarin, C., Giordan, M., Bresolin, S., Longoni, D., Micalizzi, C., Ramenghi, U., Bertaina, A., Basso, G., Locatelli, F.*, et al.* (2013). Validation of flow cytometric phospho-STAT5 as a diagnostic tool for juvenile myelomonocytic leukemia. Blood cancer journal *3*, e160.

Hodi, F. S., O'Day, S. J., McDermott, D. F., Weber, R. W., Sosman, J. A., Haanen, J. B., Gonzalez, R., Robert, C., Schadendorf, D., Hassel, J. C.*, et al.* (2010). Improved survival with ipilimumab in patients with metastatic melanoma. The New England journal of medicine *363*, 711-723.

Hodis, E., Watson, I. R., Kryukov, G. V., Arold, S. T., Imielinski, M., Theurillat, J. P., Nickerson, E., Auclair, D., Li, L., Place, C.*, et al.* (2012). A landscape of driver mutations in melanoma. Cell *150*, 251-263.

Holyoake, T., Jiang, X., Eaves, C., and Eaves, A. (1999). Isolation of a highly quiescent subpopulation of primitive leukemic cells in chronic myeloid leukemia. Blood *94*, 2056-2064.

Holzel, M., Bovier, A., and Tuting, T. (2013). Plasticity of tumour and immune cells: a source of heterogeneity and a cause for therapy resistance? Nature reviews Cancer *13*, 365-376.

Hu-Lieskovan, S., Mok, S., Homet Moreno, B., Tsoi, J., Robert, L., Goedert, L., Pinheiro, E. M., Koya, R. C., Graeber, T. G., Comin-Anduix, B., and Ribas, A. (2015). Improved antitumor activity of immunotherapy with BRAF and MEK inhibitors in BRAF(V600E) melanoma. Science translational medicine *7*, 279ra241.

Huang, X., Traganos, F., and Darzynkiewicz, Z. (2003). DNA damage induced by DNA topoisomerase I- and topoisomerase II-inhibitors detected by histone H2AX phosphorylation in relation to the cell cycle phase and apoptosis. Cell cycle *2*, 614-619.

Hugo, W., Shi, H., Sun, L., Piva, M., Song, C., Kong, X., Moriceau, G., Hong, A., Dahlman, K. B., Johnson, D. B.*, et al.* (2015). Non -genomic and Immune Evolution of Melanoma Acquiring MAPKi Resistance. Cell *162*, 1271-1285.

Irish, J., Hovland, R., Krutzik, P., Perez, O., Bruserud, O., Gjertsen, B., and Nolan, G. (2004a). Single cell profiling of potentiated phospho -protein networks in cancer cells. Cell *118*, 217-228.

Irish, J., Kotecha, N., and Nolan, G. (2006a). Innovation - Mapping normal and cancer cell signalling networks: towards single-cell proteomics. Nature Reviews Cancer *6*, 146-155.

Irish, J. M. (2014). Beyond the age of cellular discovery. Nature immunology *15*, 1095-1097.

Irish, J. M., Anensen, N., Hovland, R., Skavland, J., Borresen-Dale, A.-L., Bruserud, O., Nolan, G. P., and Gjertsen, B. T. (2007). Flt3 Y591 duplication and Bc1 -2

overexpression are detected in acute myeloid leukemia cells with high levels of phosphorylated wild-type p53. Blood *109*, 2589-2596.

Irish, J. M., Czerwinski, D. K., Nolan, G. P., and Levy, R. (2006b). Altered B -cell receptor signaling kinetics distinguish human follicular lymphoma B cells from tumor-infiltrating nonmalignant B cells. Blood *108*, 3135-3142.

Irish, J. M., Czerwinski, D. K., Nolan, G. P., and Levy, R. (2006c). Altered B -cell receptor signaling kinetics distinguish human follicular lymphoma. B cells from tumor-infiltrating nonmalignant B cells. Blood *108*, 3135-3142.

Irish, J. M., and Doxie, D. B. (2014). High -dimensional single-cell cancer biology. Current topics in microbiology and immunology *377*, 1-21.

Irish, J. M., Hovland, R., Krutzik, P. O., Perez, O. D., Bruserud, O., Gjertsen, B. T., and Nolan, G. P. (2004b). Single cell profiling of potentiated phospho -protein networks in cancer cells. Cell *118*, 217-228.

Irish, J. M., Myklebust, J. H., Alizadeh, A. A., Houot, R., Sharman, J. P., Czerwinski, D. K., Nolan, G. P., and Levy, R. (2010a). B -cell signaling networks reveal a negative prognostic human lymphoma cell subset that emerges during tumor progression. Proceedings of the National Academy of Sciences of the United States of America *107*, 12747-12754.

Irish, J. M., Myklebust, J. H., Alizadeh, A. A., Houot, R., Sharman, J. P., Czerwinski, D. K., Nolan, G. P., and Levy, R. (2010b). B -cell signaling networks reveal a negative prognostic human lymphoma cell subset that emerges during tumor progression. Proceedings of the National Academy of Sciences of the United States of America *107*, 12747-12754.

Jemal, A., Siegel, R., Ward, E., Hao, Y., Xu, J., and Thun, M. J. (2009). Cancer statistics, 2009. CA: a cancer journal for clinicians *59*, 225-249.

Jenkins, M. H., Steinberg, S. M., Alexander, M. P., Fisher, J. L., Ernstoff, M. S., Turk, M. J., Mullins, D. W., and Brinckerhoff, C. E. (2014). Multiple murine BRaf(V60 0E) melanoma cell lines with sensitivity to PLX4032. Pigment cell & melanoma research *27*, 495-501.

Jiang, X., Zhou, J., Giobbie-Hurder, A., Wargo, J., and Hodi, F. S. (2013). The activation of MAPK in melanoma cells resistant to BRAF inhibition promotes PD-L1 expression that is reversible by MEK and PI3K inhibition. Clinical cancer research : an official journal of the American Association for Cancer Research *19*, 598-609.

Johannessen, C. M., Boehm, J. S., Kim, S. Y., Thomas, S. R., Wardwell, L., Johnson, L. A., Emery, C. M., Stransky, N., Cogdill, A. P., Barretina, J.*, et al.* (2010). COT drives resistance to RAF inhibition through MAP kinase pathway reactivation. Nature *468*, 968-972.

Johnson, A. S., Crandall, H., Dahlman, K., and Kelley, M. C. (2015). Prelim inary results from a prospective trial of preoperative combined BRAF and MEK-targeted therapy in advanced BRAF mutation-positive melanoma. Journal of the American College of Surgeons *220*, 581-593 e581.

Johnson, D. B., Estrada, M. V., Salgado, R., Sanchez, V., Doxie, D. B., Opalenik, S. R., Vilgelm, A. E., Feld, E., Johnson, A. S., Greenplate, A. R.*, et al.* (2016). Melanoma - specific MHC-II expression represents a tumour-autonomous phenotype and predicts response to anti-PD-1/PD-L1 therapy. Nature communications *7*, 10582.

Johnson, G. L., Stuhlmiller, T. J., Angus, S. P., Zawistowski, J. S., and Graves, L. M. (2014). Molecular Pathways: Adaptive Kinome Reprogramming in Response to Targeted

Inhibition of the BRAF-MEK-ERK Pathway in Cancer. Clinical cancer research : an official journal of the American Association for Cancer Research.

Jordan, E. J., Kim, H. R., Arcila, M. E., Barron, D., Chakravarty, D., Gao, J., Chang, M. T., Ni, A., Kundra, R., Jonsson, P.*, et al.* (2017). Prospective Comprehensive Molecular Characterization of Lung Adenocarcinomas for Efficient Patient Matching to Approved and Emerging Therapies. Cancer discovery *7*, 596-609.

Juan, G., Traganos, F., James, W. M., Ray, J. M., Roberge, M., Sauve, D. M., Anderson, H., and Darzynkiewicz, Z. (1998). Hi stone H3 Phosphorylation and Expression of Cyclins A and B1 Measured in Individual Cells During Their Progression Through G2 and Mitosis. Cytometry *32*, 71-77.

Kalisky, T., and Quake, S. R. (2011). Single -cell genomics. Nature methods *8*, 311-314.

Kammula, U. S., White, D. E., and Rosenberg, S. A. (1998). Trends in the safety of high dose bolus interleukin-2 administration in patients with metastatic cancer. Cancer *83*, 797-805.

Kang, X., Kawakami, Y., el-Gamil, M., Wang, R., Sakaguchi, K., Yannelli, J. R., Appella, E., Rosenberg, S. A., and Robbins, P. F. (1995). Identification of a tyrosinase epitope recognized by HLA-A24-restricted, tumor-infiltrating lymphocytes. Journal of immunology (Baltimore, Md : 1950) *155*, 1343-1348.

Karachaliou, N., Gonzalez-Cao, M., Sosa, A., Berenguer, J., Bracht, J. W. P., Ito, M., and Rosell, R. (2017). The combination of checkpoint immunotherapy and targeted therapy in cancer. Annals of translational medicine *5*, 388.

Kim, T., Amaria, R. N., Spencer, C., Reuben, A., Cooper, Z. A., and Wargo, J. A. (2014). Combining targeted therapy and immune checkpoint inhibitors in the treatment of metastatic melanoma. Cancer biology & medicine *11*, 237-246.

Kotecha, N., Floress, N. J., Irish, J. M., Simonds, E. F., Sakai, D. S., Archambeault, S., Diaz-Flores, E., Coram, M., Shannon, K. M., Nolan, G. P., and Loh, M. L. (2008). Single -cell profiling identifies aberrant STAT5 activation in myeloid malignancies with specific clinical and biologic correlates. Cancer cell *14*, 335-343.

Kotecha, N., Krutzik, P. O., and Irish, J. M. (2010). Web -based analysis and publication of flow cytometry experiments. Current protocols in cytometry / editorial board, J Paul Robinson, managing editor [et al] *Chapter 10*, Unit10 17.

Koussounadis, A., Langdon, S. P., Um, I. H., Harrison, D. J., and Smith, V. A. (2015). Relationship between differentially expressed mRNA and mRNA-protein correlations in a xenograft model system. Scientific reports *5*, 10775.

Koya, R. C., Mok, S., Otte, N., Blacketor, K. J., Comin-Anduix, B., Tumeh, P. C., Minasyan, A., Graham, N. A., Graeber, T. G., Chodon, T., and Ribas, A. (2012). BRAF inhibitor vemurafenib improves the antitumor activity of adoptive cell immunotherapy. Cancer research *72*, 3928-3937.

Krebsbach, P. H., and Villa-Diaz, L. G. (2 017). The Role of Integrin alpha6 (CD49f) in Stem Cells: More than a Conserved Biomarker. Stem cells and development *26*, 1090-1099.

Krutzik, P. O., Crane, J. M., Clutter, M. R., and Nolan, G. P. (2008). High -content single-cell drug screening with phosphospecific flow cytometry. Nature chemical biology *4*, 132-142.

Krutzik, P. O., Hale, M. B., and Nolan, G. P. (2005). Characterization of the murine immunological signaling network with phosphospecific flow cytometry. J Immunol *175*, 2366-2373.

Krutzik, P. O., Irish, J. M., Nolan, G. P., and Perez, O. D. (2004). Analysis of protein phosphorylation and cellular signaling events by flow cytometry: techniques and clinical applications. Clin Immunol *110*, 206-221.

Krutzik, P. O., and Nolan, G. P. (2003). Intracellula r phospho-protein staining techniques for flow cytometry: monitoring single cell signaling events. Cytometry Part A : the journal of the International Society for Analytical Cytology *55*, 61-70.

Krutzik, P. O., and Nolan, G. P. (2006). Fluorescent cell barc oding in flow cytometry allows high-throughput drug screening and signaling profiling. Nature methods *3*, 361-368.

Laane, E., Tani, E., Bjorklund, E., Elmberger, G., Everaus, H., Skoog, L., and Porwit-MacDonald, A. (2005). Flow cytometric immunophenotyping including Bcl-2 detection on fine needle aspirates in the diagnosis of reactive lymphadenopathy and non-Hodgkin's lymphoma. Cytometry B Clin Cytom *64*, 34-42.

Ladstein, R. G., Bachmann, I. M., Straume, O., and Akslen, L. A. (2014). Nestin expression is associated with aggressive cutaneous melanoma of the nodular type. Modern pathology : an official journal of the United States and Canadian Academy of Pathology, Inc *27*, 396-401.

Landau, D. A., Carter, S. L., Stojanov, P., McKenna, A., Stevenson, K., Lawrence, M. S., Sougnez, C., Stewart, C., Sivachenko, A., Wang, L.*, et al.* (2013). Evolution and impact of subclonal mutations in chronic lymphocytic leukemia. Cell *152*, 714-726.

Lawrence, M. S., Stojanov, P., Polak, P., Kryukov, G. V., Cibulskis, K., Sivachenko, A., Carter, S. L., Stewart, C., Mermel, C. H., Roberts, S. A.*, et al.* (2013). Mutational heterogeneity in cancer and the search for new cancer-associated genes. Nature *499*, 214-218.

Lee, C. W., Zhan, Q., Lezcano, C., Frank, M. H., Huang, J., Larson, A. R., Lin, J. Y., Wan, M. T., Lin, P. I., Ma, J., *et al.* (2014). Nestin depletion induces melanoma matrix metalloproteinases and invasion. Laboratory investigation; a journal of technical methods and pathology *94*, 1382-1395.

Lee, H. L., Park, M. H., Song, J. K., Jung, Y. Y., Kim, Y., Kim, K. B., Hwang, D. Y., Yoon, D. Y., Song, M. J., Han, S. B., and Hong, J. T. (2017). Correction: Tumor growth suppressive effect of IL-4 through p21-mediated activation of STAT6 in IL-4Ralpha overexpressed melanoma models. Oncotarget *8*, 41778.

Lee, P. P., Yee, C., Savage, P. A., Fong, L., Brockstedt, D., Weber, J. S., Johnson, D., Swetter, S., Thompson, J., Greenberg, P. D., *et al.* (1999). Characterization of circulating T cells specific for tumor-associated antigens in melanoma patients. Nat Med *5*, 677-685.

Leelatian, N., Diggins, K. E., and Irish, J. M. (2015). Characterizing Phenotypes and Signaling Networks of Single Human Cells by Mass Cytometry. Methods in molecular biology *1346*, 99-113.

Leelatian, N., Doxie, D. B., Greenplate, A. R., Mobley, B. C., Lehman, J. M., Sinnaeve, J., Kauffmann, R. M., Werkhaven, J. A., Mistry, A. M., Weaver, K. D., *et al.* (2016). Single cell analysis of human tissues and solid tumors with mass cytometry. Cytometry B Clin Cytom.

Leelatian, N., Doxie, D. B., Greenplate, A. R., Mobley, B. C., Lehman, J. M., Sinnaeve, J., Kauffmann, R. M., Werkhaven, J. A., Mistry, A. M., Weaver, K. D., *et al.* (2017a). Single cell analysis of human tissues and solid tumors with mass cytometry. Cytometry Part B, Clinical cytometry *92*, 68-78.

Leelatian, N., Doxie, D. B., Greenplate, A. R., Sinnaeve, J., Ihrie, R. A., and Irish, J. M. (2017b). Preparing Viable Single Cells from Human Tissue and Tumors for Cytomic Analysis. Current protocols in molecular biology *118*, 25C 21 21-25C 21 23.

Levine, J. H., Simonds, E. F., Bendall, S. C., Davis, K. L., Amir el, A. D., Tadmor, M. D., Litvin, O., Fienberg, H. G., Jager, A., Zunder, E. R.*, et al.* (2015). Data -Driven Phenotypic Dissection of AML Reveals Progenitor-like Cells that Correlate with Prognosis. Cell *162*, 184-197.

Liu, C., Peng, W., Xu, C., Lou, Y., Zhang, M., Wargo, J. A., Chen, J. Q., Li, H. S., Watowich, S. S., Yang, Y.*, et al.* (2013). BRAF inhibition increases tumor infiltration by T cells and enhances the antitumor activity of adoptive immunotherapy in mice. Clinical cancer research : an official journal of the American Association for Cancer Research *19*, 393-403.

Madore, J., Vilain, R. E., Menzies, A. M., Kakavand, H., Wilmott, J. S., Hyman, J., Yearley, J. H., Kefford, R. F., Thompson, J. F., Long, G. V.*, et al.* (2015). PD -L1 expression in melanoma shows marked heterogeneity within and between patients: implications for anti-PD-1/PD-L1 clinical trials. Pigment cell & melanoma research *28*, 245-253.

Maecker, H. T., and Levy, R. (1989). Prevalence of antigen receptor variants in human T cell lines and tumors. J Immunol *142*, 1395-1404.

Maecker, H. T., McCoy, J. P., and Nussenblatt, R. (2012). Standardizing immunophenotyping for the Human Immunology Project. Nature reviews Immunology *12*, 191-200.

Maecker, H. T., and Trotter, J. (2006). Flow cytometry controls, instrument setup, and the determination of positivity. Cytometry Part A : the journal of the International Society for Analytical Cytology *69*, 1037-1042.

Mahoney, K. M., Freeman, G. J., and McDermott, D. F. (2015). The Next Immune - Checkpoint Inhibitors: PD-1/PD-L1 Blockade in Melanoma. Clinical therapeutics *37*, 764-782.

Marcy, Y., Ouverney, C., Bik, E. M., Losekann, T., Ivanova, N., Martin, H. G., Szeto, E., Platt, D., Hugenholtz, P., Relman, D. A., and Quake, S. R. (2007). Dissecting biological "dark matter" with single-cell genetic analysis of rare and uncultivated TM7 microbes from the human mouth. Proceedings of the National Academy of Sciences of the United States of America *104*, 11889-11894.

Marusyk, A., and Polyak, K. (2010). Tumor heterogeneity: causes and consequences. Biochimica et biophysica acta *1805*, 105-117.

Mason, D., Andre, P., Bensussan, A., Buckley, C., Civin, C., Clark, E., de Haas, M., Goyert, S., Hadam, M., Hart, D*., et al.* (2002). CD antigens 2002. Blood *99*, 3877-3880.

Mayle, A., Luo, M., Jeong, M., and Goodell, M. A. (2013). Flow cytometry analysis of murine hematopoietic stem cells. Cytometry Part A : the journal of the International Society for Analytical Cytology *83*, 27-37.

Meacham, C. E., and Morrison, S. J. (2013). Tumour heterogeneity and cancer cell plasticity. Nature *501*, 328-337.

Minor, D. R., Puzanov, I., Callahan, M. K., Hug, B. A., and Hoos, A. (2015). Severe gastrointestinal toxicity with administration of trametinib in combination with dabrafenib and ipilimumab. Pigment cell & melanoma research *28*, 611-612.

Mittal, D., Gubin, M. M., Schreiber, R. D., and Smyth, M. J. (2014). New insights into cancer immunoediting and its three component phases--elimination, equilibrium and escape. Current opinion in immunology *27*, 16-25.

Morkve, O., Halvorsen, O. J., Stangeland, L., Gulsvik, A., and Laerum, O. D. (1992). Quantitation of biological tumor markers (p53, c -myc, Ki-67 and DNA ploidy) by multiparameter flow cytometry in non-small-cell lung cancer. Int J Cancer *52*, 851-855.

Mort, R. L., Jackson, I. J., and Patton, E. E. (2015). The melanocyte lineage in development and disease. Development (Cambridge, England) *142*, 620-632.

Mroz, E. A., Tward, A. D., Pickering, C. R., Myers, J. N., Ferris, R. L., and Rocco, J. W. (2013). High intratumor genetic heterogeneity is related to worse outcome in patients with head and neck squamous cell carcinoma. Cancer *119*, 3034-3042.

Myklebust, J. H., Irish, J. M., Brody, J., Czerwinski, D. K., Houot, R., Kohrt, H. E., Timmerman, J., Said, J., Green, M. R., Delabie, J.*, et al.* (2013). High PD -1 expression and suppressed cytokine signaling distinguish T cells infiltrating follicular lymphoma tumors from peripheral T cells. Blood *121*, 1367-1376.

Nicholas, K. J., Greenplate, A. R., Flaherty, D. K., Matlock, B. K., Juan, J. S., Smith, R. M., Irish, J. M., and Kalams, S. A. (2015). Multiparameter analysis of stimulated human peripheral blood mononuclear cells: A comparison of mass and fluorescence cytometry. Cytometry Part A : the journal of the International Society for Analytical Cytology.

Nicholas, K. J., Greenplate, A. R., Flaherty, D. K., Matlock, B. K., Juan, J. S., Smith, R. M., Irish, J. M., and Kalams, S. A. (2016). Multi parameter analysis of stimulated human peripheral blood mononuclear cells: A comparison of mass and fluorescence cytometry. Cytometry Part A : the journal of the International Society for Analytical Cytology *89*, 271-280.

Nicoletti, I., Migliorati, G., Pagliacci, M. C., Grignani, F., and Riccardi, C. (1991). A rapid and simple method for measuring thymocyte apoptosis by propidium iodide staining and flow cytometry. Journal of Immunological Methods *139*, 271-279.

O'Brien, M. C., and Bolton, W. E. (1995). Compa rison of cell viability probes compatible with fixation and permeabilization for combined surface and intracellular staining in flow cytometry. Cytometry *19*, 243-255.

Ohtani, S., Kagawa, S., Tango, Y., Umeoka, T., Tokunaga, N., Tsunemitsu, Y., Roth, J. A., Taya, Y., Tanaka, N., and Fujiwara, T. (2004). Quantitative analysis of p53 -targeted gene expression and visualization of p53 transcriptional activity following intratumoral administration of adenoviral p53 in vivo. Mol Cancer Ther *3*, 93-100.

Oldford, S. A., Robb, J. D., Codner, D., Gadag, V., Watson, P. H., and Drover, S. (2006). Tumor cell expression of HLA-DM associates with a Th1 profile and predicts improved survival in breast carcinoma patients. International immunology *18*, 1591-1602.

Ordonez, N. G. (2014). Value of melanocytic -associated immunohistochemical markers in the diagnosis of malignant melanoma: a review and update. Human pathology *45*, 191-205.

Ornatsky, O. I., Lou, X., Nitz, M., Schafer, S., Sheldrick, W. S., Baranov, V. I., Bandura, D. R., and Tanner, S. D. (2008). Study of cell antigens and intracellular DNA by identification of element-containing labels and metallointercalators using inductively coupled plasma mass spectrometry. Analytical chemistry *80*, 2539-2547.

Oser, M. G., Niederst, M. J., Sequist, L. V., and Engelman, J. A. (2015). Transformation from non-small-cell lung cancer to small-cell lung cancer: molecular drivers and cells of origin. The Lancet Oncology *16*, e165-172.

Panoskaltsis, N., Reid, C. D., and Knight, S. C. (2003). Q uantification and cytokine production of circulating lymphoid and myeloid cells in acute myelogenous leukaemia. Leukemia *17*, 716-730.

Pansky, A., Hildebrand, P., Fasler-Kan, E., Baselgia, L., Ketterer, S., Beglinger, C., and Heim, M. H. (2000). Defective J ak-STAT signal transduction pathway in melanoma cells resistant to growth inhibition by interferon-alpha. International journal of cancer Journal international du cancer *85*, 720-725.

Paraiso, K. H., Xiang, Y., Rebecca, V. W., Abel, E. V., Chen, Y. A., Munko, A. C., Wood, E., Fedorenko, I. V., Sondak, V. K., Anderson, A. R.*, et al.* (2011). PTEN loss confers BRAF inhibitor resistance to melanoma cells through the suppression of BIM expression. Cancer research *71*, 2750-2760.

Park, D., Xiang, A. P., Mao, F. F., Zhang, L., Di, C. G., Liu, X. M., Shao, Y., Ma, B. F., Lee, J. H., Ha, K. S.*, et al.* (2010). Nestin is required for the proper self -renewal of neural stem cells. Stem cells (Dayton, Ohio) *28*, 2162-2171.

Patel, A. P., Tirosh, I., Trombetta, J. J., Shalek, A. K., Gillespie, S. M., Wakimoto, H., Cahill, D. P., Nahed, B. V., Curry, W. T., Martuza, R. L.*, et al.* (2014). Single -cell RNA-seq highlights intratumoral heterogeneity in primary glioblastoma. Science *344*, 1396-1401.

Peng, W., Chen, J. Q., Liu, C., Malu, S., Creasy, C., Tetzlaff, M. T., Xu, C., McKenzie, J. A., Zhang, C., Liang, X.*, et al.* (2016). Loss of PTEN Promotes Resistance to T Cell -Mediated Immunotherapy. Cancer discovery *6*, 202-216.

Perfetto, S. P., Chattopadhyay, P. K., and Roederer, M. (2004). Seventeen-colour flow cytometry: unravelling the immune system. Nature reviews Immunology *4*, 648-655.

Polikowsky, H. G., Wogsland, C. E., Diggins, K. E., Huse, K., and Irish, J. M. (2015). Cutting Edge: Redox Signaling Hypersensitivity Distinguishes Human Germinal Center B Cells. Journal of immunology (Baltimore, Md : 1950) *195*, 1364-1367.

Powell, A. A., Talasaz, A. H., Zhang, H., Coram, M. A., Reddy, A., Deng, G., Telli, M. L., Advani, R. H., Carlson, R. W., Mollick, J. A.*, et al.* (2012). Single cell prof iling of

circulating tumor cells: transcriptional heterogeneity and diversity from breast cancer cell lines. PloS one *7*, e33788.

Prahallad, A., Sun, C., Huang, S., Di Nicolantonio, F., Salazar, R., Zecchin, D., Beijersbergen, R. L., Bardelli, A., and Bernards, R. (2012). Unresponsiveness of colon cancer to BRAF(V600E) inhibition through feedback activation of EGFR. Nature *483*, 100-103.

Pyne, S., Hu, X., Wang, K., Rossin, E., Lin, T. I., Maier, L. M., Baecher-Allan, C., McLachlan, G. J., Tamayo, P., Hafler, D. A.*, et al.* (2009). Automated high -dimensional flow cytometric data analysis. Proceedings of the National Academy of Sciences of the United States of America *106*, 8519-8524.

Qiu, P., Simonds, E. F., Bendall, S. C., Gibbs Jr, K. D., Bruggner, R. V., Linderman, M. D., Sachs, K., Nolan, G. P., and Plevritis, S. K. (2011a). Extracting a cellular hierarchy from high-dimensional cytometry data with SPADE. Nat Biotech *29*, 886-891.

Qiu, P., Simonds, E. F., Bendall, S. C., Gibbs, K. D., Jr., Bruggner, R. V., Linderman, M. D., Sachs, K., Nolan, G. P., and Plevritis, S. K. (2011b). Extracting a cellular hierarchy from high-dimensional cytometry data with SPADE. Nature biotechnology *29*, 886-891.

Quintana, E., Shackleton, M., Foster, H. R., Fullen, D. R., Sabel, M. S., Johnson, T. M., and Morrison, S. J. (2010). Phenotypic heterogeneity among tumorigenic melanoma cells from patients that is reversible and not hierarchically organized. Cancer cell *18*, 510-523.

Reuben, A., Spencer, C. N., Prieto, P. A., Gopalakrishnan, V., Reddy, S. M., Miller, J. P., Mao, X., De Macedo, M. P., Chen, J., Song, X.*, et al.* (2017). Genomic and immune heterogeneity are associated with differential responses to therapy in melanoma. NPJ genomic medicine *2*.

Reya, T., Morrison, S. J., Clarke, M. F., and Weissman, I. L. (2001). Stem cells, cancer, and cancer stem cells. Nature *414*, 105-111.

Reynolds, B. A., Tetzlaff, W., and Weiss, S. (1992). A multipotent EGF -responsive striatal embryonic progenitor cell produces neurons and astrocytes. J Neurosci *12*, 4565-4574.

Ribas, A., Hodi, F. S., Lawrence, D. P., Atkinson, V., Starodub, A., Carlino, M. S., Fisher, R. A., Long, G. V., Miller, W. H., Huang, Y.*, et al.* (2016). Pembrolizumab (pembro) in combination with dabrafenib (D) and trametinib (T) for BRAF -mutant advanced melanoma: Phase 1 KEYNOTE-022 study. Journal of Clinical Oncology *34*, 3014-3014.

Richards, J. O., Treisman, J., Garlie, N., Hanson, J. P., and Oaks, M. K. (2012). Flow cytometry assessment of residual melanoma cells in tumor-infiltrating lymphocyte cultures. Cytometry Part A : the journal of the International Society for Analytical Cytology *81*, 374-381.

Rickert, R. C. (2013). New insights into pre -BCR and BCR signalling with relevance to B cell malignancies. Nature reviews Immunology *13*, 578-591.

Rizos, H., Menzies, A. M., Pupo, G. M., Carlino, M. S., Fung, C., Hyman, J., Haydu, L. E., Mijatov, B., Becker, T. M., Boyd, S. C.*, et al.* (2014). BRAF inhibitor resistance mechanisms in metastatic melanoma: spectrum and clinical impact. Clinical cancer research : an official journal of the American Association for Cancer Research *20*, 1965-1977.

Robbins, P. F., Morgan, R. A., Feldman, S. A., Yang, J. C., Sherry, R. M., Dudley, M. E., Wunderlich, J. R., Nahvi, A. V., Helman, L. J., Mackall, C. L.*, et al.* (2011). Tumor regression in patients with metastatic synovial cell sarcoma and melanoma using

genetically engineered lymphocytes reactive with NY-ESO-1. Journal of clinical oncology : official journal of the American Society of Clinical Oncology *29*, 917-924.

Robert, C., Karaszewska, B., Schachter, J., Rutkowski, P., Mackiewicz, A., Stroiakovski, D., Lichinitser, M., Dummer, R., Grange, F., Mortier, L.*, et al.* (2015a). Improved overall survival in melanoma with combined dabrafenib and trametinib. The New England journal of medicine *372*, 30-39.

Robert, C., Ribas, A., Hamid, O., Daud, A., Wolchok, J. D., Joshua, A. M., Hwu, W. J., Weber, J. S., Gangadhar, T. C., Joseph, R. W.*, et al.* (2017). Durable Complete Response After Discontinuation of Pembrolizumab in Patients With Metastatic Melanoma. Journal of clinical oncology : official journal of the American Society of Clinical Oncology, Jco2017756270.

Robert, C., Schachter, J., Long, G. V., Arance, A., Grob, J. J., Mortier, L., Daud, A., Carlino, M. S., McNeil, C., Lotem, M.*, et al.* (2015b). Pembrolizumab versus Ipilimumab in Advanced Melanoma. The New England journal of medicine *372*, 2521-2532.

Robillard, N., Pellat-Deceunynck, C., and Bataille, R. (2005). Phenotypic characterization of the human myeloma cell growth fraction. Blood *105*, 4845-4848.

Sachen, K. L., Strohman, M. J., Singletary, J., Alizadeh, A. A., Kattah, N. H., Lossos, C., Mellins, E. D., Levy, S., and Levy, R. (2012). Self -antigen recognition by follicular lymphoma B-cell receptors. Blood *120*, 4182-4190.

Sandru, A., Voinea, S., Panaitescu, E., and Blidaru, A. (2014). Survival rates of patients with metastatic malignant melanoma. Journal of medicine and life *7*, 572-576.

Schmid, I., Krall, W. J., Uittenbogaart, C. H., Braun, J., and Giorgi, J. V. (1992). Dead cell discrimination with 7-amino-actinomycin D in combination with dual color immunofluorescence in single laser flow cytometry. Cytometry *13*, 204-208.

Scholzen, T., and Gerdes, J. (2000). The Ki -67 protein: from the known and the unknown. Journal of cellular physiology *182*, 311-322.

Seghers, A. C., Wilgenhof, S., Lebbe, C., and Neyns, B. (2012). Successful rechallenge in two patients with BRAF-V600-mutant melanoma who experienced previous progression during treatment with a selective BRAF inhibitor. Melanoma research *22*, 466-472.

Shaffer, S. M., Dunagin, M. C., Torborg, S. R., Torre, E. A., Emert, B., Krepler, C., Beqiri, M., Sproesser, K., Brafford, P. A., Xiao, M.*, et al.* (2017). Rare cell variability and drug -induced reprogramming as a mode of cancer drug resistance. Nature *546*, 431-435.

Sharma, S. V., Lee, D. Y., Li, B., Quinlan, M. P., Takahashi, F., Maheswaran, S., McDermott, U., Azizian, N., Zou, L., Fischbach, M. A.*, et al.* (2010). A chromatin -mediated reversible drug-tolerant state in cancer cell subpopulations. Cell *141*, 69-80.

Shaw, H. M., McCarthy, W. H., McCarthy, S. W., and Milton, G. W. (1987). Thin malignant melanomas and recurrence potential. Archives of surgery (Chicago, Ill : 1960) *122*, 1147-1150.

Shi, H., Hugo, W., Kong, X., Hong, A., Koya, R. C., Moriceau, G., Chodon, T., Guo, R., Johnson, D. B., Dahlman, K. B.*, et al.* (2014). Acquired resistance and clonal evolution in melanoma during BRAF inhibitor therapy. Cancer discovery *4*, 80-93.

Shin, D. S., Zaretsky, J. M., Escuin-Ordinas, H., Garcia-Diaz, A., Hu-Lieskovan, S., Kalbasi, A., Grasso, C. S., Hugo, W., Sandoval, S., Torrejon, D. Y.*, et al.* (2017). Primary Resistance to PD-1 Blockade Mediated by JAK1/2 Mutations. Cancer discovery *7*, 188-201.

Shtivelman, E., Davies, M. Q., Hwu, P., Yang, J., Lotem, M., Oren, M., Flaherty, K. T., and Fisher, D. E. (2014). Pathways and therapeutic targets in melanoma. Oncotarget *5*, 1701-1752.

Simoes-Costa, M., and Bronner, M. E. (2015). Establishing neural crest identity: a gene regulatory recipe. Development (Cambridge, England) *142*, 242-257.

Situm, M., Buljan, M., Bulic, S. O., and Simic, D. (2007). The mechanisms of UV radiation in the development of malignant melanoma. Collegium antropologicum *31 Suppl 1*, 13-16.

Smalley, K. S., Lioni, M., Dalla Palma, M., Xiao, M., Desai, B., Egyhazi, S., Hansson, J., Wu, H., King, A. J., Van Belle, P.*, et al.* (2008). Increased cyclin D1 expression can mediate BRAF inhibitor resistance in BRAF V600E-mutated melanomas. Molecular cancer therapeutics *7*, 2876-2883.

Song, C., Piva, M., Sun, L., Hong, A., Moriceau, G., Kong, X., Zhang, H., Lomeli, S., Qian, J., Yu, C. C.*, et al.* (2017). Recurrent Tumor Cell -Intrinsic and -Extrinsic Alterations during MAPKi-Induced Melanoma Regression and Early Adaptation. Cancer discovery *7*, 1248-1265.

Sosman, J. A., Kim, K. B., Schuchter, L., Gonzalez, R., Pavlick, A. C., Weber, J. S., McArthur, G. A., Hutson, T. E., Moschos, S. J., Flaherty, K. T.*, et al.* (2012). Survival in BRAF V600-mutant advanced melanoma treated with vemurafenib. The New England journal of medicine *366*, 707-714.

Spitzer, Matthew H., and Nolan, Garry P. Mass Cytometry: Single Cells, Many Features. Cell *165*, 780-791.

Spitzer, M. H., and Nolan, G. P. (2016). Mass Cytometry: Single Cells, Many Features. Cell *165*, 780-791.

Spranger, S., Spaapen, R. M., Zha, Y., Williams, J., Meng, Y., Ha, T. T., and Gajewski, T. F. (2013). Up -regulation of PD-L1, IDO, and T(regs) in the melanoma tumor

microenvironment is driven by CD8(+) T cells. Science translational medicine *5*, 200ra116.

Sumimoto, H., Takano, A., Teramoto, K., and Daigo, Y. (2016). RAS -Mitogen-Activated Protein Kinase Signal Is Required for Enhanced PD-L1 Expression in Human Lung Cancers. PloS one *11*, e0166626.

Sun, C., Wang, L., Huang, S., Heynen, G. J., Prahallad, A., Robert, C., Haanen, J., Blank, C., Wesseling, J., Willems, S. M.*, et al.* (2014). Reversible and adaptive resistance to BRAF(V600E) inhibition in melanoma. Nature *508*, 118-122.

Swingle, M., Ni, L., and Honkanen, R. E. (2007). Small -molecule inhibitors of ser/thr protein phosphatases: specificity, use and common forms of abuse. Methods in molecular biology *365*, 23-38.

Timmerman, J. M., Czerwinski, D. K., Davis, T. A., Hsu, F. J., Benike, C., Hao, Z. M., Taidi, B., Rajapaksa, R., Caspar, C. B., Okada, C. Y.*, et al.* (2002). Idiotype -pulsed dendritic cell vaccination for B-cell lymphoma: clinical and immune responses in 35 patients. Blood *99*, 1517-1526.

Tirosh, I., Izar, B., Prakadan, S. M., Wadsworth, M. H., 2nd, Treacy, D., Trombetta, J. J., Rotem, A., Rodman, C., Lian, C., Murphy, G.*, et al.* (2016). Dissecting the multicellular ecosystem of metastatic melanoma by single-cell RNA-seq. Science (New York, NY) *352*, 189-196.

Trentin, L., Cabrelle, A., Facco, M., Carollo, D., Miorin, M., Tosoni, A., Pizzo, P., Binotto, G., Nicolardi, L., Zambello, R.*, et al.* (2004). Homeostatic chemokines drive migration of malignant B cells in patients with non-Hodgkin lymphomas. Blood *104*, 502-508.

Tricot, S., Meyrand, M., Sammicheli, C., Elhmouzi-Younes, J., Corneau, A., Bertholet, S., Malissen, M., Le Grand, R., Nuti, S., Luche, H., and Cosma, A. (2015). Evaluating the

efficiency of isotope transmission for improved panel design and a comparison of the detection sensitivities of mass cytometer instruments. Cytometry Part A : the journal of the International Society for Analytical Cytology *87*, 357-368.

Van Allen, E. M., Wagle, N., Sucker, A., Treacy, D. J., Johannessen, C. M., Goetz, E. M., Place, C. S., Taylor-Weiner, A., Whittaker, S., Kryukov, G. V.*, et al.* (2014). The genet ic landscape of clinical resistance to RAF inhibition in metastatic melanoma. Cancer discovery *4*, 94-109.

van der Bruggen, P., Traversari, C., Chomez, P., Lurquin, C., De Plaen, E., Van den Eynde, B., Knuth, A., and Boon, T. (1991). A gene encoding an anti gen recognized by cytolytic T lymphocytes on a human melanoma. Science (New York, NY) *254*, 1643-1647.

van Dongen, J. J., Lhermitte, L., Bottcher, S., Almeida, J., van der Velden, V. H., Flores-Montero, J., Rawstron, A., Asnafi, V., Lecrevisse, Q., Lucio, P.*, et al.* (2012). EuroFlow antibody panels for standardized n-dimensional flow cytometric immunophenotyping of normal, reactive and malignant leukocytes. Leukemia *26*, 1908-1975.

Van Gassen, S., Callebaut, B., Van Helden, M. J., Lambrecht, B. N., Demeester, P., Dhaene, T., and Saeys, Y. (2015a). FlowSOM: Using self -organizing maps for visualization and interpretation of cytometry data. Cytometry Part A : the journal of the International Society for Analytical Cytology.

Van Gassen, S., Callebaut, B., Van Helden, M. J., Lambrecht, B. N., Demeester, P., Dhaene, T., and Saeys, Y. (2015b). FlowSOM: Using self -organizing maps for visualization and interpretation of cytometry data. Cytometry Part A : the journal of the International Society for Analytical Cytology *87*, 636-645.

Van Meter, M. E. M., Diaz-Flores, E., Archard, J. A., Passegue, E., Irish, J. M., Kotecha, N., Nolan, G. P., Shannon, K., and Braun, B. S. (2007). K -Ras(G12D) expression induces hyperproliferation and aberrant signaling in primary hematopoietic stem/progenitor cells. Blood *109*, 3945-3952.

Verfaillie, A., Imrichova, H., Atak, Z. K., Dewaele, M., Rambow, F., Hulselmans, G., Christiaens, V., Svetlichnyy, D., Luciani, F., Van den Mooter, L.*, et al.* (2015). Decoding the regulatory landscape of melanoma reveals TEADS as regulators of the invasive cell state. Nature communications *6*, 6683.

Volkovova, K., Bilanicova, D., Bartonova, A., Letasiova, S., and Dusinska, M. (2012). Associations between environmental factors and incidence of cutaneous melanoma. Review. Environmental health : a global access science source *11 Suppl 1*, S12.

von Boehmer, L., Mattle, M., Bode, P., Landshammer, A., Schafer, C., Nuber, N., Ritter, G., Old, L., Moch, H., Schafer, N.*, et al.* (2013). NY -ESO-1-specific immunological pressure and escape in a patient with metastatic melanoma. Cancer immunity *13*, 12.

Wan, P. T., Garnett, M. J., Roe, S. M., Lee, S., Niculescu-Duvaz, D., Good, V. M., Jones, C. M., Marshall, C. J., Springer, C. J., Barford, D., and Marais, R. (2004). Mechanism of activation of the RAF-ERK signaling pathway by oncogenic mutations of B-RAF. Cell *116*, 855-867.

Wang, M. L., Rule, S., Martin, P., Goy, A., Auer, R., Kahl, B. S., Jurczak, W., Advani, R. H., Romaguera, J. E., Williams, M. E.*, et al.* (2013). Targeting BTK with ibrutinib in relapsed or refractory mantle-cell lymphoma. The New England journal of medicine *369*, 507-516.

Wang, Y. J., Golson, M. L., Schug, J., Traum, D., Liu, C., Vivek, K., Dorrell, C., Naji, A., Powers, A. C., Chang, K. M.*, et al.* (2016). Single -Cell Mass Cytometry Analysis of the Human Endocrine Pancreas. Cell metabolism *24*, 616-626.

Warabi, M., Kitagawa, M., and Hirokawa, K. (2000). Loss of MHC class II expression is associated with a decrease of tumor-infiltrating T cells and an increase of metastatic potential of colorectal cancer: immunohistological and histopathological analyses as compared with normal colonic mucosa and adenomas. Pathology, research and practice *196*, 807-815.

Weber, L. M., and Robinson, M. D. (2016). Comparison of clusterin g methods for high-dimensional single-cell flow and mass cytometry data. Cytometry Part A : the journal of the International Society for Analytical Cytology *89*, 1084-1096.

Wilmott, J. S., Tembe, V., Howle, J. R., Sharma, R., Thompson, J. F., Rizos, H., Lo, R. S., Kefford, R. F., Scolyer, R. A., and Long, G. V. (2012). Intratumoral molecular heterogeneity in a BRAF-mutant, BRAF inhibitor-resistant melanoma: a case illustrating the challenges for personalized medicine. Molecular cancer therapeutics *11*, 2704-2708.

Wogsland, C. E., Greenplate, A. R., Kolstad, A., Myklebust, J. H., Irish, J. M., and Huse, K. (2017). Mass Cytometry of Follicular Lymphoma Tumors Reveals Intrinsic Heterogeneity in Proteins Including HLA-DR and a Deficit in Nonmalignant Plasmablast and Germinal Center B-Cell Populations. Cytometry Part B, Clinical cytometry *92*, 79-87.

Wozniak, J., and Kopec-Szlezak, J. (2004). c -Kit receptor (CD117) expression on myeloblasts and white blood cell counts in acute myeloid leukemia. Cytometry B Clin Cytom *58*, 9-16.

Wu, A. R., Neff, N. F., Kalisky, T., Dalerba, P., Treutlein, B., Rothenberg, M. E., Mburu, F. M., Mantalas, G. L., Sim, S., Clarke, M. F., and Quake, S. R. (2014). Quantitative assessment of single-cell RNA-sequencing methods. Nature methods *11*, 41-46.

Wu, X., Peng, M., Huang, B., Zhang, H., Wang, H., Huang, B., Xue, Z., Zhang, L., Da, Y., Yang, D*., et al.* (2013). Immune microenvironment profiles of tumor immune equilibrium and immune escape states of mouse sarcoma. Cancer letters *340*, 124-133.

Yoon, H. H., Shi, Q., Sukov, W. R., Lewis, M. A., Sattler, C. A., Wiktor, A. E., Wu, T. T., Diasio, R. B., Jenkins, R. B., and Sinicrope, F. A. (2012). Adverse prognostic impact of intratumor heterogeneous HER2 gene amplification in patients with esophageal adenocarcinoma. Journal of clinical oncology : official journal of the American Society of Clinical Oncology *30*, 3932-3938.

Zaretsky, J. M., Garcia-Diaz, A., Shin, D. S., Escuin-Ordinas, H., Hugo, W., Hu-Lieskovan, S., Torrejon, D. Y., Abril-Rodriguez, G., Sandoval, S., Barthly, L*., et al.* (2016). Mutations Associated with Acquired Resistance to PD-1 Blockade in Melanoma. The New England journal of medicine *375*, 819-829.

Zhang, B., Wang, J., Wang, X., Zhu, J., Liu, Q., Shi, Z., Chambers, M. C., Zimmerman, L. J., Shaddox, K. F., Kim, S*., et al.* (2014a). Proteogenomic characterization of human colon and rectal cancer. Nature *513*, 382-387.

Zhang, B., Wang, J., Wang, X., Zhu, J., Liu, Q., Shi, Z., Chambers, M. C., Zimmerman, L. J., Shaddox, K. F., Kim, S*., et al.* (2014b). Proteogenomic characterization of human colon and rectal cancer. Nature *513*, 382-387.

Zheng, A., Castren, K., Saily, M., Savolainen, E. R., Koistinen, P., and Vahakangas, K. (1999). p53 status of newly established acute myeloid leukaemia cell lines. Br J Cancer *79*, 407-415.

Zimmerlin, L., Donnenberg, V. S., and Donnenberg, A. D. (2011). Rare event detection and analysis in flow cytometry: bone marrow mesenchymal stem cells, breast cancer

stem/progenitor cells in malignant effusions, and pericytes in disaggregated adipose tissue. Methods Mol Biol *699*, 251-273.